REPORT DOCUMENTATION PAGE

Form Approved
OMB No. 0704-0188

The public reporting burden for this collection of information is estimated to average 1 hour per response, including the time for reviewing instructions, searching existing data sources, gathering and maintaining the data needed, and completing and reviewing the collection of information. Send comments regarding this burden estimate or any other aspect of this collection of information, including suggestions for reducing the burden, to Department of Defense, Washington Headquarters Services, Directorate for Information Operations and Reports (0704-0188), 1215 Jefferson Davis Highway, Suite 1204, Arlington, VA 22202-4302. Respondents should be aware that notwithstanding any other provision of law, no person shall be subject to any penalty for failing to comply with a collection of information if it does not display a currently valid OMB control number.
PLEASE DO NOT RETURN YOUR FORM TO THE ABOVE ADDRESS.

1. REPORT DATE *(DD-MM-YYYY)*	2. REPORT TYPE	3. DATES COVERED *(From - To)*
04/11/2016	final	Jan 2013 - Dec 2015

4. TITLE AND SUBTITLE
Investigation of Microcavitation-induced Effects using in Vitro Models for Traumatic Brain Injury

5a. CONTRACT NUMBER

5b. GRANT NUMBER
N00014-13-1-0404

5c. PROGRAM ELEMENT NUMBER

5d. PROJECT NUMBER

5e. TASK NUMBER

5f. WORK UNIT NUMBER

6. AUTHOR(S)
Cho, Michael

7. PERFORMING ORGANIZATION NAME(S) AND ADDRESS(ES)
University of Illinois at Chicago
809 S. Marshfield Ave.
Chicago, IL 60612-7205

8. PERFORMING ORGANIZATION REPORT NUMBER

9. SPONSORING/MONITORING AGENCY NAME(S) AND ADDRESS(ES)
Office of Naval Research
875 North Randolph St.
Arlington, VA 22203-1995

10. SPONSOR/MONITOR'S ACRONYM(S)

11. SPONSOR/MONITOR'S REPORT NUMBER(S)

12. DISTRIBUTION/AVAILABILITY STATEMENT

13. SUPPLEMENTARY NOTES

14. ABSTRACT

The project was focused on the development of in vitro biomimetic systems to examine the impact of microcavitation in the brain tissue. We have successfully designed and validated several biosystems to elucidate quantitatively potential biophysical and molecular mechanisms mediating bioeffects which arise from blast-induced shock waves and subsequently generated microbubbles (i.e., microcavitation). The coupling mechanisms responsible for the bioeffects of microbubbles in brain tissues can now be better understood with detail, and lead to formulation of strategies to reverse some of the observed adverse effects.

15. SUBJECT TERMS
traumatic brain injury models, shockwave, microcavitation, real-time measurements of bioeffects, mechanotransduction

16. SECURITY CLASSIFICATION OF:			17. LIMITATION OF ABSTRACT	18. NUMBER OF PAGES	19a. NAME OF RESPONSIBLE PERSON
a. REPORT	b. ABSTRACT	c. THIS PAGE			19b. TELEPHONE NUMBER *(Include area code)*

FINAL REPORT

PI:	Michael Cho, Ph.D.
Organization:	University of Illinois at Chicago
Award Number:	N000141310404
Project Title	Investigation of Microcavitation-induced Effects Using in Vitro Models for Traumatic Brain Injury
Period:	January 1, 2013 to December 31, 2015

We are pleased to submit the final report that outlines research progress and accomplishments by an interdisciplinary team of investigators from three universities including University of Illinois at Chicago (UIC, lead institution), Old Dominion University (ODU) and Cornell University (CU).

Scientific and Technical Objectives:

The project was focused on the development of in vitro biomimetic systems to examine the impact of microcavitation in the brain tissue. We have successfully designed and validated several biosystems to elucidate quantitatively potential biophysical and molecular mechanisms mediating bioeffects which arise from blast-induced shock waves and subsequently generated microbubbles (i.e., microcavitation). In addition, by incorporating microfabrication technology, microbubbles interacting with brain cells were controlled and confined to the specific areas of cell cultures. This led to more systematic studies in which the collimated microbubbles rising to the surface became predictable. Our results indicate that, following microbubble collapse, the brain cells are immediately detached from the substrate and the cells seeded peripherally around the site of microbubble collapse are also adversely impacted. When treated with surfactants such as poloxamers, the partially damaged cells showed evidence of recovering cell functionality. These critical findings provide a comprehensive molecular framework. The coupling mechanisms responsible for the bioeffects of microbubbles in brain tissues can now be better understood with detail, and lead to formulation of strategies to reverse some of the observed adverse effects.

Approach:

We have employed our full capability of monitoring and recording direct and indirect bioeffects in response to microbubble generation and collapsing. Unique experimental approaches have been incorporated to redesign and improve the exposure chamber. Microfabrication technology was introduced to spatially guide the rise of collimated microbubbles to the surface and therefore controlled the site of collapse of microbubbles. High resolution and time-resolved microscopy combined with computational modeling are used to validate or refute hypotheses. In so doing we have established biophysical and molecular mechanisms that mediate the bioeffects due to collapse of microbubbles and identified biomedical strategies to preserve the cellular

integrity. Insights from these studies are expected to lead to formulation of a new paradigm for altered cellular homeostasis that may be responsible for the blast-induced and subtle brain injury.

Concise Accomplishments:

Scientific and engineering accomplishments are summarized by five peer-reviewed manuscripts, two manuscripts under review, and multiple abstracts and presentations. Our work was recognized and selected for the Reviewer Choice Award twice in a row at the 2014 Biomedical Engineering Society Meeting in San Antonio, TX and at the 2015 Biomedical Engineering Society Meeting in Tampa, FL.

Expanded Accomplishments:

Because the accomplishments are many and require explanation with in-depth details, reprints of the following published/accepted manuscripts are provided with full reference.

1) Kang D, Cho M, Xiao S. Shock wave generation in water for biological studies. IEEE Trans. Plasma Sci. 2014; 42:3231-3238.
2) Sun S, Wong SW, Mak AFT, Cho M. Impact of oxidative stress on cellular biomechanics and Rho signaling in C2C12 myoblasts. J. Biomech. 2014; 47:3650-3656.
3) Sun S, Kanagaraj J, Cho L, Kang D, Xiao S, Cho M. Characterization of subcellular responses induced by exposure of microbubbles to astrocytes. J. Neurotrauma. 2015; 32;1441-1448.
4) Zhu W, Alkhazal M, Cho M, Xiao S. Microbubble generation by piezotransducer for biological studies. Rev. Sci. Instruments. 2015. (*http://dx.doi.org/10.1063/1.4936555*).
5) Shareef F. Sun S, Kotecha M, Kassem I, Azar D, Cho M. Engineering a light attenuating artificial iris. Invest. Ophthalmol. Vis. Sci. *In Press.*

Manuscripts Submitted and Currently under Review:

Kanagaraj J, Chen B, Xiao S, Cho M. Reparative effects of Poloxamer P188 in astrocytes exposed to controlled microcavitation. **PLoS One.**

Wong SW, Yao Y, Hong Y, Ma Z, Sun S, Cho M, Lee KKH, Mak AFT. Effects of Poloxamer 188 on muscle cell damage mechanics under oxidative stress. **Ann. Biomed. Eng.**

Abstracts Published and Presentations:

Sun S, Kanagaraj J, Cho L, Kang D, Xiao S, Cho M. Engineering in vitro models to elucidate the effect of microcavitation in astrocytes. The 2014 Annual Fall Meeting of the Biomedical Engineering Society. San Antonio, TX. (selected for the Reviewer Choice Award)

Sun S, Kanagaraj J, Cho L, Kang D, Xiao S, Cho M. Altered biophysical properties of astrocytes in response to microbubbles. The 36th Annual International Conference of the IEEE Engineering in Medicine and Biology Society. Chicago, IL. 2014.

Shareef F, Szlachta D, Contreras G, Chen A, Azar D, Cho M. Designing a photo-responsive contact lens. The 2015 Annual Meeting of the Association for Research in Vision and Ophthalmology. Denver, CO.

Alkazal M, Zhou C, Zhu W, Cho M, Xiao S. Generating focused pressure wave with ultrasound piezotransducers. IEEE Pulsed Power Conference. Austin, TX. 2015.

Kanagaraj J, Chen B, Paul A, Xiao S, Cho M. Preventive effects of Poloxamer P188 in astrocytes exposed to controlled microcavitation. The 2015 Annual Fall Meeting of the Biomedical Engineering Society. Tampa, FL. (selected for the Reviewer Choice Award)

Chen B, Sun S, Kanagaraj J, Cho M. Systematic design for prediction of shielding distance of astrocytes impacted from localized collapse of microbubbles. The 2015 Annual Fall Meeting of the Biomedical Engineering Society. Tampa, FL.

Poellmann MJ, Gothard NA, Oliveira J, Sun S, Cho M, Lee RC. Poloxamer P188 reduces membrane defect size and restores membrane tension to saponin-injured cells in vitro. The 2015 Annual Fall Meeting of the Biomedical Engineering Society. Tampa, FL.

Technology Transfer:
Not applicable.

Awards Participants:
Dr. Michael Cho (PI, Professor, University of Illinois at Chicago and now at University of Texas at Arlington, US citizen)
Dr. Bo Chen (Research Assistant Professor, University of Illinois at Chicago, US permanent resident)
Dr. Shan Sun (Research Assistant Professor, University of Illinois at Chicago)
Mr. Johnwesly Kanagaraj (Graduate Student, University of Illinois at Chicago, US citizen)
Dr. Shu Xiao (co-PI, Assistant Professor, Old Dominion University, US permanent resident)
Mr. Chunrong Zhou (Technician, Old Dominion University, US permanent resident)
Mr. Mohammed Alkhazal (Graduate Student, Old Dominion University, Saudi Arabia National)
Dr. Jeff Varner (co-PI, Associate Professor, Cornell University, US citizen)
Mr. Ankit Chandra (Graduate Student, Cornell University, Indian national)

Shock Wave Generation in Water for Biological Studies

Dongkoo Kang, Jong Bong Nah, Michael Cho, and Shu Xiao, *Senior Member, IEEE*

***Abstract*—We have used a pulsed power generator based on stacking MOSFET switches to create breakdown in water and generate shock waves. The pulses with an exponential decay have a maximum voltage of 4 kV. With the pulse application of approximately 50 μs, the breakdown voltage is approximately 3 kV. Postbreakdown events, such as shock wave emission and bubble expansion and collapse were recorded by a fast camera. The shock speed was recorded as 1.5 km/s and the maximum bubble diameter is 2.3 mm. This shock wave generator can be used on the microscope and provides a means of studying the shock impact on biological cells.**

***Index Terms*—Biological studies, shock wave, stacking MOSFETs, water breakdown.**

I. Introduction

SHOCK waves have been used in dismantling kidney stones (lithotripsy) [1], tumor destruction [2], and drug or gene delivery [3], [4]. The high gradient of the pressure carried by shock waves causes complicate reflections and refractions when they impinge sonic impedance discontinuities. A rarefaction wave follows the compression wave and carries a negative pressure, causing the coexistence of compression and expansion. It is such compressive and tensile forces that cause most of the damages. In the liquid environment, such transition of positive to negative pressure could induce microbubbles and microstream force, which are responsible for the pore formation of cells (sonoporation) [5].

Generating a high gradient pressure front can be done by shock tubes or gas guns. They are also used in generating a long lasting blasting wave up to milliseconds or seconds. In the liquid environment, for example, under water, a piezoelectric transducer, or an arc discharge can be used for repeatable use in a controllable condition [6]. For the purpose of studying the impact of pressure waves to biological cells, we have used the arc discharge considering the fact that it is possible to construct a low-profile shock wave system on the microscope stage. This would be of an interest in studying the response of biological cells to shock waves, in particular, cells cultured on a coverslip. Immediate effects can be studied by performing real-time measurement on the microscope and therefore such system will be useful in understanding the interaction of shock waves with biological cells.

Shock waves generated by electric discharges in the liquid were studied as a byproduct of high power switching using liquid as medium [7]–[9]. Numerous data have been generated and useful conclusions have been drawn. Most of the data were focused on high voltages (above 10 kV) and high peak currents (up to kiloampere) [10]–[12]. We instead use lower voltages (4 kV) and low currents (<50 A) to produce shock waves in a culture dish. The pulsed power source was based on a capacitor discharge switched by four MOSFET switches stacking in series. Our aim was to establish a consistent, reliable shock wave source. Specifically, we have studied the temporal evolution of shock waves and bubble expansion through a high speed camera. The pressure change over distance, the bubble radius over distance, and their relation at the onset of the shock wave are examined. We estimate the shock pressure from the speed of the shock wave and bubble expansion.

II. Theoretical Considerations

Using pulsed power systems to generate shock waves in water relies on electric breakdown. One may also produce pressure waves when streamers are initiated [13]. Higher pressure is, however, produced when electric breakdown occurs and the electric field can be as high as 1 MV/cm [14], [15]. Rapid heating occurs when the current increases and the voltage across the electrode gap collapses. Significant amount of electric energy deposits in the plasma channel in the form of heating and vaporizing the liquid by increasing the internal and kinetic energies. The rapid expansion of the plasma channel passes momentum to the surrounding water, compressing the water, and forming shock waves. During earlier time of the expansion of the plasma channel, the pressure behind the shock wave front is smaller than the pressure at the boundary of the plasma channel. As the shock waves detach from the plasma channel, they propagate at a supersonic speed very near the electrodes but become sonic as the distance increases. Even at the sound speed, the wave could still carry a pressure greater than the ambient pressure. While the shock wave emission occurs much faster, the plasma channel or bubble left behind still has significant pressure and keeps growing in volume until it reaches its peak size before

Manuscript received December 2, 2013; revised June 11, 2014; accepted July 3, 2014. Date of publication August 5, 2014; date of current version October 21, 2014. This work was supported by the Office of Naval Research.

D. Kang and J. B. Nah are with the Frank Reidy Research Center for Bioelectrics, Old Dominion University, Norfolk, VA 23529-0246 USA (e-mail: kang.whistle@gmail.com; jnahx001@odu.edu).

M. Cho is with the Department of Bioengineering, University of Illinois, Chicago, IL 60607 USA (e-mail: mcho@uic.edu).

S. Xiao is with the Frank Reidy Research Center for Bioelectrics, Old Dominion University, Norfolk, VA 23529-0246 USA, and also with the Department of Electrical and Computer Engineering, Old Dominion University, Norfolk, VA 23529-0246 USA (e-mail: sxiao@odu.edu).

Color versions of one or more of the figures in this paper are available online at http://ieeexplore.ieee.org.

Digital Object Identifier 10.1109/TPS.2014.2339171

0093-3813 © 2014 IEEE. Personal use is permitted, but republication/redistribution requires IEEE permission.
See http://www.ieee.org/publications_standards/publications/rights/index.html for more information.

collapsing. A second shock wave may be observed after the collapse of the gas bubble [10]–[16].

A. Bubble Dynamics and Pressure

In the stage of bubble expansion, the volume grows from streamer channels, which is created in the prebreakdown phase. The energy balance equation is [17]

$$\frac{\beta}{\beta-1}P_c\dot{V}_c + \frac{1}{\beta-1}V_c\dot{P}_c = I^2R_c \tag{1}$$

where P_c is the pressure of the plasma channel, β is the effective adiabatic exponent, and R_c is the measurable resistance of the plasma channel and depends on time. A more complicated form of the plasma channel resistance including nonuniform density and temperature distribution can be found in [18]. Here, we will not consider such case. Rather, we obtain its expression from measurement. V_c is the volume of the spherical plasma $V_c = 4\pi r_c^3/3$. The largest heating occurs in the resistive phase of the plasma channel.

The current allows the connection of the plasma channel resistance with the external circuit that provides the energy

$$L\dot{I} + RI + \frac{1}{C}\int_0^t I\, d\tau = U_0 \tag{2}$$

where R is the total resistance of the circuit, $R = R_R + R_c$. R_R is the resistance placed in series with the gap and in our case is 100 Ω. The plasma channel is called bubble in its later phase. The bubble motion started from rest is irrotational and the equation of continuity gives

$$\nabla \cdot \bar{u} = 0 \tag{3}$$

where $\bar{u}$ is the velocity vector of the bubble. Once a velocity potential, ϕ, is introduced: $\bar{u} = \nabla\phi$, the continuity equation becomes Laplace's equation

$$\nabla^2\phi = 0. \tag{4}$$

In general, with Green's functions, we can solve this velocity potential at any point ($\check{r}$) inside the bubble using Green's theorem, which allows the differential equation to be converted to an integral equation

$$\phi(\check{r}) = (1/4\pi)\int_\Omega (G\partial\phi/\partial n - \phi\partial G/\partial n)dS. \tag{5}$$

The integral is performed over the boundary Ω, provided the boundary conditions are known. They typically include rigid boundaries (no flow condition: $\nabla\phi\cdot\check{n} = 0$, $\check{n}$ is the boundary normal) and a free boundary on the bubble surface. Using the momentum equation, the free boundary condition can be written

$$\partial\phi/\partial t + 1/2|\nabla\phi|^2 + (p_g + p_c)/\rho + gz = p_\infty/\rho. \tag{6}$$

Equation (6) is also called Bernoulli equation, which allows ϕ to be determined at later time $t + \delta t$, so the bubble solution through time can be obtained through iteration [19].

In this paper, we will not use this approach to solve the bubble dynamics, but the outlined process above points to an important conclusion relevant to our study. That is, in our experiment, we created discharges on the surface of a glass coverslip. The bubble dynamics share the same characteristics as that for the discharges in free field. This is so because their Green's functions are the same.

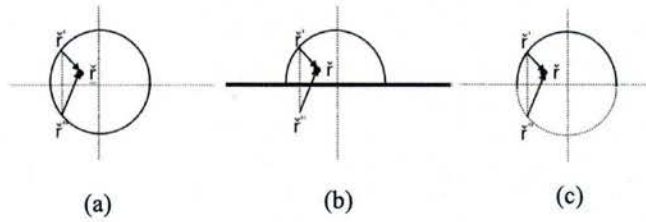

Fig. 1. Illustration of Green's functions for a free field source and a source on top of a rigid boundary. (a) In a spherical expansion, the sources on the bubble surface form a symmetry from the upper half-plane to the lower half-plane. (b) Bubble expansion on the surface of a boundary. (c) Effect of boundary can be considered by adding symmetrical images in the lower half-plane, which resembles (a).

For the bubble in the free field, the Green's function for the source on the bubble surface is

$$G = 1/|\check{r} - \check{r}'| + 1/|\check{r} - \check{r}''| \tag{7}$$

where $\check{r}'$ locates in the upper half-plane and $\check{r}''$ in the lower half-plane. For the bubble generated on the coverslip surface, the coverslip can be considered by the method of images [16]. The sources like $\check{r}'$, and their images, like $\check{r}''$ with an equal strength create the same boundary condition as the rigid boundary (Fig. 1). The corresponding Green's function is identical to (7). Therefore, we can drop the integral over the rigid boundary, but integrate over a full sphere surface in the free field. Therefore, the solutions for both cases should be the same based on (5) and (7). Such conclusion is also drawn in [20]. A more concise expression for a bubble growing in the free field (also applied in our case) is developed according to the square root of time [21]

$$r_c(t) = at^{\frac{1}{2}}. \tag{8}$$

In this simplified bubble expansion relation, we can estimate the coefficient a from the images of bubble expansion. We note that in (8), as $t = 0$, the radius of the bubble becomes zero, which implies that the transition of streamer to arc is instantaneous. One can also solve a more complicated form of bubble radius [11], [22], which is a function of the enthalpy difference between the liquid at the bubble wall and at hydrostatic pressure.

Assuming the decrease in resistance of the arc is due to the increase of conductivity and the expansion of the volume of the arc, (8) leads to the resistance of the plasma channel [23]

$$R_c(t) \sim b/t^{\frac{1}{2}}. \tag{9}$$

The constant b can be estimated from the resistance of the water arc by measuring the voltage and current across the electrodes. Equations (1), (2), (8), and (9) determine the pressure development as the energy from the circuit deposits in the form of Joule heating.

The initial conditions for the unknowns are given: $I = 0$, $dI/dt = U_0/L$, $P_c = 100$ kPa, and $V_c = 0$.

In solving the equations, the parameters need to be normalized

$$\bar{I} = \frac{I}{U_0}\sqrt{\frac{L}{C}}, \bar{t} = \frac{t}{\sqrt{LC}}, \bar{R} = R\sqrt{C/L}, \bar{P} = P/\rho_0 c_0^2$$

where ρ_0 is the unperturbed water density and c_0 is the sonic velocity in water.

B. Shock Wave Pressure

The pressure and particle velocity at the gas-water boundary are equal at all times [16]. Knowing the pressure of the expansion bubble, its radius and speed, one can obtain the shock pressure at a distance r [11]

$$p(r) = A\left[\frac{2}{n+1} + \frac{n-1}{n+1}\left(1 + \frac{n+1}{rc_0^2}G\right)^{\frac{1}{2}}\right]^{\frac{2n}{n-1}} - B \quad (10)$$

where $G = R_b(H + U^2/2)$ is a constant along a path or a characteristic as the pressure wave travels. H is the enthalpy and can be determined from the bubble wall

$$H = \int_{p_0}^{p(R_b)} \frac{dp}{\rho} = \frac{n}{n-1}\frac{A}{\rho_0}\left[\left(\frac{p(R_b)+B}{A}\right)^{\frac{n-1}{n}} - 1\right]. \quad (11)$$

In the enthalpy expression, $A = 0.3001$ GPa, $B = 0.3$ GPa, $n = 7$, $\rho_0 = 1000$ kg/m^3, and $c_0 = 1480$ m/s.

If we consider water is incompressible, the pressure field can also be given by the following simplified expression [24]:

$$p(r) = p_0 + \frac{R_b}{r}(P_c - p_0) + \frac{R_b(r^3 - R_b^3)}{r^4}\frac{\rho_0 U^2}{2} \quad (12)$$

where P_c is the bubble pressure at its radius R_b, r is the distance from the bubble center, and U is the speed of the bubble when the bubble expands to R_b. The kinetic energy carried by the pressure wave can be calculated by integrating the pressure pulse over the duration t' at a given distance r_s

$$E_s = \frac{4\pi r_s^2}{\rho_0 c_0}\int_0^{t'} p(t)^2 dt. \quad (13)$$

C. Power Dependence

In electrical discharges, the energy delivered to the water spark is calculable from the measured voltage and current. The generation of shock wave mostly occurs in the current rise time during which the momentum of the expansion is the largest. At later time, the energy deposition in the plasma channel becomes much less, as the majority of the energy will be absorbed by the external resistance in the circuit.

Rather than solving the differential equations, the peak pressure in the plasma channel can also be estimated by [12]

$$p = 8(P'/l)^{\frac{1}{2}} \quad (14)$$

where P' is the rate of power deposition in the channel during the resistive phase of the discharge and l is the spark length. The power relation is simply given by the product of voltage and current

$$P(t) = I(t)V(t). \quad (15)$$

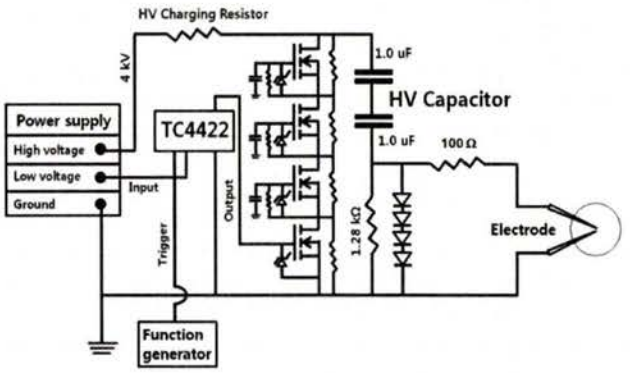

Fig. 2. Pulsed power system and experimental setup. Two high voltage capacitors (1 μF) are connected in series and switched by four MOSFET switches stacking in series. An exponential-decay pulse is applied to the electrodes, which are submerged in water. Shock wave emits as a result of the breakdown of water gap.

III. Experimental Setup

The experimental setup is shown in Fig. 2. We used two needle electrodes arranged in V-shape and the tips were separated by 0.2 mm. The electrodes were mounted on a holder. The two electrodes were touching the bottom of a culture dish, which was filled with tap water (resistivity: ~7 kΩ·cm). The pulsed power system used in the experiment has two, 1-μF capacitors charged by a dc voltage source (4 kV, Ultravolt, 4C series). The capacitors are discharged by four MOSFET switches (IXFB38N100Q2) stacking in series. The designing details of such stacking circuit can be found in [25]. In brief, the gate and source terminals of the MOSFET switches are held at the same potential before closing. As soon as the bottom switch is turned ON by a noninverted MOSFET driver (TC4422), the second switch closes as the gate is positively biased through discharging the capacitor that connects to the gate. In a similar fashion, the third and fourth switches turn ON sequentially. Because the rated current of each MOSFET is 20 A (average rating, the peak current is higher as shown later), several resistors connecting in series with the needle electrodes were used to limit the current. Four resistors with a total resistance of 100 Ω were used. The voltage across the electrodes was measured by a high voltage probe (Tektronix P6015) and the current was measured by a Pearson coil (Pearson, 5046). A separate current viewing resistor (1.1 Ω) was also used to measure the current and was connected in series with the water gap. The oscilloscope was Tektronix TDS640A.

The laser shadowgraphy was used to capture the shock waves and bubble expansions after the breakdown of water gap. A He–Ne laser was used to illuminate the electrode region and a fast camera (4Picos, Stanford) was used to record the images in a time-resolved fashion. The camera was triggered by the oscilloscope in response to the current pulse rise through the water gap. To shield the electric interference from the water breakdown, the pulsed power system and water gap were placed in a Faraday cage, leaving the camera and oscilloscope outside.

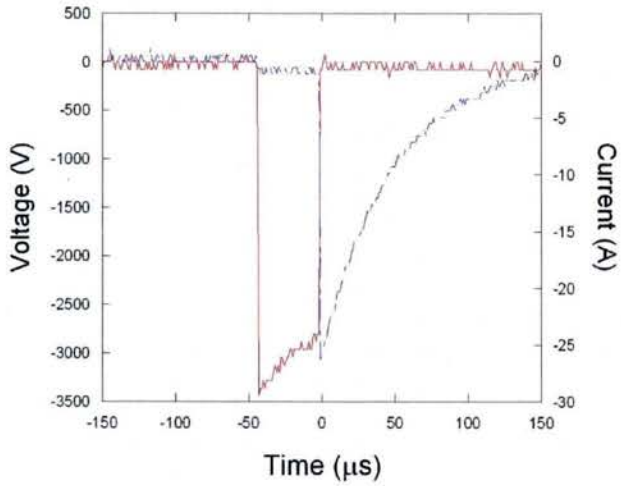

Fig. 3. Voltage measured across the water gap and the resulting current. The peak voltage is approximately −3.5 kV. The water gap breaks down after 48 μs at −2.8 kV at 0 μs causing the increase of current. The decay of the current is given by the RC time constant, 50 μs.

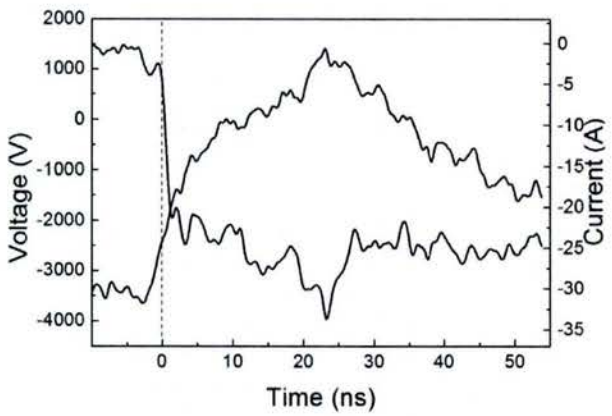

Fig. 4. Voltage and current in a shorter time scale. The current rise time is approximately 10 ns.

IV. Results

A. Voltage and Current

The voltage across the water gap after the MOSFETs are turned ON is governed by the capacitor discharge through the resistor (1.28 kΩ). The peak voltage is approximately 3.5 kV (Fig. 3) but decreases according to the time constant (640 μs and $RC = 1.28\ \text{k}\Omega \times 0.5\ \mu\text{F}$). After approximately 50 μs, the water gap breaks down so the current starts flowing and it decreases exponentially at a new time constant (50 μs and $RC = 100\ \Omega \times 0.5\ \mu\text{F}$). This is a statistical event and the breakdown voltage is approximately 2.8 ± 0.5 kV with a delay time of $40 \pm 10\ \mu$s.

Fig. 4 shows a voltage and current waveform in shorter time scale. In general, the current increases from 0 to 10 ns as the voltage drops. The voltage and current waveform allows us to calculate the resistance of the water gap and the power deposition. In Fig. 5, the water gap resistance drops from >2 kΩ to approximately 900 Ω, which occurs in less than 2 ns (Phase I). The second phase (Phase II) of the resistance drop occurs from −1.4 to 4 ns, during which the resistance

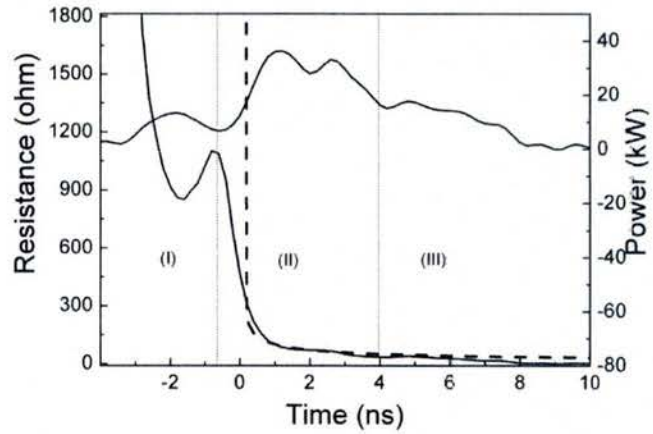

Fig. 5. Resistance of the water gap and the corresponding power deposited in the gap. The data were calculated from the voltage and current in Fig. 4. The dashed line is the resistance fitted as the inverse square root of time. The two dotted lines mark the phase transitions.

becomes the same value of the current-limiting resistance (100 Ω). After that, i.e., in Phase III, the resistance further decreases to a negligible value until >10 ns. Such three-stage development of water gap resistance agrees with the resistance drop reported in [23]. It is in the second phase that the largest amount of power deposited in the water gap (0–4 ns), which according to Fig. 5, has a peak power 30 kW. We note that in the current and voltage waveforms (Fig. 4), the phase boundaries are not so clear. Especially, the current lags the voltage by approximately 2 ns, which suggests the water gap is somewhat inductive. Otherwise, a pure resistive gap should have exhibited synchronous voltage and current. The inaccuracy caused by the inductive element can therefore be estimated as 2 ns. In other words, the temporal error of Phase I transitioning to Phase II is approximately 2 ns. In Fig. 5, the boundaries become clearer indicated by the slope change of the power deposition from phase to phase.

In (9), the resistance develops according to the inverse of square root of time. We fitted this relation in Fig. 5 and drew it as the dashed line

$$R_c(t) = 100/t^{\frac{1}{2}}\,(\Omega). \tag{16}$$

The time t is expressed in nanoseconds. This relation works well in the second and third phases. Clearly, the resistance becomes infinitely large as time approaches zero. However, because the expansion of water arc mainly occurs in the second phase, we will ignore the process prior to 0 ns, in which only small power is deposited in the water gap as the resistance is still large compared with the current-limiting resistance (100 Ω). For our calculation of (1), (2), (8), and (9), the starting time is 0.1 ns, at which, the resistance of the water gap is 316 Ω (16). This value is close to the mean value of the measured values $300 \pm 45\ \Omega$ at this particular instant (0.1 ns).

B. Temporal Development of Shock Wave and Bubble

The temporal development of the postbreakdown in shadow graphs is shown in Fig. 6. Two events, shock wave emission

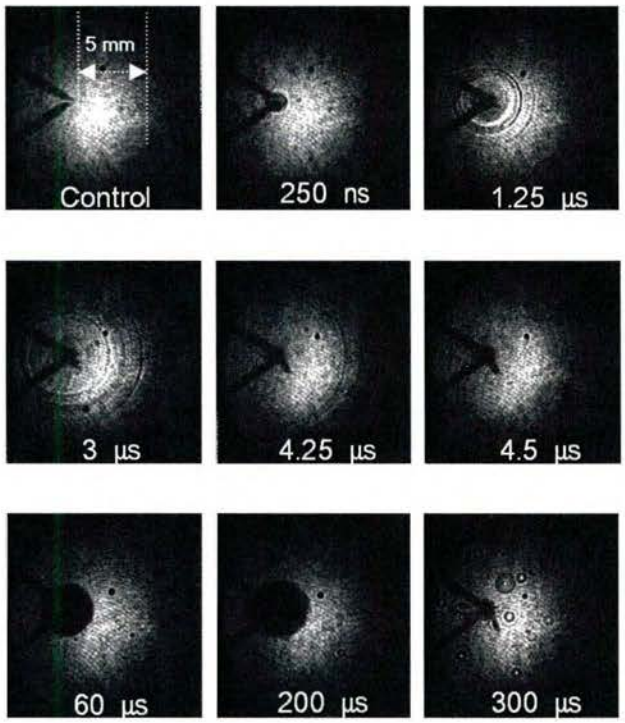

Fig. 6. Laser shadowgraphs of the water gap after breakdown. The time shown is the delay from the breakdown.

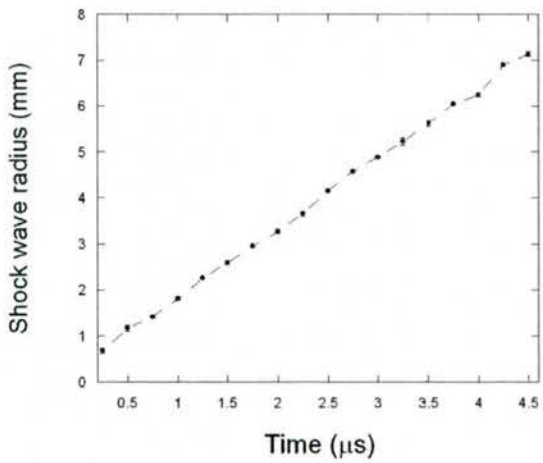

Fig. 7. Shock wave radius taken from Fig. 6 at various delay times.

and bubble expansion are observed. The shock wave expands in the spherical shape, which lasts from 250 ns to 4.5 μs. Within this time, there is still current flow in the water gap between the electrodes (Fig. 3). The radius of the shock wave is shown in Fig. 7. The speed of the shock wave is 1.5 km/s, measured by the slope of the radius.

With the disappearance of shock wave in the imaging window, the bubble grows and reaches its maximum radius at $\sim$150 μs. It then shrinks and collapses into smaller bubbles. The radius of the bubble is shown in Fig. 8. In the growing phase, the radius in the expansion phase (<150 μs, Fig. 8) can be fitted as $r = at^d$ using a graphic tool (Sigma Plot,

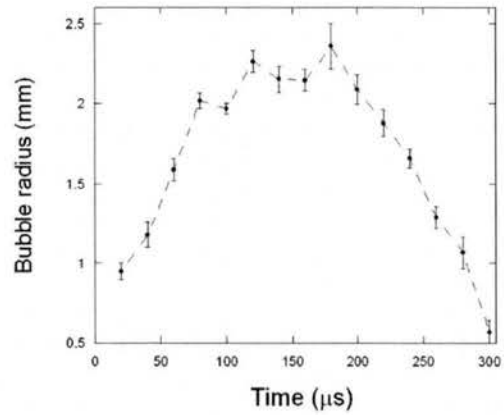

Fig. 8. Bubble radius taken from the images in Fig. 6. At each data point, $N = 5$ images were included and the radius is shown as standard error bar.

regression wizard). The resulted a is 0.2 and d is 0.5

$$r = 0.2t^{0.5}. \tag{17}$$

The unit of r is millimeter and t is microseconds. Alternatively, r can be in meter and t in seconds. The time dependence $t^{0.5}$ is consistent with the experimental observation and similarity analysis [22].

The time interval T_c between the bubble inception and maximum diameter is given by [26]

$$r_{\max} = T_c/0.915(\rho_0/(p_\infty - p_v))^{0.5} \tag{18}$$

where p_v is the vapor pressure inside the bubble (2330 Pa at 20 °C). In Fig. 8, T_c is 150 μs, which leads to $r_{\max} = 1.6$ mm. This radius is close to 2.2 mm, measured in the experiment (Fig. 8).

C. Temporal Development of Water Gap Pressure

The results shown in Fig. 6 summarize the postbreakdown phenomena in the water gap, but the pressure buildup in the bubble (or plasma channel) occurs earlier. The largest power deposition occurs in the breakdown phase (Phase II), as shown in Fig. 5. Equations (1), (2), (8), and (9) allow us to calculate the pressure in the water gap during this phase. Fig. 9 shows the pressure profile within 80 ns starting from $t =$ 0.1 ns. The pressure increases to a peak pressure 1 GPa within 5 ns. This is consistent with Fig. 5, in which the major power is deposited in the first 5 ns. The pressure, however, drops rather rapidly as the water gap resistance becomes negligible compared with the current limiting resistance, causing less power deposition in the gap. The accuracy of the pressure calculation is corroborated by the close agreement of the calculated current with the measured current (Fig. 9).

The peak pressure of the water gap can also be estimated from (14). As shown in Fig. 5, the peak power deposited in the water gap is 30 kW, which occurs in approximately 2 ns. Considering the length of the water gap, which is 0.2 mm, the peak pressure was calculated as 2.2 GPa. This value is rather close to the 1 GPa obtained by solving the energy conservation equations (1), (2), (8), and (9).

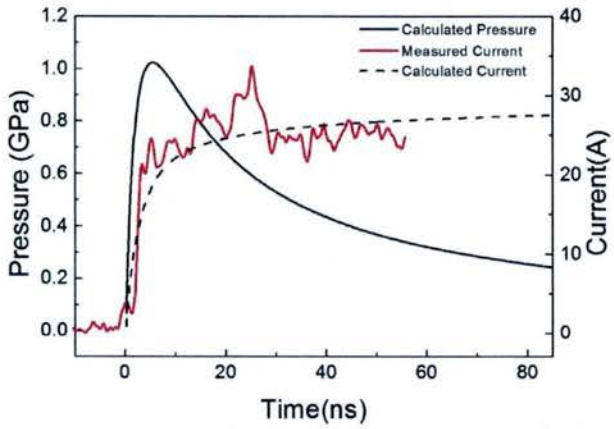

Fig. 9. Pressure development in the water gap in the early stage when its resistance drops to the value close to the current limiting resistance. The calculated and measured currents show a close agreement.

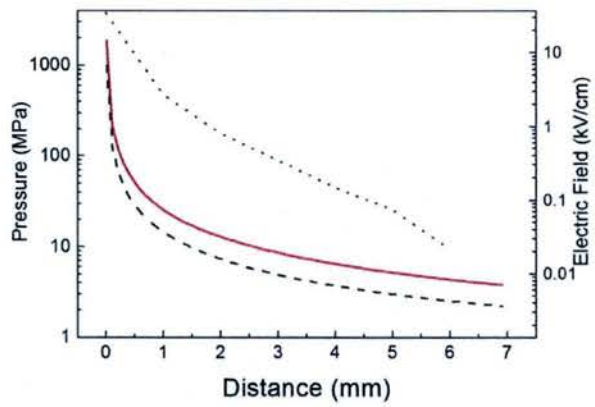

Fig. 10. Pressure generated from the bubble at its maximum pressure (1 GP and 5 ns in Fig. 9) over the distance. Two approaches were used: the red line is the result of using (10) and the dashed line is the result of using (12). Also shown is the electric field calculated from the electrode by applying a voltage of 4 kV (the dotted line).

D. Shock Pressure

The shock pressure generated from the expansion of bubble can be calculated from (10) and (11) or separately from (12). We used the pressure profile of the bubble wall from Fig. 9. The speed of the bubble wall was calculated from (17).

To compare the results of these two approaches, we calculated the pressure wave generated when the bubble pressure reaches the maximum ($t = 5.2$ ns and $P = 1$ GPa in Fig. 9). Fig. 10 shows the pressure field outside the bubble extending to a distance of 7 mm. The pressure drops from 1.1 GPa to 4 MPa at 7 mm, whereas the incompressible approximation yields a pressure 2.5 MPa. Both results are very close, suggesting a simpler expression in (12) can replace the more lengthy expression in (10) and (11).

Since Fig. 9 shows the development of the pressure in the bubble, it allows us to calculate the pressure in the time domain, rather than single time point shown in Fig. 10. We used (12) and read the bubble pressure from Fig. 9, the pressure temporal profile outside the bubble at different distances can be calculated in Fig. 11. We note that the pressure is for an observer at different distances observing the arrival of the pressure wave and the propagation delay is not included. In general, the pressure drops 70% within 400 ns. The trend of pressure decrease over distance approximately follows the inverse of the distance. For example, at 1 mm (870 ns), the pressure is 7 MPa, but it drops to 1 MPa at the distance of 6 mm.

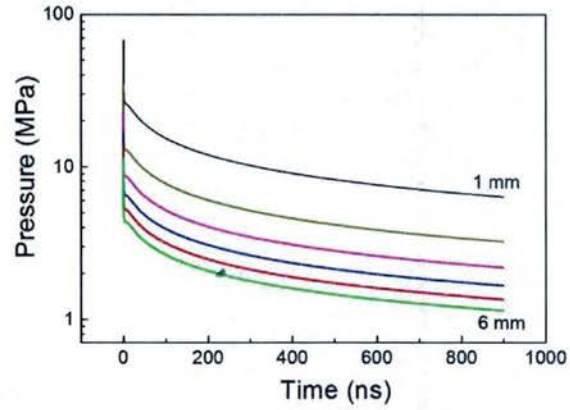

Fig. 11. Temporal development of pressure at different distances (1–6 mm) from the electrode.

The energy carried by the pressure wave was estimated from (13). At the distance of 6 mm, the energy integrated in the time frame (<870 ns in Fig. 11) is 1 mJ, which is the same as that calculated at the distance of 1 mm.

V. Discussion

The radius of the bubble expansion is well described by the power relation (17). The duration from the expansion to shrinkage can also be predicted by a well-established relation (18). Accordingly, the resistance of the water gap can be described by the inverse square root relation (16). Such dependence is consistent with the observation in other liquids.

The pressure increase in the bubble coincides with the increase of current, or more directly, with the increase of power deposition in the water arc, which occurs in less than 10 ns. That points to the importance of using a low-impedance circuit. However, due to the restriction of rated current of MOSFET switches, such low-impedance circuit will have to rely on higher current switches, such as spark gap switches. In our circuit, the time constant before breakdown from the circuit is 640 μs, yet the pressure decreases 70% within the 400 ns. Moreover, the energy carried by the pressure wave is only 1 mJ, which is much less than the total energy stored in the capacitor 4 J. Therefore, we may decrease the capacitance value and reduce the size of the pulse generator.

In estimating the shock pressure, we have used two approaches. One is to calculate from the method of characteristics (10), and the other is to calculate from the approximation of incompressible liquid (12). The drop of the pressure wave over distance is rather close using these two approaches, suggesting a strong dependence on the inverse of distance. On the other hand, the peak pressure in the bubble, calculated

by (1), (2), (8), and (9), is 1 GPa, in the same range as that calculated by a pressure-power relation (14), which is 2.2 GPa.

Our motivation of this paper is to produce shock waves on the coverslip. We have used electric discharges and it takes finite length of time to generate discharge, approximately 50 μs, as shown in Fig. 3. The cells near the electrodes experience not only shock waves, but also pulsed electric fields. Side effects such as electroporation could be present in addition to the biological effects induced by shock waves. We therefore have calculated the electric field dependence over distance (the dotted line in Fig. 10) for a maximum applied voltage of 4 kV. The electric field drops rather rapidly over distance. At a distance of 2 mm, the electric field already drops to 1 kV/cm. However, the threshold for electroporation, as shown by [27], is greater than 1 kV/cm for 50-μs pulses. We therefore rule out electroporation for cells situated beyond 2 mm. For other biological effects considered less in severity, such as action potential activation, a separate control experiment can be performed. In this case, the water gap can be enlarged slightly so that no breakdown occurs. Cells will be only exposed to electric fields so the effective range of shock wave impact can be determined.

Finally, we point out one caveat of using (1), (2), (8), and (9) to calculate the pressure. The fitted resistance of the water gap (16) only works well in the second phase (0–6 ns), as shown in Fig. 5. Beyond that, the actual resistance drops much faster than predicted by (16). Thus, the power deposited in the water gap should be smaller, which suggest the calculated bubble pressure should drop faster. Therefore, the duration of the pressure (70%) can be shorter than 400 ns.

VI. Conclusion

We have used a compact pulsed power generator, which consists of four 1-kV MOSFET switches, to produce shock waves in biological media for biomedical research. Such shock wave system allows cells to expose to shock waves on the microscope, therefore providing a means of real-time measurement of cells response. The pressure increase occurs in the rising time of the current and therefore the circuit impedance needs to be minimized. In general, pressure waves in the range 1–10 MPa with a duration of submicroseconds can be generated by this device. We also would like to point out the predicted pressure needs to be confirmed by measurements.

References

[1] R. O. Cleveland and J. A. McAteer, "Physics of shock-wave lithotripsy," in *Smith's Textbook on Endourology*, A. D. Smith *et al.*, Eds. Hamilton, ON, Canada: BC Decker, 2007, ch. 38, pp. 317–332.

[2] P. Lukes *et al.*, "Focused tandem shock waves in water and their potential application in cancer treatment," in *Proc. 28th Int. Symp. Shock Waves*, 2012, pp. 839–845.

[3] V. Menezes, K. Takayama, A. Gjani, and S. H. R. Hosseini, "Shock wave driven microparticles for pharmaceutical applications," *Shock Waves*, vol. 18, no. 5, pp. 393–400, 2008.

[4] D. Magaña-Ortíz, N. Coconi-Linares, E. Ortiz-Vazquez, F. Fernández, A. M. Loske, and M. A. Gómez-Lim, "A novel and highly efficient method for genetic transformation of fungi employing shock waves," *Fungal Genetics Biol.*, vol. 56, pp. 9–16, Jul. 2013.

[5] S. M. Nejad, S. H. R. Hosseini, H. Akiyama, and K. Tachibana, "Optical observation of cell sonoporation with low intensity ultrasound," *Biochem. Biophys. Res. Commun.*, vol. 413, no. 2, pp. 218–223, 2011.

[6] H. Bluhm, *Pulsed Power Systems, Principles and Applications*. New York, NY, USA: Springer-Verlag, 2006.

[7] J. P. VanDevender, "The resistive phase of a high-voltage water spark," *J. Appl. Phys.*, vol. 49, no. 5, pp. 2616–2620, 1978.

[8] S. Xiao *et al.*, "High power water switches: Postbreakdown phenomena and dielectric recovery," *IEEE Trans. Dielectr. Electr. Insul.*, vol. 11, no. 4, pp. 604–612, Aug. 2004.

[9] J. R. Woodworth, D. Chalenski, G. S. Sarkisov, and J. R. Blickem, "170-kV laser-triggered water switch experiments," *IEEE Trans. Plasma Sci.*, vol. 33, no. 6, pp. 2051–2059, Dec. 2005.

[10] D. Oshita *et al.*, "Time-resolved high-speed visualization and analysis of underwater shock wave focusing generated by a magnetic pulse compression unit," *IEEE Trans. Plasma Sci.*, vol. 40, no. 10, pp. 2395–2400, Oct. 2012.

[11] X. Lu, Y. Pan, K. Liu, M. Liu, and H. Zhang, "Spark model of pulsed discharge in water," *J. Appl. Phys.*, vol. 91, no. 1, p. 24, 2002.

[12] P. Šunka, V. Babický, M. Člupek, and Č. Štuka, "New discharge circuit for efficient shock wave generation," in *Shock Waves in Condensed Matter and Heterogeneous Media*, R. Brun and L. Z. Dumitrescu, Eds. Berlin, Germany: Springer-Verlag, 1995, pp. 455–458.

[13] S. Katsuki, K. Tanaka, T. Fudamoto, T. Namihira, H. Akiyama, and H. Bluhm, "Shock wave due to pulsed streamer discharges in water," in *Proc. Conf. Rec. 26th Int. Power Modulator Symp.*, 2004.

[14] K. Schoenbach, J. Kolb, S. Xiao, S. Katsuki, Y. Minamitani, and R. Joshi, "Electrical breakdown of water in microgaps," *Plasma Sources Sci. Technol.*, vol. 17, no. 2, p. 024010, 2008.

[15] J. F. Kolb, R. P. Joshi, S. Xiao, and K. H. Schoenbach, "Streamers in water and other dielectric liquids," *J. Phys. D, Appl. Phys.*, vol. 41, no. 23, p. 234007, 2008.

[16] R. H. Cole, *Underwater Explosions*. Princeton, NJ, USA: Princeton Univ. Press, 1948.

[17] N. M. Beskaravainyi, V. G. Kovalev, and E. V. Krivitskii, "Scaling variables for high-voltage electrical discharges in gas-liquid mixtures," *Tech. Phys.*, vol. 39, no. 2, pp. 224–225, 1994.

[18] L. K. Warne, R. E. Jorgenson, and J. M. Lehr, "Resistance of a water spark," Sandia National Laboratories, Albuquerque, NM, USA, Tech. Rep. SAND2005–6994, Nov. 2005.

[19] M. C. Hooton, J. R. Blake, and W. K. Soh, "Behaviour of an underwater explosion bubble near a rigid boundary: Theory and experiment," in *Bubble Dynamics and Interface Phenomena*. Norwell, MA, USA: Kluwer, 1994, pp. 421–428.

[20] I. G. Cullis, "Blast waves and how they interact with structures," *J. Roy. Army Med. Corps*, vol. 147, no. 1, pp. 16–26, 2001.

[21] R. Courant and K. O. Friedrichs, *Supersonic Flow and Shock Waves*. New York, NY, USA: Interscience, 1948, ch. 6.

[22] V. Y. Ushakov, *Impulse Breakdown of Liquids*. New York, NY, USA: Springer-Verlag, 2007.

[23] J. Fuhr and W. F. Schmidt, "Spark breakdown of liquid hydrocarbons. II. Temporal development of the electric spark resistance in *n*-pentane, *n*-hexane, 2,2 dimethylbutane, and *n*-decane," *J. Appl. Phys.*, vol. 59, no. 11, pp. 3702–3708, 1986.

[24] F. R. Gilmore, "The growth or collapse of a sphercial bubble in a viscous compressible liquid," Office of Naval Research, Arlington, VA, USA, Tech. Rep. 26-4, Apr. 1952.

[25] R. J. Baker and B. P. Johnson, "Stacking power MOSFETs for use in high speed instrumentation," *Rev. Sci. Instrum.*, vol. 63, no. 12, pp. 5799–5801, 1992.

[26] A. Vogel, S. Busch, and U. Parlitz, "Shock wave emission and cavitation bubble generation by picosecond and nanosecond optical breakdown in water," *J. Acoust. Soc. Amer.*, vol. 100, no. 1, pp. 148–165, 1996.

[27] G. Saulis and R. Saulè, "Comparison of electroporation threshold for different cell lines *in vitro*," *ACTA Phys. Polonica A*, vol. 115, no. 6, pp. 1056–1058, 2009.

Dongkoo Kang Seoul, Korea, in He received the M.E. and Ph.D. degrees from Kumamoto University, Kumamoto, Japan, in 2010 and 2013, respectively.

He is a Post-Doctoral Research Associate with the Frank Reidy Research Center for Bioelectrics, Old Dominion University, Norfolk, VA, USA.

Jong Bong Nah, photograph and biography not available at the time of publication.

Michael Cho is currently a Professor of Bioengineering with the University of Illinois at Chicago, Chicago, IL, USA. To facilitate the research goals, the Laboratory for Biomolecular Imaging, University of Illinois at Chicago, has been established and features five instruments to measure and characterize the biological, mechanical, and optical properties of engineered tissue constructs. He has supervised numerous Ph.D. students, two M.D./Ph.D. students, and many undergraduate students have gained their research experience in his laboratory. He has published a new journal *Physics and Chemistry of Stem Cells*, which he serves on as an Editor-in-Chief. His current research interests include regenerative tissue engineering, cellular biomechanics, and multimodal imaging.

Prof. Cho was a recipient of the University Scholar and Faculty of the Year Awards in 2014. He is a fellow of the American Institute for Medical and Biological Engineering, Washington, DC, USA. His research programs have been funded by several federal agencies, including the Department of Defense, the National Institutes of Health and Department of Energy, and the Whitaker Foundation.

Shu Xiao (M'04–SM'12) received the Ph.D. degree in electrical engineering from Old Dominion University, Norfolk, VA, USA, in 2004.

He was in the Ph.D./master's joint program with the University of Electronic Sciences and Technology of China, Chengdu, China, from 1996 to 2001. He is currently an Assistant Professor with the Department of Electrical and Computer Engineering, Old Dominion University. His current research interests include power electronics, pulse power, electrical discharges in liquid and gas, and manipulation of biological cells with intense electrical pulses.

Journal of Biomechanics 47 (2014) 3650–3656

Contents lists available at ScienceDirect

Journal of Biomechanics

journal homepage: www.elsevier.com/locate/jbiomech
www.JBiomech.com

Impact of oxidative stress on cellular biomechanics and rho signaling in C2C12 myoblasts

Shan Sun [a], Singwan Wong [b], Arthur Mak [b], Michael Cho [a,*]

[a] Department of Bioengineering, University of Illinois at Chicago, Chicago, IL 60607, USA
[b] Division of Biomedical Engineering, The Chinese University of Hong Kong, Shatin, Hong Kong

ARTICLE INFO

Article history:
Accepted 29 September 2014

Keywords:
Oxidative stress
Cytoskeleton
Rho signaling pathway
ERM linker proteins
Cell stiffness
AFM
Superoxide

ABSTRACT

Although cells often can tolerate oxidative environments, abnormal oxidative stress has been identified in inflammation, cardiovascular and neurodegenerative diseases, and aging. The impact of oxidative stress on the cellular biomechanics is poorly understood, however. In this study, we used C2C12 myoblasts to investigate the effect of oxidative stress, mimicked by hydrogen peroxide (H_2O_2), on the cell elasticity (i.e., Young's modulus), viability, and production of intracellular reactive oxygen species (ROS). To better understand the mechanisms underlying the impact of H_2O_2, we examined various effectors of the Rho signaling pathway, which has been shown to play a key role in the control of cell mechanics. H_2O_2 decreased the cell stiffness in a dose-dependent manner, caused cell death, and reduced the RhoA expression that was accompanied by down-regulation of α-actin, cytoskeleton-membrane linker proteins (ezrin–radixin–moesion proteins), and focal adhesion. Modulating the Rho signaling by using a Rho activator partially restored the cell stiffness, enhanced the cell viability, and decreased the intracellular ROS level, suggesting a potential intervention strategy to maintain the cellular biomechanical homeostasis and rescue cell damage in the threat of oxidative stresses.

© 2014 Elsevier Ltd. All rights reserved.

1. Introduction

Cells are subject to oxidative stress in many situations. Normal metabolic activities commonly involve redox processes (Burhans and Heintz, 2009; Gutteridge and Halliwell, 2010), and thus, cells need to cope with potential oxidative stress regularly. Pathological situations arise when the oxidative stress in the cells and their microenvironments exceed the coping capacity, making the in situ cells susceptible to oxidative damages. Oxidative stress has been associated with inflammation (Tidball, 2005), cardiovascular and neurodegenerative diseases (Hebbel et al., 1990; Halliwell, 2000; Coyle and Pattfarcken, 1993), and aging (Sohal et al., 2002). Other examples of high oxidative stress involve post-ischemic reperfusion, such as in the case of neural tissues immediately after ischemic stroke (Aronowski et al., 1997), cardiac tissues after open-heart surgery (Starkopf et al., 1995), or subcutaneous tissues at risk of pressure ulcers after prolonged excessive epidermal loading that compromises tissue microcirculation (Mak et al., 2010).

Cells in oxidative environments often need to continue to sustain mechanical loading. Tendon fibroblasts with tendonitis continue to be stretched repeatedly under inflammatory conditions. Cardiomyocytes need to resume pumping blood immediately following an open-heart surgery. In the cascade of events leading to deep tissue injury and pressure ulcer under epidermal loading, the skin fibroblasts and keratinocytes as well as the underlying adipocytes and skeletal myocytes may likely be reloaded in a reperfusion-induced oxidative environment, if the repeated loading is applied soon after the release of the preceding load-induced ischemia. Most studies on the cell mechanics have typically been conducted with the aim of examining the normal cell mechanics. Although pathological cell mechanics have been reported for blood cells (Finch et al., 1973; Wang et al., 2002; Lam et al., 2007) and cancer cells (Cross et al., 2007; Li et al., 2008), literature on how oxidative stress may affect cell mechanics and in particular the load-carrying capacity of cells is scant. The RhoA, among others, is regulated by redox agents (Aghajanian et al., 2009; Nimnual et al., 2003), and this mechanotransduction pathway is expected to influence the cellular biomechanics. We therefore undertook this study to elucidate how an increase in oxidative stress introduced by adding hydrogen peroxide to the culture media could affect the cellular mechanics, cell viability, and production of reactive oxygen species (ROS) in mouse myoblasts. Mechanistically, the Rho signaling is known to play a key role in the control of cell mechanics. However, the role of various effectors of the Rho signaling pathway, including actin, vinculin,

* Correspondence to: Department of Bioengineering, University of Illinois at Chicago, 851 S. Morgan St. (M/C 063), Chicago, IL 60607. Tel.: +312 413 9424; fax: +312 996 5921.
E-mail address: mcho@uic.edu (M. Cho).

http://dx.doi.org/10.1016/j.jbiomech.2014.09.036
0021-9290/© 2014 Elsevier Ltd. All rights reserved.

ezrin–radixin–moesion (ERM) linker proteins, remains to be elucidated. In addition, we further examined whether the upstream regulator (e.g., RhoA) modulated these effectors and correlated with cell death and, thus, suggesting a potential application of biomechanically strengthening the cells under the threats of oxidative challenges.

2. Materials and method

2.1. Cell culture and H_2O_2 treatment

Mouse-derived C2C12 myoblasts (kindly provided to us by Prof. T-C He) were cultured in complete media consisting of Dulbecco's modified eagle's medium supplemented with 10% fetal bovine serum, 1% antibiotics/antimycotics (final concentration; penicillin 100 units/ml, streptomycin 100 μg/ml, and amphotericin B 0.25 μg/ml), in a humidified atmosphere with 5% CO_2 at 37 °C, with media changed twice per week. Passages between 3 to 9 were used for all experiments. For dose-dependent treatment of oxidative stress, C2C12 cells were treated for 24 h with prepared dilutions of H_2O_2 in a cell culture medium resulting in the final concentration range from 0 to 2 mM. These dosages were based on the DNA fragmentation associated with apoptotic cell death as previously reported (Siu et al., 2009).

2.2. Measurement on cell stiffness using AFM

An atomic force microscope (AFM; Novascan Technologies, Ames, IA) was used to measure the biomechanical properties of individual mouse myoblasts. Full experimental details have been provided elsewhere (Titushkin and Cho, 2007; Titushkin and Cho, 2011; Titushkin et al., 2013; Sun et al., 2013). Briefly, to obtain a force–distance curve, an AFM cantilever (0.12 N/m) with a 5-μm radius microindentor descended toward the cell at ~2 mm/s to minimize hysteresis and until a trigger force of 3 nN was reached. The force–distance curves were then analyzed according to the Hertz model (Radmacher, 2002). The average Young's modulus for each experimental condition was calculated and subjected to t-test at the level of $\alpha = 0.05$.

2.3. Cell viability

C2C12 cells were placed in a 96-well plate to yield a density of 1×10^5 cells/ml and incubated overnight. The original medium was then replaced by fresh medium containing various concentration of H_2O_2 (0–2 mM) with or without Rho activator II (Cytoskeleton, Denver, CO). Cell survival rate was determined using the Cell Counting Kit 8 (CCK-8, Sigma-Aldrich, St. Louis, MO), which provides a higher detection sensitivity than, for example, tetrazolium salts, such as MTT or MTS. A 10-μl CCK-8 solution was added to the cells 24 h post-treatment and incubated for 4 h at 37 °C. Absorbance of each well was quantified at 450 nm using a plate reader (BioTek Instruments Inc., Winooski, VT). The cell survival was represented by the optical absorbance under each experimental condition.

2.4. Superoxide labeling

Mitosox (Life Technologies, Grand Island, NY) was used to label superoxide inside the cells. This novel, membrane-permeable fluorophore preferentially targets mitochondria. Upon oxidation by superoxide, the dye fluoresces with the emission maximum at 580 nm. Myoblasts were treated with H_2O_2 or Rho activator II and then incubated with 1 μM Mitosox for 30 min at 37 °C. Cells were extensively washed and immediately mounted on the microscope stage for imaging.

3. Results

Schematically shown in Fig. 1A, individual cell stiffness was quantitatively measured using AFM-based microindentation. A typical force–deformation curve (Fig. 1B) demonstrates that as the AFM probe slowly indents a surface, hard substrate quickly deflects the tip and causes a sharp rise in the force–deformation curve. In contrast, a gradual rise in the curve is representative of relatively soft substrate, such as the cell. Microindentation results showed that the stiffness of normal C2C12 cells is ~3 kPa. The cell stiffness was found to decrease in response to the H_2O_2 treatment for 24 h in a concentration-dependent manner (Fig. 1C). At the H_2O_2 concentration as low as 0.2 mM, the cell stiffness was only slightly reduced but not statistically significant. The cells became mechanically softer ($p < 0.05$) after the H_2O_2 concentrations were increased to > 0.5 mM,, presumably due to cytoskeletal reorganization. We also observed that at the highest H_2O_2 concentration (2 mM) used in our experiments, cells were either broken into debris or shrunk into much smaller spherical cells that were too easily detached. In such a case, no AFM measurements could be properly interpreted (data not shown).

Although actins are primarily responsible for maintaining the cell stiffness, focal adhesion can also contribute to the cellular biomechanics. We therefore fluorescently visualized actin and vinculin, a key protein found in the focal adhesion, and nuclei in response to the H_2O_2 treatment. In a control experiment, actin stress fibers were noticeably present, as expected. In addition, multiple focal adhesions were visualized in the control cells and preferentially located at the ends of actin stress fibers (Fig. 2A). Consistent with the cell stiffness measurement shown in Fig. 1C, the treatment of mouse myoblasts with 0.2 mM H_2O_2 did not show discernible changes in the actin organization or focal adhesions (Fig. 2B). At 0.5 mM H_2O_2, the actin fibers appeared slightly weaker in fluorescence intensity and shorter in length (Fig. 2C). However, as the H_2O_2 concentration increased to 1 mM, the actin stress fibers were no longer clearly delineated, and the focal adhesions as assessed by the vinculin punctates were diminished in numbers as well as fluorescence intensity (Fig. 2D). At the 2- mM concentration, cells could no longer maintain the proper morphology, became smaller in size, and readily detached from the substrate (Fig. 2E). A quantitative assay indicates a significant reduction in the vinculin expression as a function of the increasing H_2O_2 concentration (Fig. 2F). These findings suggest that oxidative damage mimicked by H_2O_2 disorganizes the actin stress

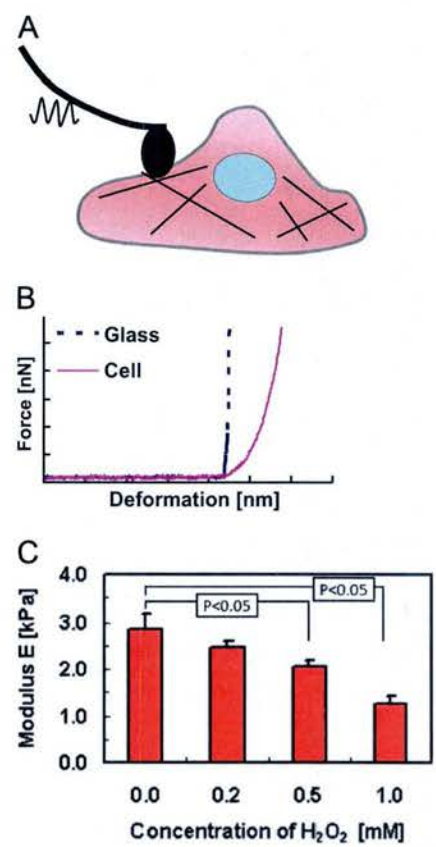

Fig. 1. Measurement of Young's modulus. (A) Schematic drawing showing an AFM probe descending on the cell. (B) A typical force–deformation curve is obtained from each AFM measurement. (C) Mean ± SEM Young's moduli of 60 to 80 C2C12 cells 24 h post-treatment of varying H_2O_2 concentrations from 3 to 4 independent experiments.

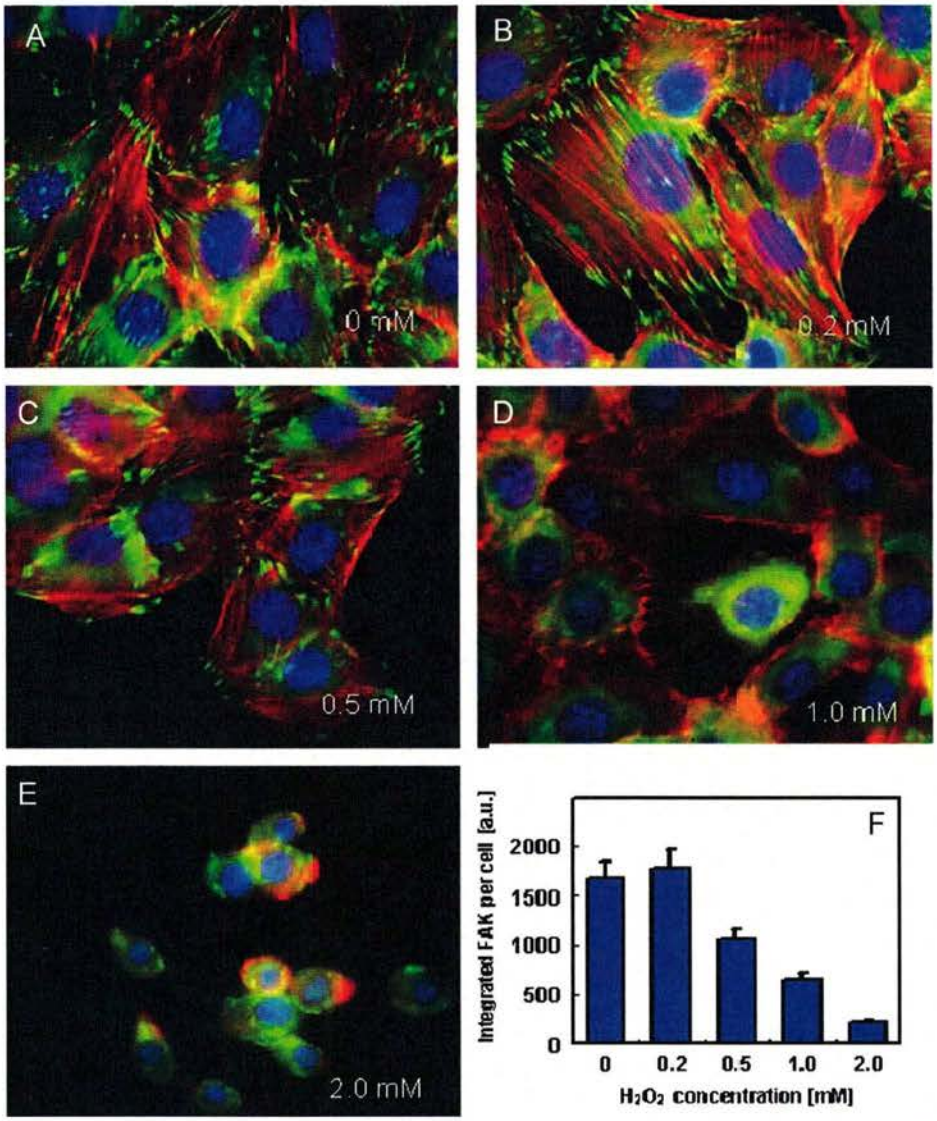

Fig. 2. Three-color imaging of C2C12 cells. Actin (red), vinculin (green), and nucleus (blue) were fluorescently visualized in control cells (A) and in response to 0.2 (B), 0.5 (C), 1 (D), and 2 mM (E) H_2O_2 treatment for 24 h. Images were acquired using a 60× objective. A quantitative assay was applied to measure the vinculin expression and to represent the focal adhesions (F).

fibers and focal adhesions in myoblasts in a concentration-dependent manner, and that these subcellular changes are accurately reflected by AFM-based microindentation measurement of the cell stiffness.

As α-actin is expressed in skeletal muscle, we measured its expression in C2C12 myoblasts using Western blot. The α-actin expression decreased as a function of the H_2O_2 concentration, and its bands became almost invisible in response to the 1 or 2 mM H_2O_2 (Fig. 3A) and appear to correlate with the cell stiffness. To further examine the mechanisms underlying the H_2O_2-induced oxidative stress, we measured the expression of RhoA, and the family of phosphorylated linker proteins (p-ERM). Similar to the changes in the α-actin expression, both the RhoA and p-ERM expressions also decreased in a concentration-dependent manner. At the H_2O_2 concentration > 1.0 mM, these mechanosensitive molecules were barely detectable. Such decreases in the proteins' expressions may be due to cell detachment and subsequent death. We therefore repeated Western blot experiments using the cells remaining attached to the substrate only. Although not as pronounced, both the RhoA and the α-actin expressions demonstrated a similar trend of down-regulation in response to the H_2O_2 treatment (Fig. 3B). Using the Rho activator II in increasing concentrations (1–2 μg/ml), it is apparent that the expressions of RhoA and α-actin were restored in the presence of oxidative stress (Fig. 3C).

Hydrogen peroxide was found to decrease the cell viability in a concentration-dependent manner. The cell viability was reduced by approximately 2-fold when myoblasts were exposed to 1 mM H_2O_2, and only an insignificant fraction of cells was found viable in response to 2 mM H_2O_2 (Fig. 4A). We next tested the role of RhoA involved in the regulation of cell viability. A decrease in the cell viability in response to the H_2O_2 treatment was found to be partially reversible by the Rho activation, which suggests that RhoA activation counteracts the effect of the H_2O_2 oxidative stress (Fig. 4A). At as high as 1 mM H_2O_2 concentration, the Rho activation appeared to provide some protective measures and statistically improved the cell viability. At the 2-mM concentration, virtually all cells were detached from the substrate and no interpretable data were obtained, indicating that increased Rho activity was not sufficient to rescue the cells from severe oxidative stress. The rescue of cells from oxidative damage by Rho activation

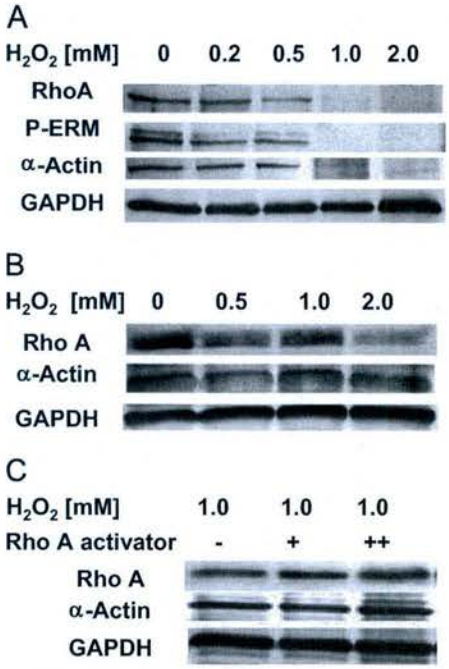

Fig. 3. Western blot analysis of RhoA, p-ERM proteins, and α-actin. (A) Treatment of cells with various H_2O_2 concentrations down-regulated the RhoA, p-ERM, and α-actin in a dose-dependent manner. (B) The protein's expressions were measured using the cells remaining attached to the substrate only following the H_2O_2 treatment. (C) Upregulation of RhoA and α-actin using the Rho activator II at 1 (+) and 2 (++) μg/ml in the presence of 1 mM H_2O_2.

would be expected to correlate with restoration of the cellular biomechanical properties. Consistent with the role of RhoA as a mechanotransducer, the Rho activation caused the cells to become stiffer and, in response to the oxidative stress, Young's modulus resembled that found in control cells (Fig. 4B). From a mechanical point of view, the Rho activation restored the biomechanical properties of C2C12 cells in the presence of oxidative stress.

We have recently reported the family of linker proteins (ERM proteins) that physically couple the cytoskeleton to plasma membrane are involved in the regulation of cellular biomechanics (see Titushkin et al., 2010b for review). To test the role of the ERM proteins in myoblasts, siRNA ERM was applied and their expressions were transiently suppressed (> 90% transfection efficiency). Incubation of C2C12 cells with H_2O_2 for 24 h could not be carried out when the ERM proteins were knocked down. Cells typically became detached from the substrate and a maximum of only 5 h incubation was experimental feasible, suggesting that the cytoskeleton–membrane coupling mediated by the ERM proteins regulates cell adhesion and likely cellular biomechanics. As expected, the ERM knockdown alone decreased the cell stiffness by ~35% (Fig. 5). To be consistent, scrambled siRNA was used as control for 5 h incubation with 1 mM H_2O_2. When siRNA ERM was applied prior to exposure to the 1 mM H_2O_2 treatment, no further decrease in the cell stiffness was observed, implying that the H_2O_2-induced cytoskeletal reorganization (e.g., cell softening) may be preceded by decoupling the cytoskeleton and plasma membrane.

One of the likely signaling pathways that mediate the effect of H_2O_2 may be ROS-induced ROS release (RIRR). The mitochondrial membrane potential could become unstable, and redox transition can occur in response to external insults that typically lead to adverse consequences for mitochondrial potential and cell viability. To validate such mechanism in myoblasts, we treated the cells first with oxidative damage and then visualized the production of superoxide using a dye (Mitosox) that fluoresces upon oxidation. In control cells, the superoxides typically formed small clusters around the nucleus (Figs. 6A and D). In response to the 1.0- mM H_2O_2 treatment, the expression of superoxide was increased, and the dye was capable of penetrating into the nucleus (Figs. 6B and E), providing evidence for RIRR. When cells were treated with 1.0 mM H_2O_2 and Rho activator II, the superoxide expression and distribution were partially restored and resembled those observed in the control cells (Figs. 6C and F).

4. Discussion

In this study, we investigated the role of Rho signaling in response to oxidative stress using H_2O_2 treatment and determined

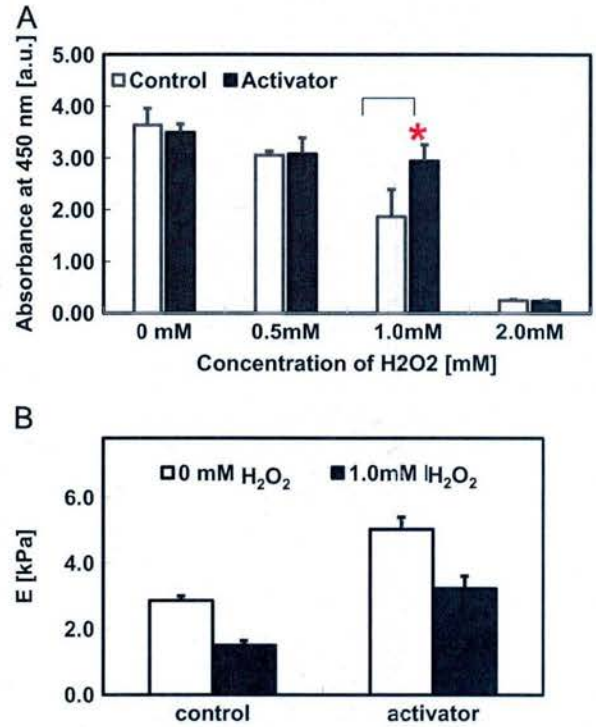

Fig. 4. Cell viability and stiffness. (A) Control cells were treated with varying H_2O_2 concentrations but without Rho activation (open bars). The Rho activator II together with various H_2O_2 concentrations were applied to the cells (black bars). At the 2-mM H_2O_2 concentration, the cell viability could not be reversed by the Rho activation. (B) Changes in the cell stiffness appear to correlate with the cell viability. * indicates $p < 0.05$.

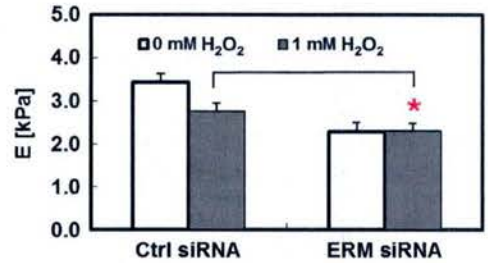

Fig. 5. Modulated biomechanics of C2C12 cells by ERM proteins. Treatment of cells with scrambled siRNA did not significantly change the cells stiffness, as expected. However, siRNA ERM treatment decreased Young's modulus by 35% even without applying H_2O_2 (open bars). Because treatments with both H_2O_2 and siRNA ERM for 24 h could not keep the cells attached, the incubation time was decreased to 5 h only (solid bars). With scrambled siRNA applied, the cell stiffness in response to a shorter H_2O_2 incubation time decreased by ~20%. No further decrease was observed following both siRNA ERM treatment and a 5-h H_2O_2 incubation. Data represent mean ± SEM of 60 to 80 C2C12 cells from 3 to 4 independent experiments.

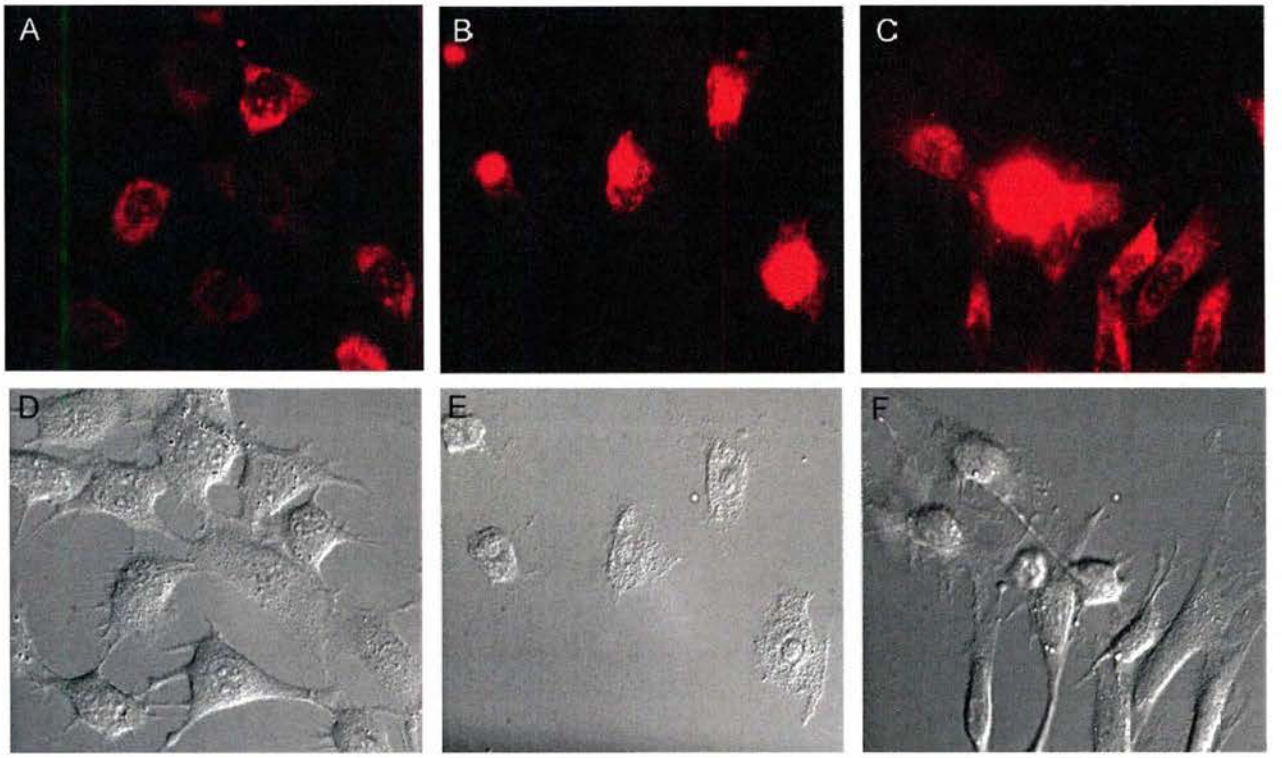

Fig. 6. Production of intracellular superoxide. Mitosox (1 μM) was used to visualize intracellular superoxide in control cells (A, D) and in cells treated with 1 mM H_2O_2 alone (B, E) and in the combination of 1 mM H_2O_2 and 1 μg/ml Rho activator II (C, F).

changes in the cellular biomechanics and cell viability. In addition to actin disassembly in C2C12 myoblasts, we also found that oxidative stress could disrupt focal adhesion and cytoskeleton–membrane association in a dose-dependent manner, and produce ROS (e.g., superoxide). These mechanical events all contribute to the altered cellular biomechanics. Moreover, the viability of C2C12 myoblasts was protected by the Rho activity and correlated with recovery in the cellular mechanics following an oxidative damage

H_2O_2 is an oxidant that can induce cellular damage in a concentration-dependent manner. It may cause apoptosis in C2C12 cells (Siu et al., 2009), induce fragmentation of the mitochondria reticulum of C2C12 cells (Fan et al., 2010), and produce ER stress (Pierre et al., 2014). RIRR is now accepted as a common mechanism for ROS generation that is regulated by the cell's scavenger system to maintain the ROS homeostasis (for review, see Zinkevich and Gutterman, 2010). Biomechanically, it is interesting to note that atheroprotective flow decreases intracellular ROS level, while atheroprone flow induces the opposite (Dai et al., 2007). As the ROS generation appears to follow an altered biomechanics, its intracellular level may be modulated by changes in the cellular biomechanics. In our study, all the effects attributed to H_2O_2 are regulated by or depend on the Rho signaling, and the effect of H_2O_2 treatment on the three mechanotransducers (RhoA, ERM proteins, and α-actin) should correlate in a concerted manner (see Fig. 3).

As RhoA is a member of the GTPase family that has been shown to control actin stress fibers and focal adhesions (Titushkin and Cho, 2011; Titushkin et al., 2010a, 2010b), its activation may stabilize actins and form stress fibers and subsequently regulate cellular cytoskeleton and morphology. The important role of cytoskeleton has been repeatedly demonstrated, particularly for the load-bearing cell types, such as muscle cells. It is likely involved in the regulation of intracellular signaling to respond dynamically to a changing extracellular environment. This cytoskeleton function has often been attributed, among many others, to the Rho family. Although complex interactions between the Rho GTPases and downstream target molecules have been extensively studied, the current study sheds light on the role of RhoA on several structural proteins (vincluin, ERM proteins, and α-actin). These mechanosensitive proteins likely coordinate their responses through the Rho signaling pathway when challenged by oxidative stress, and alter the cellular biomechanics.

The cell membrane not only conforms closely to the cytoskeleton, but it also is physically associated with the underlying cytoskeletal structures (Titushkin and Cho, 2009). Evidence indicates that interactions between the cytoskeleton and the lipid bilayer, mediated by specific linkers (i.e., ERM proteins), are a major factor determining the mechanical properties of the cell membrane, such as membrane tension. The three closely related ERM proteins serve as general crosslinkers between the cell membrane and actin filaments and organize the cytoskeleton in many cell types (Fehon and MaClatchey, 2010; Neisch and Fehon, 2011; Arpin et al., 2011). Both RhoA-dependent and RhoA-independent ERM activation mechanisms have been suggested. Interestingly, energy depletion of cells causes membrane separation from cytoskeleton and bleb formation (Titushkin and Cho, 2009), which is also thought be mediated by inhibition of the ERM linker proteins. Changes in the cellular biomechanics through interfering with the function of ERM proteins have been observed. For example, our laboratory reported that transient knockdown of ERM proteins can inhibit or promote stem cell differentiation. Osteogenesis can be significantly delayed or even inhibited by down-regulation of ERM proteins (Titushkin and Cho, 2011), whereas adipogenesis appears to be facilitated (Titushkin et al., 2013).

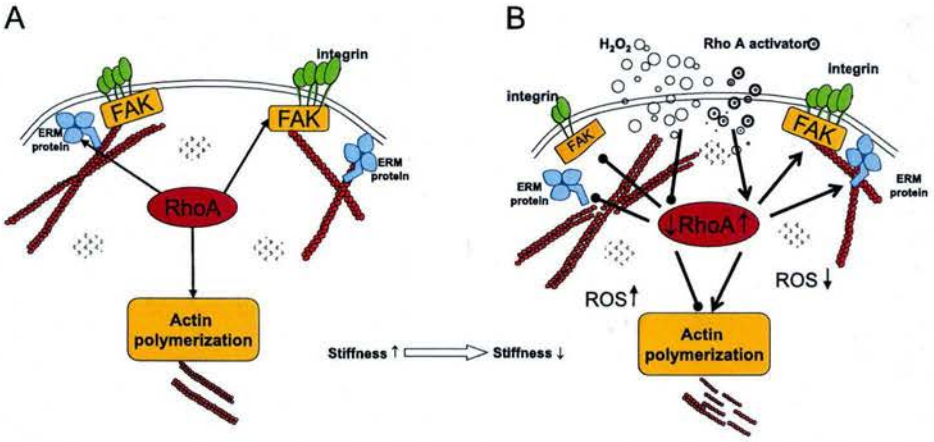

Fig. 7. Schematic for biomechanical changes by oxidative stress. (A) Endogenous RhoA activity maintains proper biomechanical homeostasis in C2C12 cells. (B) External factors, such as H_2O_2, adversely affect the RhoA activity, which, in turn, reorganizes actin stress fibers, disassembles focal adhesions, decouples the cytoskeleton from the cell membrane by inhibiting the ERM proteins, and increases the intracellular ROS production. All of the processes contribute to the overall cellular biomechanics and correlate with the cell viability. Activation of the Rho molecules is postulated to compete against these effects, including a decrease in the intracellular ROS level, and partially restores the cellular biomechanics and enhances cell viability.

Based on our collective findings, we propose a working model as illustrated in Fig. 7. Although this model is not intended to represent a complete list of possible multiple pathways that are influenced by hydrogen peroxide-induced oxidative stress, the cell viability and altered biomechanical properties of C2C12 cells may be regulated through the Rho molecules, the focal adhesions, and the linker ERM proteins. The cell viability is reflected by and correlated with the altered cellular biomechanics. In addition to actin stress fibers, the overall cellular biomechanics is determined by focal adhesions and association between the cytoskeleton and the plasma membrane that is mediated by the ERM proteins. Hydrogen peroxide could directly affect the focal adhesion and ERM proteins, or indirectly affect them through RhoA. Although this study is not designed to delineate them, it is clear that the cellular biomechanics can be altered by one or, more likely, a combination of effectors impacting the focal adhesion and ERM proteins, which contribute to regulate the biomechanical homeostasis in response to oxidative stress. Finally, the production of intracellular ROS through the RIRR mechanism may be partially reversed by activating the Rho pathways. It is therefore envisioned that treatments targeting the Rho signaling pathway could potentially be applied to diseases caused by oxidative stress.

Conflict of interest

None

Acknowledgments

This work was supported in part by a grant (N00014-13-1-0404) from the Office of Naval Research. The authors thank Prof. T-C He at the University of Chicago for providing mouse C2C12 myoblasts.

References

Aghajanian, A., Wittchen, E.S., Campbell, S.L., Burridge, K., 2009. Direct activation of RhoA by reactive oxygen species requires a redox-sensitive motif. PLoS One 4, e8045.

Aronowski, J., Strong, R., Grotta, J.C., 1997. Reperfusion Injury: demonstration of brain damage produced by reperfusion after transient focal ischemia in rats. J. Cereb. Blood Flow Metab. 17, 1048–1056.

Arpin, M., Chirivino, M., Naba, A., Zwaenepoel, I., 2011. Emerging role for ERM proteins in cell adhesion and migration. Cell Adhes Migration 5, 199–206.

Burhans, W.C., Heintz, N.H., 2009. The cell cycle is a redox cycle: linking phase-specific targets to cell fate. Free Radic. Bio. Med. 47, 1282–1293.

Coyle, J.T., Pattfarcken, P., 1993. Oxidative stress, glutamate, and neurodegenerative disorders. Science 262, 689–695.

Cross, S.E., Jin, Y.S., Rao, J.Y., Gimzewskj, J.K., 2007. Nanomechanical analysis of cells from cancer patients. Nat. Nanotech. 2, 780–783.

Dai, G., Vaughn, S., Zhang, Y., Wang, E.T., Garcia-Cardena, G., Gimbrone Jr., M.A., 2007. Biomechanical forces in atherosclerosis-resistant vascular regions regulate endothelial redox balance via phosphoinositol 3-Kinase/Akt-dependent activation of Nrf2. Circ. Res. 101, 723–733.

Fan, X., Hussien, R., Brooks, G.A., 2010. H_2O_2-induced mitochondrial fragmentation in C2C12 myocytes. Free Radic. Biol. Med. 49, 1646–1654.

Fehon, R.G., MaClatchey, A.I., 2010. Organizing the cell cortex: the role of ERM proteins. Nat. Rev. Molec. Cell Biol. 11, 276–287.

Finch, J.T., Perutz, M.F., Bertles, J.F., Dobler, J., 1973. Structure of sickled erythrocytes and of sickle-cell hemoglobin fibers. Proc. Nat. Acad. Sci. 70, 718–722.

Gutteridge, J.M., Halliwell, B., 2010. Antioxidants: Molecules, medicines, and myths. Biochem. Biophys. Res. Commun. 393, 561–564.

Halliwell, B., 2000. Lipid peroxidation, antioxidants, and cardiovascular disease: how should we move forward? Cardiovasc. Res. 47, 410–418.

Hebbel, R.P., Leung, A., Mohandas, N., 1990. Oxidation-induced changes in microrheologic properties of the red blood cell membrane. Blood 76, 1015–1020.

Lam, W.A., Rosenbluth, M.J., Fletcher, D.A., 2007. Chemotherapy exposure increases leukemia cell stiffness. Blood 109, 3505–3508.

Li, Q.S., Lee, G.Y., Ong, C.N., Lim, C.T., 2008. AFM indentation study of breast cancer cells. Biochem. Biophys. Res. Comm. 374, 609–613.

Mak, A.F.T., Zhang, M., Tam, E.W.C., 2010. Biomechanics of pressure ulcer in body tissues interacting with external forces during locomotion. Ann. Rev. Biomed. Eng. 12, 29–53.

Neisch, A.L., Fehon, R.G., 2011. Ezrin, Radixin and Meosin: key regulators of membrane-cortex interactions and signaling. Curr. Opin. Cell Biol. 23, 377–382.

Nimnual, A.S., Taylor, L.J., Bar-Sagi, D., 2003. Redox-dependent downregulation of Rho by Rac. Nat. Cell Biol. 5, 236–242.

Pierre, N., Barbe, C., Gilson, H., Deldcque, L., Raymacker, J.M., Francaux, M., 2014. Activation of ER stress by hydrogen peroxide. Biochem. Biophys. Res. Comm. 450, 459–463.

Radmacher, M., 2002. Measuring the elastic properties of living cells by the atomic force microscope. Methods Cell Biol. 68, 67–90.

Siu, P.M., Wang, Y., Always, S.E., 2009. Apoptotic signaling induced by H_2O_2-mediated oxidative stress in differentiated C2C12 myotubes. Life Sci 84, 468–481.

Sohal, R.S., Mockett, R.J., Orr, W.C., 2002. Mechanisms of ageing: an appraisal of the oxidative stress hypothesis. Free Radic. Biol. Med. 33, 575–586.

Starkopf, J., Zilmer, K., Vihalemm, T., Kullisaar, T., Zilmer, M., Samarutel, J., 1995. Time course of oxidative stress during open-heart surgery. Scand. J. Thor. Cardiovasc. Surg. 29, 181–186.

Sun, S., Song, Z., Cotler, S., Cho, M., 2013. Biomechanics and functionality of hepatocytes in liver cirrhosis. J. Biomech., http://dx.doi.org/10.1016/j.jbiomech.2013.10.050.

Tidball, J.G., 2005. Inflammatory processes in muscle injury and repair. Am. J. Physiol. Reg. Integr. Comp. Physiol. 288, R345–R353.

Titushkin, I., Cho, M., 2007. Modulation of cellular mechanics during osteogenic differentiation of human mesenchymal stem cells. Biophys. J. 93, 3693–3702.

Titushkin, I., Cho, M., 2009. Regulation of cell cytoskeleton and membrane mechanics by electric field: role of linker proteins. Biophys. J. 96, 717–728.

Titushkin, I., Shin, J.S., Cho, M., 2010a. A new perspective for stem cell mechanobiology: biomechanical control of stem cell behaviors and fate. Crit. Rev. Biomed. Eng. 38, 393–433.

Titushkin, I., Sun, S., Shin, J.S., Cho, M., 2010b. Physicochemical control of adult stem cell differentiation: shedding light on potential molecular mechanisms. J. Biomed. Biotech., http://dx.doi.org/10.1155/2010/743476.

Titushkin, I., Cho, M., 2011. Altered osteogenic commitment of human mesenchymal stem cells by ERM protein-dependent modulation of cellular biomechanics. J. Biomech. 44, 2692–2698.

Titushkin, I., Sun, S., Paul, A., Cho, M., 2013. Control of adipogenesis by Ezrin, Radixin and Moesin-dependent biomechanics remodeling. J. Biomech. 46, 521–526.

Wang, J.C., Turner, M.S., Agarwal, G., Kwong, S., Josephs, R., Ferrone, F.A., Briehl, W.R., 2002. Micromechanics of isolated sickle cell hemoglobin fibers: bending moduli and persistence lengths. J. Mol. Biol. 315, 601–612.

Zinkevich, N.S., Gutterman, D.D., 2010. ROS-induced ROS release in vascular biology: redox-redox signaling. Amer. J. Physiol. 301, H647–H653.

JOURNAL OF NEUROTRAUMA 32:1–8 (XXXX 00, 2015)
© Mary Ann Liebert, Inc.
DOI: 10.1089/neu.2014.3699

Characterization of Subcellular Responses Induced by Exposure of Microbubbles to Astrocytes

Shan Sun,[1] Johnwesly Kanagaraj,[1] Lindsey Cho,[2] Dongkoo Kang,[3] Shu Xiao,[3] and Michael Cho[1]

Abstract

Blast traumatic brain injury (bTBI) has now been identified to associate with adverse health consequences among combat veterans. Post-traumatic stress disorder linked with explosive blasts, for example, may result from such brain injury. The fundamental questions about the nature, diagnosis, and long-term consequences of bTBI and causative relationship to post-traumatic stress disorder remain elusive, however. A better understanding of brain tissue injury requires elucidation of potential mechanisms. One such mechanism may be generation of microcavitation bubbles in the brain after an explosive blast and their subsequent interaction with brain cells. Using a controlled electrical discharge system, we have successfully generated shock waves ($\sim$10 MPa) and microbubbles (20–30 μm) in the cell culture of mouse astrocytes. Detachment of astrocytes from the substrate after exposure to microbubbles was observed, and it depended on repetitive exposures. Of the cells that survived the initial assault, several subcellular changes were monitored and determined using fluorescent microscopy, including cell viability, cytoskeletal reorganization, changes in focal adhesion, membrane permeability, and potential onset of apoptosis. While the astrocytes impacted by the shock wave only demonstrated essentially unaltered cellular behavior, the astrocytes exposed to microbubbles exhibited significantly different responses, including production of reactive oxygen species by collapse of microbubbles. In the present study, we characterized and report for the first time the altered biophysical and subcellular properties in astrocytes in response to exposure to the combination of shock waves and microbubbles.

Key words: astrocytes; atomic force microscope; fluorescent microscopy; microbubbles; principle of symmetry; shock waves

Introduction

According to the Centers for Disease Control and Prevention, approximately 1.7 million Americans sustained traumatic brain injury (TBI) between 2002 and 2006. Mild TBI, which accounts for 75% of annual TBI cases,[1,2] has been linked to progressive neurodegeneration and neurosomatic damage leading to cognitive deficits. Blast-induced mild TBI now represents a serious challenge to military combat troops.[3] One recent estimate suggests that approximately 320,000 troops suffered mild TBI (e.g., concussion) in Iraq and Afghanistan by 2008.[4] Definitive diagnosis of mild TBI is difficult, because symptoms can often be confused with other medical conditions.[2,3] Primary TBI diagnosis includes qualitative assessment of the cranium and the use of the Glasgow Coma Scale (GCS) scoring system that relies on the clinician's observation of verbal and motor skills.

Intracranial pressure, CT scan, and MRI are also used to assess brain trauma.[5] Surprisingly, CT imaging and MRI may not detect mild TBI-related damage.[2] For example, CT scans are abnormal in fewer than 10% of mild TBI cases, and the diagnostic capabilities of conventional MRI are also limited. It is recently noted that diffusion tensor imaging may be able to better quantify and aid in diagnosis of axonal injury or shearing trauma. In addition, functional MRI can help to identify physiological and biochemical parameters associated with mild TBI. While imaging diagnostics continues to improve, a clearer understanding of the impact of blast TBI at the cell and tissue level would be crucial for the development of validated and unambiguous diagnosis and subsequent treatment strategies.

Biological responses related to and induced by explosive blasts can manifest themselves in brain tissue injury. Energy from shock waves caused by explosion (e.g., improvised explosive devices) is believed to transfer to the brain through several modes.[6] Compression of the skull plates is possible, but other modes, such as pressurization of intravascular blood and stress from rapid severe head movement, cannot be ruled out. Blast may push the blood into

[1]Department of Bioengineering, University of Illinois at Chicago, Chicago, Illinois.
[2]Department of Kinesiology and Community Health, University of Illinois at Urbana-Champaign, Urbana, Illinois.
[3]Department of Electrical and Computer Engineering, Old Dominion University, Norfolk, Virginia.

closed cranial vaults and canals and increase local pressures. Radiofrequency and infrared energies may also result from explosion, and the electromagnetic radiation may interact with highly electrically active organs such as the brain.[7–9] Accelerated head movement is interesting in that shearing may be produced and lead to axonal injury.

More likely, energy transfer to the brain is expected to be mediated by a combination of the above modes and those that are yet to be discovered. A recent report by Goeller and associates[9] showed that in a polycarbonate ellipsoid brain model, blast overpressure ranging up to 170 kPa produced cavitation at the contrecoup. Moreover, it has been suggested that the blast-induced effects on the skull may generate microcavitation bubbles that subsequently collapse with high pressure.[9,10] Collapse of highly pressurized bubbles can generate penetrating water jet (e.g, microjet) that is capable of causing tissue injury. Detection of these microbubbles and potential impact on the neural tissues remain virtually unknown, however.

While no blast-induced microbubbles have been directly observed in the brain, cavitation of water has been clearly demonstrated. The pressure associated with collapse of the microbubble can range from 0.1 to 20 MPa,[11] suggesting microcavitation collapse may potentially be responsible for tissue damage. Several head injury models[12–15] also indicate that formation of microcavitation bubbles in response to blunt force to the brain is indeed feasible in experimental and computational studies. Elucidation of potential coupling mechanism at the cell level has been lacking, however. To this end, we have successfully engineered an electrical discharge system that can generate shock waves and microbubbles of different sizes and be mounted on a microscope stage for imaging. This unique and novel system allows us to quantitatively examine subcellular responses using biophysical and molecular techniques. We characterized and now report for the first time changes in the biophysical and biomechanical properties of astrocytes (major glial cell type).

Methods

Cell cultures

Mouse astrocytes were purchased from the American Type Culture Collection (ATCC, Manassas, VA). Cell were maintained in a-modified Eagle medium (a-MEM), 10% fetal bovine serum (FBS; Atlanta Biologicals, Lawrenceville GA), 1% penicillin/streptomycin (Invitrogen, Grand Island, NY). Astrocytes were plated onto glass coverslips and cultured overnight before experiment.

Fluorescence staining

Cell viability was determined using LIVE/DEAD viability kits (Life Technologies) that combine fluorophores to yield two-color discrimination of the live (green) and dead (red) cell population. As a marker for focal adhesion, vinculin was visualized using antibodies. Briefly, cells were seeded on the top or bottom of the chamber, exposed to shock waves and/or microbubbles, fixed with 3.7% formaldehyde, rinsed with phosphate buffered saline. Nonspecific binding sites were blocked using a 5% bovine serum albumin solution for 1 h at room temperature, and then cells were treated with mouse monoclonal antibodies against vinculin at 1:100 dilution. After incubation overnight at 4°C, cells were further incubated with FITC-conjugated goat anti-mouse IgG at room temperature for 1 h. To visualize F-actin, cells were fixed in 3.7% formaldehyde and permeabilized in cold (−20°C) acetone for 3 min, and stained with rhodamine phalloidin (1:100 dilution, Invitrogen) for 30 min at room temperature.

Atomic force microscopy

The cell's elasticity (i.e., Young modulus or sometimes referred to as stiffness) was measured using an atomic force microscope (AFM, Novascan Technologies, Ames, IA) mounted on an inverted Nikon microscope.[16] To minimize the effect of glass substrate on the cell elasticity measurements, we used an indentation depth up to 500 nm (~ 10% of the average cell height) for data analysis. About 100 force-distance curves were generated using >30 cells under each experimental condition. The force-distance curves were collected and analyzed according to Hertz model,[17–19] which relates the loading force (F) with the indentation depth (δ):

$$F = \frac{4}{3}\frac{E}{(1-\upsilon^2)}\delta^{3/2}\sqrt{R}$$

where ν is the Poisson ratio, R is the radius of the spherical indenter ($\sim 5\ \mu$m), E is the local Young elastic modulus. The cellular Poisson ratio was assumed to be 0.5, which treats the cell as an incompressible material. Fitting the Hertz model to the experimental force curve with a standard least squares minimization algorithm yielded the local apparent elastic modulus E.

Membrane permeability and caspase signaling

The FAM-FLICA® kit from Immunochemistry (Bloomington, MN) was used to detect the membrane permeability and activity of the caspase signaling *in vitro*. This kit detects multiple caspases including caspase-1, 2, 3/7, 6, 9, and 10. Propidium iodide (PI) was used to test the membrane permeability. After exposure to shock waves and/or microbubbles, both detached and adherent cells were collected and washed with the given buffer provided in the kit. Cells were stained with the FAM-FLICA caspase inhibitor reagent, PI, and Hoechst 33342. After incubation at 37°C for 30 min, the samples were analyzed using a Synergy HT plate reader (BioTek, Winooski, VT) to measure the FAM-FLICA, PI, and Hoechst 33342 signals. Three independent tests were repeated for each condition.

Superoxide labeling

Mitosox (Life Technologies) was used to label superoxide inside the cells. This novel, membrane permeable fluorophore preferentially targets mitochondria. On oxidation by superoxide, the dye fluoresces (emission maximum 580 nm) and is designed to visualize the production of superoxide using fluorescent microscopy. Astrocytes were exposed to the combination of shock waves and microbubbles and then incubated with 1 mM Mitosox for 30 min at 37°C. Cells were extensively washed and mounted on the microscope stage for imaging.

Exposure chamber

The custom-designed exposure apparatus is shown in Figure 1A. Two needle electrodes were separated by 0.7 mm. The pulsed power system used in the experiment is two, 1 μF capacitors charged by a DC voltage source (4 kV, 800 msec pulses). The capacitors are discharged by four MOSFET switches (IXFB38N100Q2) stacking in series. Because the rated current of each MOSFET is 20A, several resistors (a total resistance of 100Ω) connecting in series with the needle electrodes were used to limit the current. The voltage across the electrodes was measured by a high voltage probe (Tektronix P6015), and the current was measured by a Pearson coil (Pearson Electronics, Palo Alto, CA). Details of the electrical discharge system have been reported elsewhere.[20]

The volume of the chamber is 2.5 mL and was intentionally designed to minimize temperature rise within the chamber to <1°C (Fig. 1B). The principle of symmetry was exploited by placing the

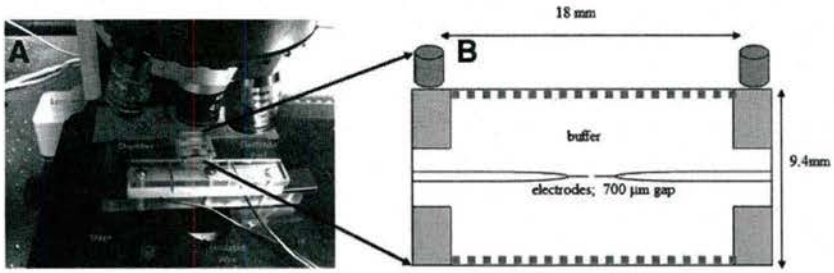

FIG. 1. Schematics of the experimental chamber. (**A**) Photo of the chamber placed on an upright Nikon microscope. (**B**) Side view of the chamber with specific dimensions (not drawn to scale). Experiments were performed using mouse astrocytes (squares) seeded at the top or the bottom of the chamber.

two electrodes the middle of the chamber and plating cells either 4.7 mm above or below the electrodes. The rationale is that the electric field of short duration produced by electrical discharge pulses and shock waves should propagate equally in the two opposing directions to the top and bottom of the chamber where cells are seeded. One important difference is that the microbubbles should rise to the top of the chamber only. While the cells seeded at the top and the bottom do experience electric field (estimated to be negligible, ~0. 28 kV/cm but only for <200 μsec) and shock wave pressure (estimated 10 MPa), the cells seeded at the top only would be exposed to further interaction with the microbubbles. The membrane potential was monitored in real time to ensure that the short duration of electric field exposure did not modify the cellular responses (data available but not shown).

Statistical analysis

Statistical analysis was performed at an alpha level of 0.05. The statistical significance of data was evaluated using analysis of variance. All reported values represent mean ± standard error of the mean.

Results

Characterization of microbubbles

Microbubbles generated by the electrical discharge system were visualized by differential interference contract (DIC) microscopy and analyzed by a custom-designed algorithm. Some microbubbles were visualized as early as 40 msec after the electrical pulses were applied, suggesting these initial bubbles traversed at an average speed of ~100 mm/sec. The maximum number of microbubbles reaching the plane of seeded cells, however, was observed between 1 and 2 sec after the stimulation.

We developed a simple image analysis algorithm to identify, count, and characterize the number and size of the microbubbles at the focal plane (Fig. 2A). A histogram was constructed to display the distribution of the number of microbubbles and their size (Fig. 2B). In triplicate experiments, the density of microbubbles was observed to increase from 10.8/mm^2 (1 pulse) to 18.6/mm^2 (5 pulses). Most of the microbubbles observed were less than 30 μm

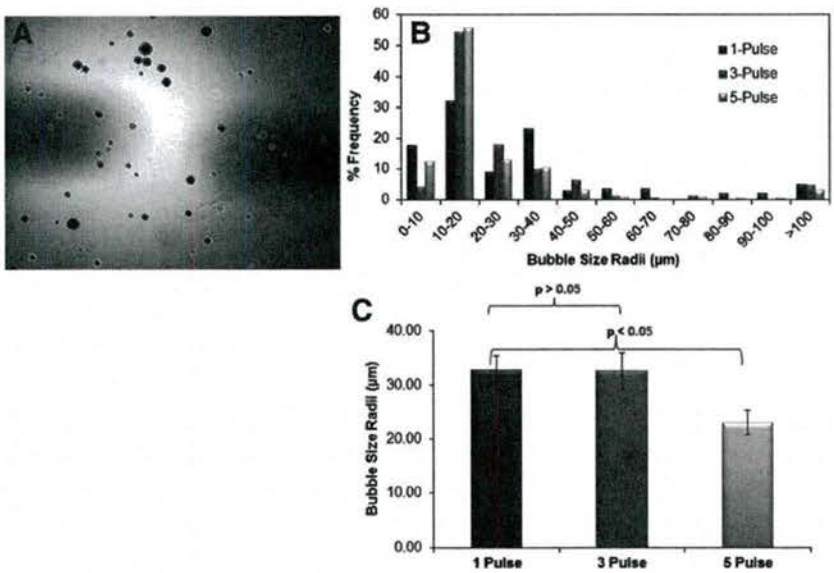

FIG. 2. Characterization of microbubbles. (**A**) Differential interference contrast image of microbubbles captured at the focal plane where cells were seeded. A custom-designed software was developed to identify, count, and analyze the microbubbles. (**B**) A histogram was constructed to demonstrate distribution of microbubble number and size. Between 148 and 254 microbubbles were captured in triplicate and analyzed for the three different experimental conditions. (**C**) Because the microbubble size is not normally distributed, the Tukey method was applied to calculate statistical significance. Data represent mean ± standard error of the mean from three independent experiments.

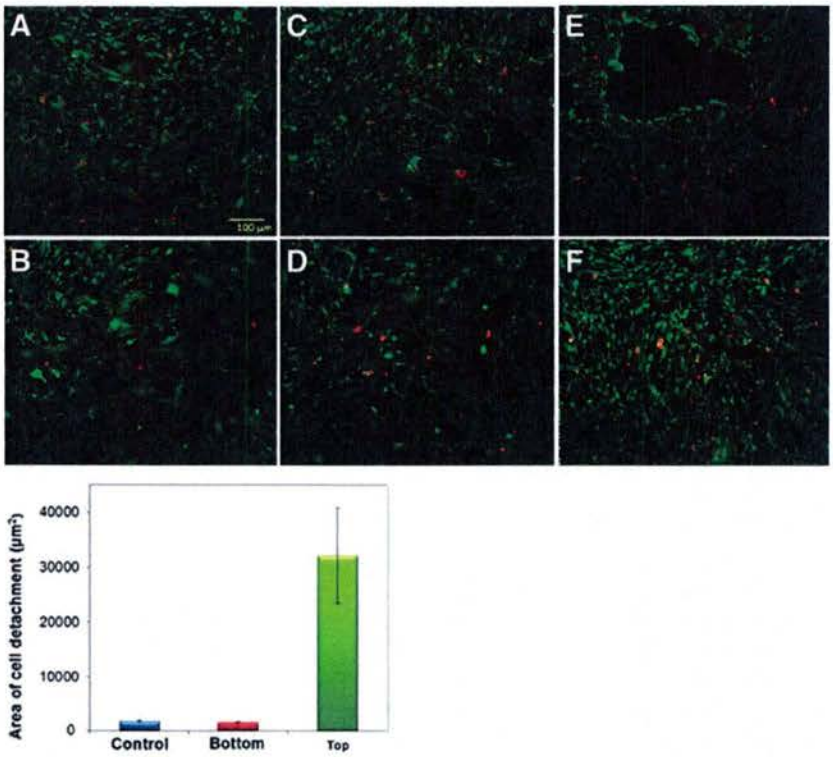

FIG. 3. Cell detachment and viability. Astrocytes seeded at the top (**A, C, E**) or bottom (**B, D, F**) of the chamber were exposed to one (A, B), three (C, D), or five (E, F) shock waves. Cell detachment was noticeably visible under some experimental conditions (e.g., E; five shock waves at the top of the chamber). The area of cell detachment (mean ± standard error of the mean) was measured from three to seven independent experiments. Although there was no indication of cell detachment in the control experiments, the areas of dark regions were nonetheless identified, and the largest dark region was assumed to represent cell detachment. A lower magnification objective (20x, NA/0.5) was used to capture large areas of astrocytes. Color image is available online at www.liebertpub.com/neu

radius. Average radii of the microbubbles depended on the number of the electrical pulses applied (Fig. 2C).

Cell detachment

As expected, astrocytes that were exposed to shock waves and microbubbles became detached from the substrate, and such cell detachment was found to depend on the number of electrical discharge pulses. Cells remaining attached to the substrate were identified and visualized using a fluorescent cell viability assay that fluoresces live cells in green and dead cells in red. The cells exposed to one single pulse did not show any noticeable detachment from the substrate whether cells were plated at the top or bottom of the chamber, and the cell viability remained unchanged (Fig. 3A, 3B). In contrast, a sequence of three or five pulses exhibited an increasing extent of cell detachment and in the number of dead cells (Fig. 3C–3F).

It is evident that the cell detachment and the decrease in cell viability appeared to be correlated. This is perhaps best exemplified when astrocytes were exposed to five pulses (Fig. 3E, 3F). A large area of cell detachment was noticeably visible at the top of the chamber (Fig. 3E), and the number of dead cells also increased. At the bottom of the chamber where microbubbles were prevented to reach, more dead cells were found (Fig. 3F). One significant difference, however, is that cells at the bottom of the chamber essentially maintained adherence to the substrate, and no apparent cell detachment was observed. The area of cell detachment was analyzed using ImageJ and determined $\sim 32{,}000\ \mu m^2$. In control experiments, the same image analysis showed virtually no area of cell detachment.

Cell adhesion and biomechanics

Cell detachment and viability are strongly dependent on cell adhesion to the substrate. To examine altered cell adhesion in response to shock wave and microbubble, focal adhesions were visualized by fluorescently labeling vinculin, and F-actin was identified using phalloidin. Typical focal adhesions are known to form punctates that were clearly observed in control cells (Fig. 4A). After five pulse stimulation, cells seeded at the bottom of the chamber (i.e, no microbubbles) still maintained similar organization of focal adhesion (Fig. 4B). In contrast, cells seeded at the top

FIG. 4. Altered focal adhesion. Fluorescent images of vinculin in astrocytes seeded at the top but without any stimulation (control; **A**) or at the bottom (**B**) or at the top (**C**) of the chamber and exposed five pulse simulation. Image analysis showed that the vinculin expression in cells in the panel (C) was reduced by 64.1 ± 8.5%. Data represent mean ± standard error of the mean of three independent experiments.

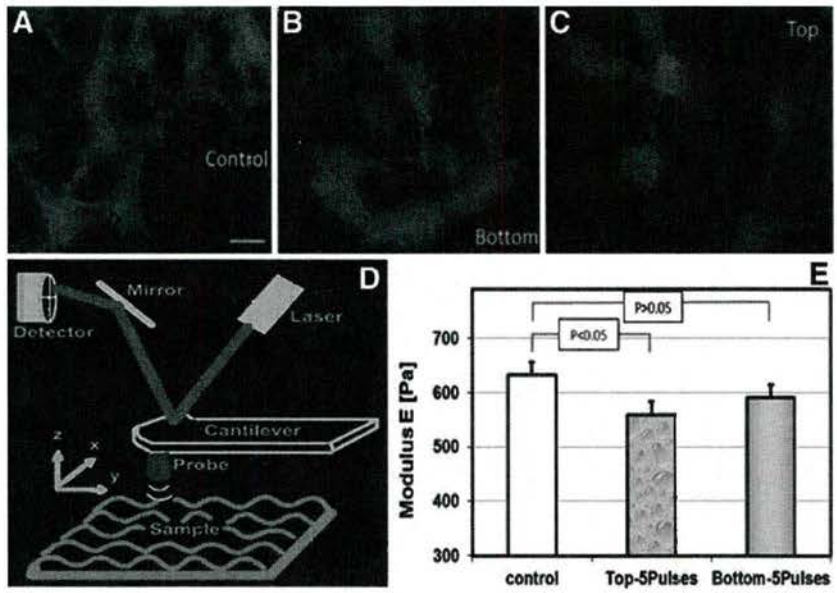

FIG. 5. F-actin organization and elastic modulus of astroctyes. F-actin was fluorescently labeled in the control cells (**A**), in the cells seeded at the bottom (**B**) or top (**C**) of the chamber (bar = 20 mm). A schematic illustrates the principle of atomic force microscope (AFM)-based microindentation (**D**). Microindentation up to 500 nm depth is induced by an AFM tip and the cantilever deflection is measured by laser interference pattern. Young modulus of astrocyte seeded at the bottom of the chamber showed no statically significant changes, while the cells seeded at the top of the chamber became mechanically compromised (D).

of the chamber demonstrated no distinctive punctuates, but vinculin appeared to have been down-regulated and redistributed (Fig. 4C). Quantitative analysis indicates that the vinculin expression in the cells seeded at the top decreased by 65%. This finding suggests that microbubbles caused astrocytes to reorganize focal adhesions and therefore diminished cell attachment to the substrate.

To visualize the microfilament organization, F-actin was fluorescently labeled (Fig. 5A–5C). While astrocytes and other brain cells are not expected to demonstrate thick microfilament stress fibers, the F-actin organization in either control cells or cells seeded at the bottom of the chamber exhibited F-actin stress fibers, whereas in the cells seeded at the top of the chamber, the stress fibers appear to have been diminished. Loosely organized microfilament structure is consistent with mechanically softened cells. The cell's mechanical property was therefore measured using AFM. The cells were microindented $\sim 0.5\ \mu m$ by an AFM tip,[16–19] and Young moduli were determined (Fig. 5). In control cells, the elastic modulus was about 0.62 kPa, approximately five-fold softer than, for example, human mesenchymal stem cells (3.2 kPa[16]) but similar to other brain cell types (~ 0.5 kPa[21]).

Exposure of cells to the shock wave only (e.g., at the bottom of the chamber) did not significantly alter the biomechanical properties, whereas the microbubbles impacting the cells seeded at the top of the chamber caused astrocytes to become mechanically softer ($p < 0.05$), suggesting the cellular biomechanical integrity may have been compromised.

PI uptake and activation of caspase signaling

Changes in the cellular biomechanics may be an indication that the cell membrane permeability could have been modified and activation of the apoptotic signaling pathways initiated. To test this hypothesis, we measured and quantified the number of cells that were permeable to PI. Because PI is membrane impermeant and excluded by viable cells, uptake of PI is indicative of structural alteration in the cell membrane. As shown in Figure 6A, only the cells seeded at the top but not at the bottom of the chamber demonstrated an increase in the PI uptake in response to microbubbles. This finding is consistent with an assay that identifies activation of the caspase signaling pathways (Fig. 6B), a marker for cellular damage leading to apoptosis. It is interesting to note that cellular interaction with a lesser number of and larger size microbubbles (e.g., one pulse stimulation) does not appear to induce significant changes either in the PI uptake or activation of the caspase signaling.

Production of superoxide

Apoptotic signaling can be induced by oxidative stress. To measure the expression of superoxide in astrocytes using fluorescent microscopy, cells were plated at the top of the chamber and exposed to a five-pulse stimulation, and immediately incubated with Mitosox (1 mM). Punctates of superoxide clusters around the

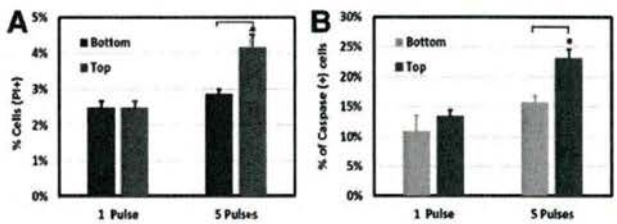

FIG. 6. Membrane permeability and apoptosis. (**A**) Uptake of propidum iodide (PI) and (**B**) activation of the caspase signaling pathways were quantitatively determined. Data represent mean ± standard error of the mean from three independent experiments. *Indicates $p < 0.05$.

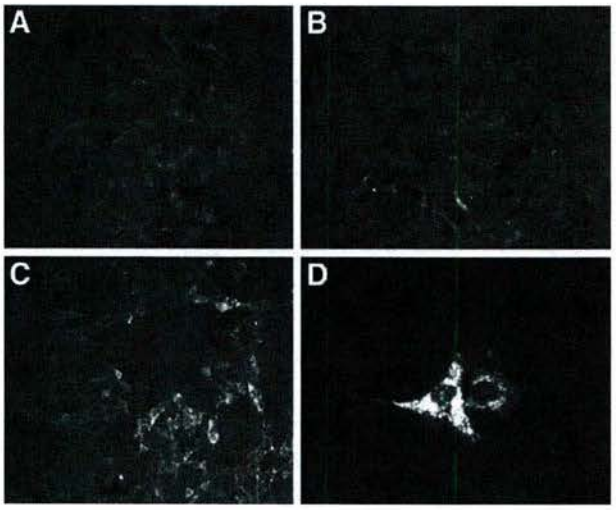

FIG. 7. Production of intracellular superoxide. Mitosox (1 mM) was used to visualize intracellular superoxide in control cells (**A**) and in cells seeded at the bottom (**B**) or top (**C**) of the chamber using a 20x, NA/0.5 objective. A higher magnification objective (60x, NA/1.4) was used to provide evidence for apparent accumulation of the Mitosox dye in the nuclei of astrocytes that were exposed to microbubbles (**D**).

nucleus were observed in control cells (Fig. 7A). Similarly, the Mitosox expression in astrocytes plated at the bottom of the chamber showed no discernable differences when compared with the control cells (Fig. 7B). In contrast, the cells exposed to microbubbles not only exhibited a higher level of superoxide but also showed that perhaps Mitosox dye penetrated into the nucleus (Fig. 7C). For better illustration, a higher magnification objective was used to enlarge astrocytes in which evidence of the dye accumulation inside the nucleus was demonstrated (Fig. 7D). Because the dye is highly fluorescent on binding to nucleic acid, it is perhaps indicative of compromised nuclear envelope that can alter the nuclear trafficking of macromolecules.

Discussion

A potential cause of brain injury has been hypothesized and attributed to cerebrospinal fluid (CSF) cavitation.[13,22] While the CSF can act as a buffer to provide protection for the brain, the brain and/or meninges separate from the skull on force impact, and regional negative pressures overcome the tensile strength of brain tissue. This can create vacuum cavity (i.e., microcavitation bubbles), and collapse of such cavities adversely affects the neural tissues.[23] It is still controversial, however, whether CSF cavitation occurs during explosive blast. Other postulates and speculations have also been proposed, including blast-caused sudden acceleration of the head movement that decreases cerebral intravascular and intracranial pressure sufficiently to produce microcavitation bubbles that collapse and may generate secondary shock waves.[10] While no blast-induced microbubbles have been directly observed in the brain, cavitation in water[11] or in a surrogate human model[9] has been clearly demonstrated.

The goal of the current study was therefore to elucidate the role of microcavitation at the cell level using *in vitro* astrocyte culture models.

Because the microbubble generation system used in this study does produce large but short-lived electric fields and shock waves, we modified the exposure chamber (Fig. 1B) to rule out bioeffects caused by something other than microbubbles. First, the energy input needed to produce shock waves may have raised the temperature inside the chamber. Simple calculations suggest that the worst scenario (800 μsec pulse) in which no heat diffusion is allowed would raise the chamber temperature <1°C. After a five-pulse stimulation, the temperature of the buffer in the chamber was measured within 3 sec and found to be no different than ambient temperature.

Further, we transfected astrocytes with green fluorescence proteins (GFPs). Because GFPs are sensitive to temperature, they have been used to calibrate the intracellular temperature.[24,25] We observed no changes in the GFP signals in response to any stimulations we applied (data available but not shown), indicating temperature rise in the chamber and inside the cells is negligible.

Second, the results shown in this article were obtained using astrocytes that were seeded 4.7 mm vertically away from the electrodes. Numerical simulation results indicate that at this vertical distance, the electric field strength was estimated as not insignificant but only lasts <200 μsec. To experimentally rule out a potential effect from the electric field, we applied a fast reacting membrane potential dye (Di-4-ANEPPS)[26] and monitored its fluorescent intensity. If there were a high electric field present for a considerable period, the cell membrane should be depolarized and the fluorescent intensity would be expected to decrease. We observed no such changes in the membrane potential (data not shown), suggesting that the effects associated with a short-lived electric field can be ignored.

Third, the shock wave pressure where the cells were seeded was estimated at 10 MPa.[20] If the shock waves were sufficient to cause cell detachment, such an effect should have been observed both at the top and the bottom of the chamber. The reason is that we intentionally designed the exposure chamber to exploit the principle of symmetry. Shock waves produced at the middle of the chamber should propagate equally to the top as well as to the bottom of the chamber. However, cells exposed up to five shock waves only do not show evidence of cell detachment, altered focal adhesion, changes in the biomechanical properties, PI uptake, or activation of the caspase signaling pathways (Fig. 3F, 4B, 5B, and 6, respectively). A logical conclusion may be drawn that transient shock wave pressure on the order of $\sim$10 MPa does not modulate the astrocytes' behavior or response.

One advantage of the chamber modification is to force microbubbles to rise to the top only and therefore delineate the bioeffects that can be attributed to the microbubbles. While it is experimentally difficult to determine the lifetime of microbubbles, movements of a few microbubbles were captured using high frame rates of video imaging. Image analysis suggests that the microbubbles can move as rapidly as 100 mm/sec. At this velocity, the unimpeded microbubble movement would require at least 0.05 sec to rise to the top of the chamber ($\sim$5 mm). Because we observed the maximum bubble density between 1 to 2 sec after stimulation, we can approximate the lifetime of the microbubbles between fractions of a second to <2 sec.

Such an estimate is actually consistent with the theory developed by Ferrari and coworkers.[27] The effects observed at the top of the chamber are significantly different. Unlike the cells seeded at the bottom of the chamber, the cellular and subcellular effects observed in astrocytes seeded at the top include noticeable cell detachment from the substrate, changes in focal adhesion and biomechanics, and an increase in the PI uptake and activation of the caspase signaling.

Three possible explanations may be offered. First, we noted that the density of microbubbles increased by 70% with the number of pulses applied to generate them (Fig. 2B), and more adverse bioeffects were observed with more microbubbles. It suggests that astrocytes exposed to more microbubbles are prone to adverse cellular damage. Second, an alternative explanation may be due to the smaller size of microbubble in response to using multiple pulses (Fig. 2C). It is interesting to note here that the collapse of microbubbles near cells is expected to produce secondary and localized shock waves.[28–30] The interior pressure of microbubbles increases with smaller radii and has been calculated using the Young-Laplace equation,[31,32] ($\Delta P = 2\,s/r$) where s is the surface tension and r is the radius. For example, the pressure of 1 μm microbubbles in water can be at least an order of magnitude greater that the pressure in 10 μm microbubbles.

Third, the collapse time of microbubbles also depends on the size. As demonstrated by Takahashi and colleagues,[30] 40 μm microbubbles are predicted to collapse within a few seconds, whereas 10 μm microbubbles could have a collapse time >100 sec, providing a longer lifetime during which the smaller microbubbles may affect the cells. Collectively, it is feasible to postulate that the combination of a greater microbubble density and smaller microbubble size with a longer collapse time and higher interior pressure is responsible for the adverse changes in astrocytes documented in this article.

Finally, we postulate here an alternate mechanism that collapse of microbubbles produces hydroxyl radicals.[33,34] The temperature inside the collapsing microbubble may be significantly elevated for a short time, causing pyrolytic decomposition and producing reactive oxygen species such as hydroxyl radicals.[35] This potential thermochemical reaction near the cells may generate oxidative stress and adversely affect the cellular integrity and function. If validated, the implication would be, in addition to the physical assault induced by microbubbles, collapse of microbubbles may alter the local chemical microenvironment that further exacerbates adverse subcellular effects, including altered nuclear transport.[36]

Estimating the potential shear stress associated with the collapse of microbubbles remains a daunting challenge. If a microjet is produced by collapsing microbubbles, the magnitude of induced shear stress can be estimated by $\tau = \mu(v_j/h)$ where μ is dynamic viscosity of the medium (water: 0.89×10^{-4} Pa·s) and v_j is the jet speed, and h is the typical cross-section dimension of the jet.[37]

In our experiments, most bubbles were measured in the range of 20–30 μm, comparable to the cell size. The velocity of the microjets in our experiment is not available; however, for similar bubble sizes, it was measured to be $\sim$10 m/sec.[38] If the jet diameter is taken 1/10 of the bubble size, one can estimate the shear stress is 350 Pa. As a point of comparison, the critical shear stress for cell detachment was reported to be 0.1 kPa[39] and 1–3 kPa for membrane rupture.[27] Further, the recent estimate of collapse of bubbles is predicted to be as high as 20 MPa.[9] These estimates remain to be experimentally validated.

Several experiments are under way to fabricate microposts of known mechanical properties. It is anticipated that, on collapse of microbubbles, a shear stress will be generated that can bend the microposts. Deflection of the fluorescent bead-containing microposts can be monitored, and therefore the shear stress can be directly measured.

The unique and novel exposure system we developed and characterized for the current study allows us to quantitatively examine biological responses. Using cell cultures of astrocytes (major glial cell type), we have observed and quantified several important cellular responses that are critical for maintaining the cell viability and functionality. Astrocytes occupy between 20% and 50% of brain volume and exceed the number of neurons by $\sim$10-fold.[40,41] These glial cells are also known to regulate the clearance of neurotransmitters and thereby prevent excitotoxicity.[42] Results from our experiments using such an important brain cell type might lead to a better understanding of the effect of blast-induced microbubbles.

Additional studies are under way to engineer physiologically relevant three-dimensional (3D) collagen hydrogels of co-culture models using neurons and astrocytes. A recently developed co-culture model has been applied to study the common motor neuron diseases such as amyotrophic lateral sclerosis.[43] Our research approaches that use state-of-the-art molecular and biomechanical techniques will be applied to test and validate/refute the hypothesis that potential bioeffects in the 3D microenvironment arise also from localized membrane damage, cytoskeleton collapse, necrotic cell death, and activation of apoptosis. Unlike other previous studies using animal models, our shockwave and microcavitation generating system is capable of repetitive exposure to the neural cells and tissues. A spatially and temporally integrated model may be formulated in which complex series of molecular interactions in response to blast-induced TBI may be better explained by the presence of microbubbles.

Acknowledgement

This work was supported by a grant (N00014-13-1-0404) from the Office of Naval Research.

Author Disclosure Statement

No competing financial interests exist.

References

1. Gonzalez, P.G., and Walker, M.T. (2011). Imaging modalities in mild traumatic brain injury and sports concussion. PM R 3, Suppl 2, S413–S424.
2. Kan, E.M., Ling, E.A., and Lu, J. (2012). Microenvironment changes in mild traumatic brain injury. Brain Res. Bull. 87, 359–372.
3. Menon, D.K., Schwab, K., Wright, D.W., and Maas, AI (2010). Position statement: Definition of traumatic brain injury. Arch. Phys. Med. Rehabil. 91, 1637–1640.
4. Pedersen, T. Mild brain injury in combat may lead to PTSD. Available at: http://psychcentral.com/news/2012/06/08/mild-brain-injury-in-combat-may-lead-to ptsd/39891.html. Accessed: May 13, 2015.
5. Lollis, S.S., Quebada, P.B., and Friedman, J.A. (2008). Traumatic brain injury, in: *Handbook of Clinical Neurology*. M. Aminoff, F. Boller, and D. Swaab, (eds). Elsevier: Edinburgh, pps. 217–229.
6. Benzinger, T.L., Brody, D., Cardin, S., Curley, K.C., Mintun, M.A., Mun, S.K., Wong, K.H., and Wrathall, J.R. (2009). Blast-related brain injury: Imaging for clinical and research applications: Report of the 2008 St. Louis Workshop. J. Neurotrauma. 26, 2127–2144.
7. Armonda, R.A., Bell, R.S., Vo, A.H., Ling, G., DeGraba, T.J., Crandall, B., Ecklund, J., and Campbell, W.W. (2006). Wartime traumatic cerebral vasospasm: Recent review of combat casualties. Neurosurgery 59, 1215–1225.
8. Cernak, I., Merkle, A.C., Koliatsos, V.E., Bilik, J.M., Loung, Q.T., Mahota, T.M., Xu, L., Slack, N., Windle, D., and Ahmed, F.A. (2011). The pathobiology of blast injuries and blast-induced neurotrauma as identified using a new experimental model of injury in mice. Neurobiol. Dis. 41, 538–551.
9. Goeller, J., Wardlaw, A., Treichler, D., O'Bruba, J., and Weiss, G. (2012). Investigation of cavitation as a possible damage mechanism in blast-induced traumatic brain injury. J. Neurotrauma. 29, 1970–1981.
10. Stuhmiller, J.H. (2002). A health hazard assessment for blast overpressure exposure. Annual Report DAMD17-96-C-6607. (www.dtic.mil/cgi-bin/GetTRDoc?AD=ADA413062)

11. Herbert, E., Balibar, S., and Caupin, F. (2006). Cavitation pressure in water. Phys. Rev. E. Stat Nonlin Soft Matter Phys 74, 041603.
12. El Sayed, T., Mota, A., Fraternali, F., and Ortiz, M. (2008). Biomechanics of traumatic brain injury. Comput. Methods Appl. Mech. Eng. 197, 4692–4701.
13. Lubock, P., and Goldsmith, W. (1980). Experimental cavitation studies in a model head-neck system. J. Biomech. 13, 1041–1052.
14. Panzer, M.B., Myers, B.S., Capehart, B.P., and Bass, C.R. (2012). Development of a finite element model for blast brain injury and the effects of CSF cavitation. Ann. Biomed. Eng. 40, 1530–1544.
15. Nakagawa, A., Manley, G.T., Gean, A.D., Ohtani, K., Armonda, R., Tsukamoto, A., Yamamoto, H., Takayama, K., and Tominaga, T. (2011). Mechanisms of primary blast-induced traumatic brain injury: Insights from shock-wave research. J. Neurotrauma. 28, 1101–1119.
16. Titushkin, I., and Cho, M. (2007). Modulation of cellular mechanics during osteogenic differentiation of human mesenchymal stem cells. Biophys. J. 93, 3693–3702.
17. Titushkin, I., and Cho, M. (2011). Altered osteogenic commitment of human mesenchymal stem cells by ERM protein-dependent modulation of cellular biomechanics. J. Biomech. 44, 2692–2698.
18. Sun, S., Wong, S.W., Mak, A.F., and Cho, M. (2014). Impact of oxidative stress on cellular biomechanics and rho signaling in C2C12 myoblasts. J. Biomech. 47, 3650–3656.
19. Sun, S., Song, Z.Y., Cotler, S.J., and Cho, M. (2014). Biomechanics and functionality of hepatocytes in liver cirrhosis. J. Biomech. 47, 2205–2210.
20. Kang, D., Nah, J., Cho, M., and Xiao, S. (2014). Shock wave generation in water for biological studies. IEEE Tran. Plas. Sci. 42, 3231–3228.
21. Leventhal, I., Georgesa, P.C., and Janmey, P.A. (2006). Soft biological materials and their impact on cell function. Soft Matter.
22. Nusholtz, G.S., Wylie, E.B., and Glascoe, L.G. (1995). Internal cavitation in simple head impact model. J. Neurotrauma. 12, 707–714.
23. Hardy, W.N., Khalil, T.B., and King, A.I. (1994). Literature review of head injury biomechanics. Int. J. Impact Eng. 15, 561–586.
24. Donner, J.S., Thompson, S.A., Kreuzer, M.P., Baffou, G., and Guidant, R. (2012). Mapping intracellular temperature using green fluorescent proteins. Nano Lett. 12, 2107–2111.
25. Kiyonaka, S., Kajimoto, T., Sakaguchi, R., Shinmi, D., Omatsu-Kanbe, M., Matsuura, H., Imamura, H., Yoshizaki, T., Hamamchi, I., Morri, T., and Mori, Y. (2013). Genetically encoded fluorescent thermosensors visualize subcellular thermoregulation in living cells. Nat. Methods 10, 2132–1238.
26. Bachtel, A.D., Gray, R.A., Stohlman, J.M., Bourgeois, E.B., Pollard, A.E., and Rogers, J.M. (2011). A novel approach to dual excitation ratiometric optical mapping of cardiac action potentials with di-4-ANEPPS using pulsed LED excitation. IEEE Tran. Biomed. Eng. 58, 2120—2126.
27. Ferrari, M., Liggieri, L., and Miller, R. (eds). (2012). *Drops and Bubbles in Contact with Solid Surfaces.* CRC Press: Boca Raton, FL.
28. Takahashi, M., Kawamura, T., Yamamoto, Y., Ohnari, H., Himuro, S., and Shakutsui, H. (2003). Effect of shrinking microbubbles on gas hydrate formation. J. Phys. Chem. B. 107, 2171–2173.
29. Takahashi, M. (2005). Zeta potential of microbubbles in aqueous solutions: electrical properties of the gas-water interface. J. Phys. Chem. B. 109, 21858–21864.
30. Takahashi, M., Chiba, K., and Li, P. (2007). Free-radical generation from collapsing microbubbles in the absence of a dynamic stimulus. J. Phys. Chem. B. 111, 1343–1347.
31. Vakarelski, I.U., Manica, R., Tang, X., O'Shea, S.J., Stevens, G.W., Grieser, F., Dagastine, R.R., and Chan, D.Y. (2010). Dynamic interactions between microbubbles in water. Proc. Nat. Acad. Sci. U S A. 107, 11177–11182.
32. Israelachvili, J.N. (1991). *Intermolecular and Surface Forces.* Academic Press: San Diego, CA, pps. 176–259.
33. Takahashi, M., Chiba, K., and Li, P. (2007). Formulation of hydroxyl radicals by collapsing ozone microbubbles under strongly acidic conditions. J. Phys. Chem. B. 111, 11443–11446.
34. Agarwal, A., Ng, W.J., and Liu, Y. (2011). Principle and applications of microbubble and nanobubble technology for water treatment. Chemosphere. 84, 1175–1180.
35. Kimura, T., and Ando, T. (2002). Physical control of chemical reaction by ultrasonic waves. Ultrason. Technol. 14, 7–8.
36. Kodiha, M., and Stochaj, U. (2012). Nuclear transport: A switch for the oxidative stress—signaling circuit? J. Signal Transduc. Available at: http://dx.doi.org/10.1155/2012/208650. Accessed: May 13, 2015.
37. Sankin, G.N., Yuan, F., and Zhang, P. (2010). Pulsating tandem microbubble for localized and directional single-cell membrane poration. Phys. Rev. Lett. 105, 078101.
38. Yuan, F. (2013). Probing the bioeffects of cavitation at the single-cell level. Ph.D. Thesis. Duke University.
39. Ohl, C.D., and Wolfrum, B. (2003). Detachment and sonoporation of adherent HeLa-cells by shock wave-induced cavitation. Biochim. Biophys. Acta. 1624, 131–138.
40. O'Kusky, J., and Colonnier, M. (1982). A laminar analysis of the number of neurons, glia, and synapses in the visual cortex (area 17) of the adult macaque monkeys. J. Comp. Neurol. 210, 278–290.
41. Kimelberg, H.K., and Norenberg, M.D. (1989). Astrocytes. Sci. Am. 260, 66–76.
42. Schousboe, A., and Waagepetersen, H.S. (2005). Role of astrocytes in glutamate homeostasis: implications for excitotoxicity. Neurotox. Res. 8, 221–225.
43. Kunze, A., Lengacher, S., Dirren, E., Aebischer, P., Magistretti, P.J., and Renaud, P. (2013). Astrocyte-neuron co-culture on microchips based on the model of SOD mutation to mimic ALS. Integr. Biol. 5, 964–975.

Address correspondence to:
Michael Cho, PhD
Department of Bioengineering
University of Illinois at Chicago
851 S. Morgan Street, MC 063
Chicago, IL 60607

E-mail: mcho@uic.edu

REVIEW OF SCIENTIFIC INSTRUMENTS **86**, 124901 (2015)

Microbubble generation by piezotransducer for biological studies

W. Zhu,[1,a)] M. Alkhazal,[2,3] M. Cho,[4] and S. Xiao[2,3,b)]
[1]*Department of Applied Science and Technology, Saint Peter's University, Jersey City, New Jersey 07306, USA*
[2]*Frank Reidy Research Center for Bioelectrics, Old Dominion University, Norfolk, Virginia 23529, USA*
[3]*Department of Electrical and Computer Engineering, Old Dominion University, Norfolk, Virginia 23529, USA*
[4]*Department of Biomedical Engineering, University of Illinois, Chicago, Illinois 60607, USA*

(Received 29 July 2015; accepted 11 November 2015; published online 2 December 2015)

Bubbles induced by blast waves or shocks are speculated to be the major cause of damages in biological cells in mild traumatic brain injuries. Microbubble collapse was found to induce noticeable cell detachment from the cell substrate, changes in focal adhesion and biomechanics. To better understand the bubble mechanism, we would like to construct a system, which allows us to clearly differentiate the impact of bubbles from that of shocks. Such a generator needs to be low profile in order to place under a microscope. A piezoelectric transducer system was designed to meet the need. The system uses either a flat or a spherical focusing piezoelectric transducer to produce microbubbles in a cuvette loaded with cell-culture medium. The transducer is placed on the side of the cuvette with its axis lining horizontally. A cover slip is placed on the top of the cuvette. The impact of the waves to the cells is minimized as the cover slip is parallel to the direction of the wave. Only bubbles from the medium reach the cover slip and interact with cells. The effect of bubbles therefore can be separated that of pressure waves. The bubbles collected on a cover slip range in size from 100 μm to 10 μm in radius, but the dominant size is 20-30 μm. © *2015 AIP Publishing LLC.* [http://dx.doi.org/10.1063/1.4936555]

I. INTRODUCTION

Soldiers who experience the repeated impact of blast waves may develop mild traumatic brain injuries (TBIs), for example, in the form of a concussion.[1] While the cause of TBI is still not well understood, a leading theory is that microbubbles are generated due to the pressure impacts, which subsequently collapse, causing microstreams.[2] The force created by the microstreams could reach a level sufficient to disrupt cell-cell connections and even create membrane pores.[3,4] This theory has been proved in astrocytes,[5] which provides insights for 3-D tissue culture or animal studies. In a tissue subjected to pulsed high-intensity focused ultrasound (pHIFU), acoustic cavitation threshold varies broadly and depends on the tissue composition.[6] Experimental shock and blast systems that can be repeatedly applied include electrically driven spark gaps, focused laser, shock tubes, and piezotransducers. Each approach has merits and disadvantages. For example, a laser focused in water can create a single shock and bubble precisely on the micrometer scale, therefore becoming highly useful for studying biological responses of a single cell. In the scenario of multiple bubbles, however, several lasers are needed and therefore increase the complexity of the system.[3] Shock tubes can easily reproduce the blast waves that mimic the actual blast waves in a bombshell detonation, but due to the large scale, their use on an *in vitro* microscope study becomes impossible. Spark gaps are easy to construct, especially in water to produce bubbles. In the system reported in our previous work,[5,7] the impact of bubbles on astrocytes was clearly demonstrated and shock alone was shown to be ineffective to induce cell damage. However, one caveat for that system is the presence of an electric field before the breakdown of the spark gap, which can be a source of artifacts and may contaminate the biological results. Although we have not observed the effect directly caused by the electric fields in astrocytes, some other sensitive cell lines may be more susceptible to activation by the electric fields in addition to the bubble effect, making the interpretation of results difficult. It would be necessary to have a cleaner system in which the bubbles are the only stimuli to the cells. In this paper, we report such a system with the use of piezotransducers immersed in water to produce microbubbles. The piezotransducers are driven by RF signals with ultra-low voltages (peak voltage ~40 V) and the electric fields are no longer a concern. In the liquid environment, the negative pressure in the tensile phase allows bubble creation and growth. Because the transducer is placed on the side of the cuvette and the cover slip on the top of the cuvette, the pressure wave's impact with the cells is minimized. All that interacts with the cells are the bubbles rising to the cover slip on which biological cells are seeded. The biological response to the bubbles can therefore be observed provided that the microscope is focused on the cover slip.

II. MICROBUBBLE GENERATOR

A. The electrical circuit

We adopted a commonly used ultrasonic water atomizer circuit to drive the piezotransducer at a resonance frequency

a)This research was performed while W. Zhu was visiting the Frank Reidy Research Center for Bioelectrics, Old Dominion University, Norfolk, Virginia 23508, USA.
b)Author to whom correspondence should be addressed. Electronic mail: sxiao@odu.edu.

 ©2015 AIP Publishing LLC
This article is copyrighted as indicated in the article. Reuse of AIP content is subject to the terms at: http://scitationnew.aip.org/termsconditions. Downloaded to IP: 128.82.40.63 On: Mon, 07 Dec 2015 14:59:20

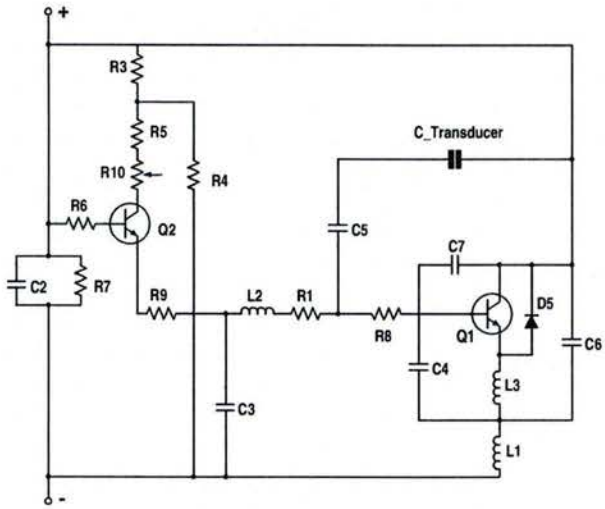

FIG. 1. A schematic diagram of the electrical circuit of the microbubble generator. A tank circuit (L1, L3, and C3) determines the oscillation frequency. A power BJT Q1 allows the replenishment of the energy stored in the inductors (L1 and L3) and sustains the oscillation.

of ~2.1 MHz. A schematic diagram of the driving circuit is shown in Fig. 1. The critical component is a power BJT Q1. Two inductors in series (L1 and L3) and a capacitor (C3) in parallel constitute the tank circuit, which determines the frequency of the oscillation. When Q1 turns on as a result of the switching-on of Q2 and charging of C3, L3 and L1 become charged. The voltage at L1 feeds back through C4 to the base of Q1, calling for more current for a fast charging of L1. The oscillation rises from the discharging and charging between C3 and L1, which in turn switches Q1 on and off. In short, L1, L3, and C3 form the oscillation and C5 and C6 provide an AC short path to the transducer. Meanwhile, the energy is replenished by the turning-on of Q1.

The standard household voltage (120 Vrms) is stepped down to ~28 Vrms to serve as the power source of the circuit. We note that higher voltages, for example, 100 Vrms, can cause visible electrolysis and are therefore not suitable for generating vibrations. A relay (Tyco CNS-35-72) is connected to the primary side of the transformer to control the "on-time" of the circuit, thereby controlling the on-time of the mechanical vibration of the piezotransducer. The on-time in this study was limited to ~2 s.

B. Microbubble chamber design

The size of the microbubbles is typically between single-digit micrometers to hundreds of micrometers. When they are resting on a glass surface, a conventional upright microscope is sufficient to observe these bubbles. However, in order to incorporate the chamber under a microscope for biological studies, a few criteria have to be met: (1) there has to be a light pathway so that the cover slip can be illuminated; (2) the overall chamber size (in particular its height) should be small enough so that it can be placed on the microscope stage; (3) there should be a fairly easy way to place and remove the cover slips; and (4) microbubbles can reach the cover slip with minimal impact from the mechanical vibration generated by the piezotransducer.

Acrylic sheet was initially considered as the material for the chamber since they are easy to machine. However, considerable heat damage to the acrylic sheet on the air side at the line-of-sight of the piezotransducer was observed after repeated operation. This is due to a mismatch between the acoustic impedance of acrylic and the air interface: The acoustic impedance of acrylic is 3.26×10^{-6} kg s^{-1} m^{-2} [8] while that of air is 400 kg s^{-1} m^{-2}. Therefore, the transition of the low impedance to high impedance causes an increased magnitude of the mechanical wave at the interface and excessive heat, leading to the damage of the acrylic sheet (melting point: ~160 °C).

We therefore chose glass (melting temperature 1400 °C) as the material to construct the main body of the chamber. The piezotransducer was arranged at 90° to the cover slip to avoid the direct transfer of vibration to the cover slip. A separate compartment for the piezotransducer was constructed with a circular opening (Φ = 1.50 cm) to the primary chamber. Edge steps were constructed along the top of the chamber walls to support a transparent top cover, where a stepped hole was drilled for the placement of the cover slip. A thin trench of ~2 mm in width connecting to the stepped hole was made for easy mounting and dismounting of the cover slips with tweezers. The pre-seeded cells on the cover slip face the water bulk in the water so the risen bubbles interact with them as soon as they make contact. Fig. 2(a) shows a schematic diagram of the chamber design with primary dimensions annotated. Fig. 2(b) shows a picture of the chamber placed on the stage of an upright microscope.

An added benefit of an all-glass chamber is that one can observe and photograph the generation of microbubbles from the side of the chamber while illuminating the chamber with a strong light source. During our experiments, tap water was used to fill the chamber up to the cover slip. No specific degassing procedure was carried out. It should also be noted that bubbles generated in previous cycles sometimes attached to the surface of the piezotransducer. Ultrasound energy in the following cycle is absorbed by these bubbles, preventing further microbubble formation in water. One can either extend the duration of the operation, i.e., use the ultrasonic vibration of the piezotranducer to "shake off" the attached bubbles, or to clean the surface of the piezotransducer before each cycle.

C. Piezotransducers

Two kinds of piezotransducer (STEMiNC) were used in this study. The spherical transducer has a diameter of 20 mm and a focal point at 30 mm from the transducer surface. It is operated at the resonant frequency of 2.1 MHz. The idea was to generate bubbles preferably at the focal plane of the transducer so that the maximum amount of bubbles rises to the cover slip. The flat transducer has a diameter of 19 mm and a thickness of 1 mm, which has a resonant frequency of 2.07 ± 0.05 MHz. Both transducers were made with similar materials and operate in the thickness vibration mode with the electro-mechanical coupling coefficient, $k_p \approx 0.59$.

This article is copyrighted as indicated in the article. Reuse of AIP content is subject to the terms at: http://scitationnew.aip.org/termsconditions. Downloaded to IP: 128.82.40.63 On: Mon, 07 Dec 2015 14:59:20

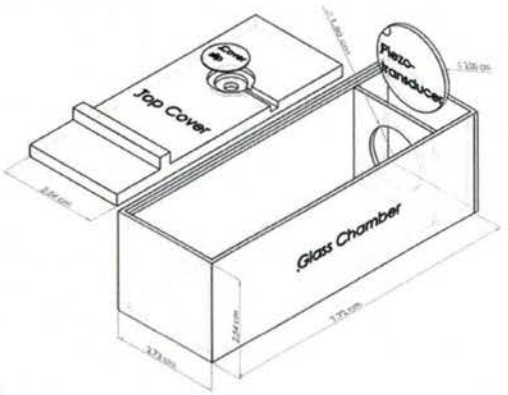

(a)

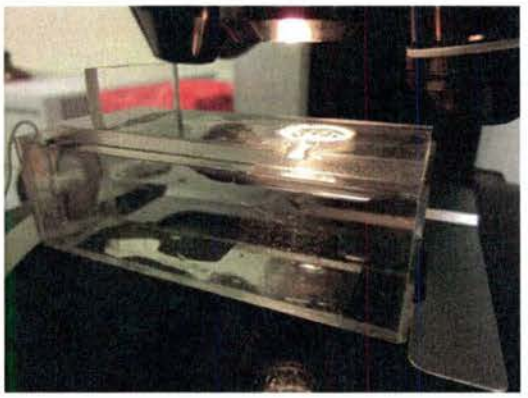

(b)

FIG. 2. A schematic diagram of the microbubble generator chamber (a) and a picture of the chamber under the microscope (b). The electrical wires that connect to the piezotransducer are omitted here. A cover slip that has cells pre-seeded is placed in the top cover, leaving the side with cells facing the chamber water. The bubbles risen from the glass chamber interact with the cells as soon as they reach the cover slip.

III. CHARACTERIZATION

A. Current and voltage characterization

The voltage supplied to the piezotransducer was monitored via two voltage probes (Tek P6139A). The current behavior was monitored through a Pearson current monitor (Model: 2877). Signals were processed through a digital oscilloscope (Tektronix TDS3054C).

Fig. 3 shows a typical voltage waveform measured across the piezotransducer, as well as the current through the circuit. The peak-to-peak voltage is measured to be about 70 V with the magnitude of the negative polarity slightly higher than that of the positive. The peak-to-peak current is roughly 5 A, with the positive current slightly higher than that of the negative. Although the driver circuit is of LC resonance in nature, but the phase difference of current and voltage is not 90° due to extra stray components of the transducer and connection leads. The electrical power deposition onto the transducer was evaluated to be about 17 W. Considering the electromechanical coupling coefficient of 0.59, only about 10 W is channeled into the mechanical vibration of the piezotransducer.

B. Pressure analysis

The acoustic pressure generated in water was monitored in a separate chamber by a fiber optic hydrophone (ONDA HFO-690) in an upright position, where the piezotransducer was arranged vertically in water (at about 6 cm below water surface) and the fiber tip ($\Phi = 150\ \mu$m) was placed directly above its surface at various distances. The signal from the hydrophone controller was processed through the digital oscilloscope.

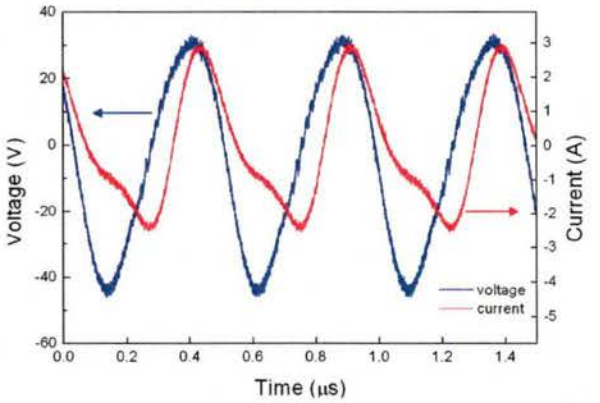

FIG. 3. Current and voltage waveforms of the circuit. The current is not in the same phase as the voltage. The phase relationship is neither as that in a resistive circuit nor a typical resonant circuit.

A pressure waveform measured by the fiber optic hydrophone at a distance of 30 mm from the surface of the spherical piezotransducer is shown in Fig. 4. The positive pressure reaches about 9.5 MPa while the negative pressure is about −4 MPa.

The pressure of the acoustic wave in water at various distances from the piezotransducer was monitored for both the spherical focusing transducer and the flat transducer. The results are shown in Fig. 4(b). The spherical piezotransducer was found to have a focal distance at 30 mm, which agrees with the datasheet provided by the manufacturer. The pressure ranges from ~2 MPa to ~10 MPa between a fiber-to-transducer distance of 20 mm and 40 mm. The pressure produced by the flat piezotransducer is, however, considerably lower: ~1.0 MPa at all distances measured (8-40 mm). Nevertheless, both piezotransducers were able to generate microbubbles in water effectively.

C. Imaging

Images of the bubbles inside the chamber were captured via a digital SLR camera (Nikon D300S) with a macro lens coupled with a 2× teleconverter (Nikon TC-20EIII). The CCD of the camera has a pixel resolution of 181 pixels/mm. With the 2× lens, the camera should in principle be able to capture microbubbles of a diameter of roughly 3 μm (1 pixel). Bubbles grown large enough to rise to the surface of the cover slip due to buoyancy were photographed by a CCD camera (Olympus DP70) through an upright microscope (Olympus BX51) with a 10× magnification. The size of the bubbles in the photos was analyzed using *ImageJ*.[9]

IV. BUBBLE GENERATION

A. Bubbles in water

Microbubbles nucleate in the presence of impurities or pre-existing bubbles in water and oscillate in phase with the

This article is copyrighted as indicated in the article. Reuse of AIP content is subject to the terms at: http://scitationnew.aip.org/termsconditions. Downloaded to IP: 128.82.40.63 On: Mon, 07 Dec 2015 14:59:20

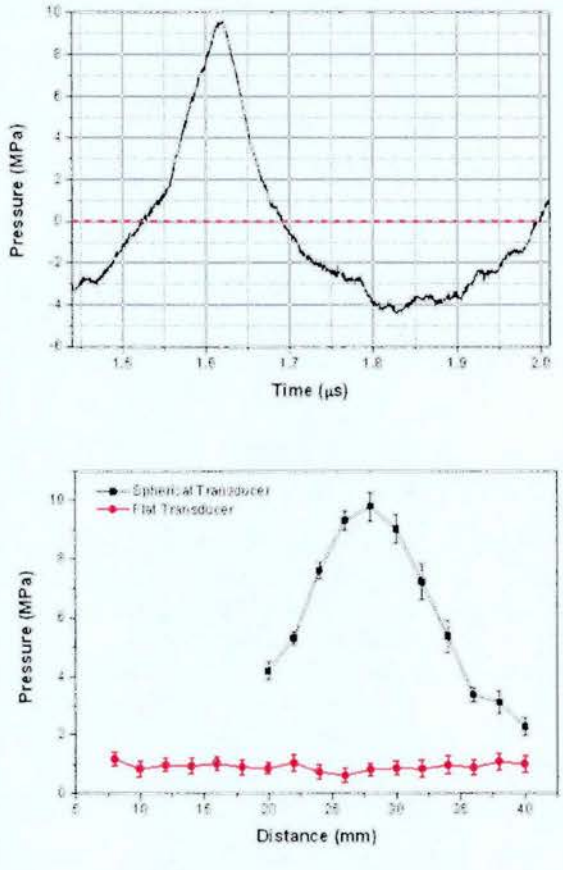

FIG. 4. Pressure waveform measured by fiber optic hydrophone (a) and axial pressure distribution of the spherical and the flat transducer (b).

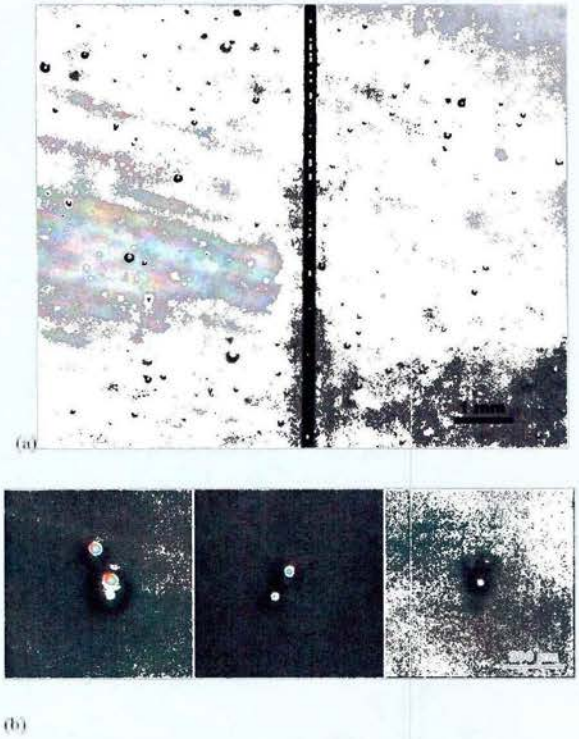

FIG. 5. A still image of the bubbles generated in water. A needle of 190 μm is included as a reference to infer the size of the bubbles (a) and a few examples of bubble clusters (b). The images were taken with an exposure time of 40 ms with a synchronized flash light, at an f-stop of 90. Bubbles tend to form bubble clusters instead of merging into one single bubble.

applied sonic wave. The bubbles expand during rarefactions (negative pressure) and contract during compressions (positive pressure). A typical still image with microbubbles in water is shown in Fig. 5(a). The image was taken at an f-stop of 90 with an exposure time of 40 ms and a synchronized flashlight. A stainless steel needle of thickness 190 μm was included as a reference to infer the size of the bubbles. The radius of the bubbles captured in the images ranges from about 10 μm to about 100 μm. By analyzing a series of images taken at a rate of 24 frames/s, we observed that when the piezotransducer was initially turned on, bubbles generated in water were extremely small (only a few pixels in the images). However, more visible, larger bubbles quickly appear, either due to the direct growth of smaller bubbles or due to the collision and merging of multiple bubbles. Bubbles may also get close to each other and form bubble clusters instead of merging into one single bubble. A few examples of bubble clusters are shown in Fig. 5(b). Interestingly, no bubbles with a radius greater than 100 μm were observed, which may indicate the upper limit of the bubble size in the present system.

B. Bubbles on cover slip

Bubbles that grow large enough rise to the surface of the cover slip and were monitored under the microscope with a 10× objective lens. Before each run, bubbles on the cover slip from the previous cycle were cleaned with *KimWipes*® delicate task wipers. Figure 6(a) is a superimposed image of 17 images taken under the microscope at the same location of the cover slip. The field of view is roughly 1.2×1.2 mm^2. A total of 237 bubbles were analyzed through *ImageJ*. The relay control was set to 2 s on-time and the images were taken after a 3 s delay to allow enough time for the bubbles to rise to the surface of the cover slip. It should be noted that some small bubbles (single digit microns in diameter) do rise to the surface of the cover slip but collapse rather quickly before other bubbles settle on the cover slip. The histogram of the bubble radii is shown in Fig. 6(b). The radii distribute between 5 and 92 μm, with the highest percent frequencies appearing between 10 and 30 μm. Bubbles with larger radii appear less frequently. This result is consistent with the size of the bubbles observed in water and that reported in Ref. 5, where the microbubbles were produced by electrical discharges in water.

Bubbles of similar sizes may collapse at different speeds on the cover slip. We analyzed a series of 896 images of two bubbles captured in a time span of 60 s. Thirty images with the same time spacing were chosen and are illustrated in Fig. 7. The two bubbles are noted as bubble 1 and bubble 2, respectively, for easy reference. The initial radius of bubble 1 (14 μm) is bigger than that of bubble 2 (12.5 μm). This rather small difference in radii, however, leads to a 40% difference in the bubble volumes. The time evolution of the radii and the calculated volumes of the bubbles are plotted in Figs. 8(a) and 8(b). The radius of bubble 2 decays much faster than that of bubble 1. The volumes of bubbles 1 and 2 decay steadily

This article is copyrighted as indicated in the article. Reuse of AIP content is subject to the terms at: http://scitationnew.aip.org/termsconditions. Downloaded to IP: 128.82.40.63 On: Mon, 07 Dec 2015 14:59:20

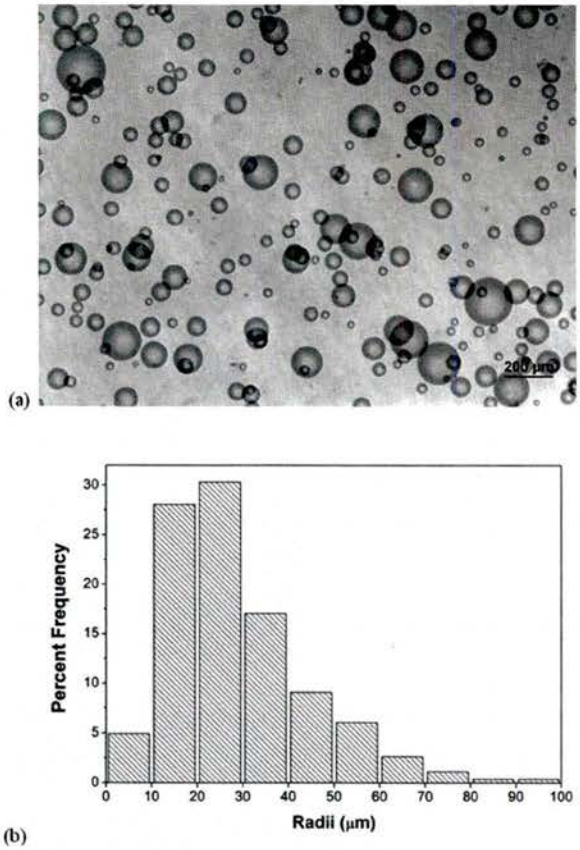

FIG. 6. A superimposed image of 17 images taken at the same location of the cover slip (a) and the histogram of a total of 237 bubbles (b). The bubbles whose radii distribute between 10 and 30 μm appear with the highest percent frequencies.

with time and can be described with a 3rd order polynomial function.

It is interesting to note that the smaller the bubble gets, the faster it collapses on the cover slip. Fig. 9 plots the radial collapsing speed versus the radii of the bubbles. The radial

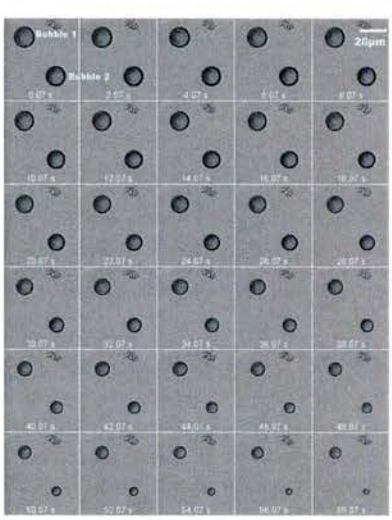

FIG. 7. Photo montage of two similar bubbles collapsing on the cover slip. The initial radius of bubble 1 (14 μm) is bigger than that of bubble 2 (12.5 μm).

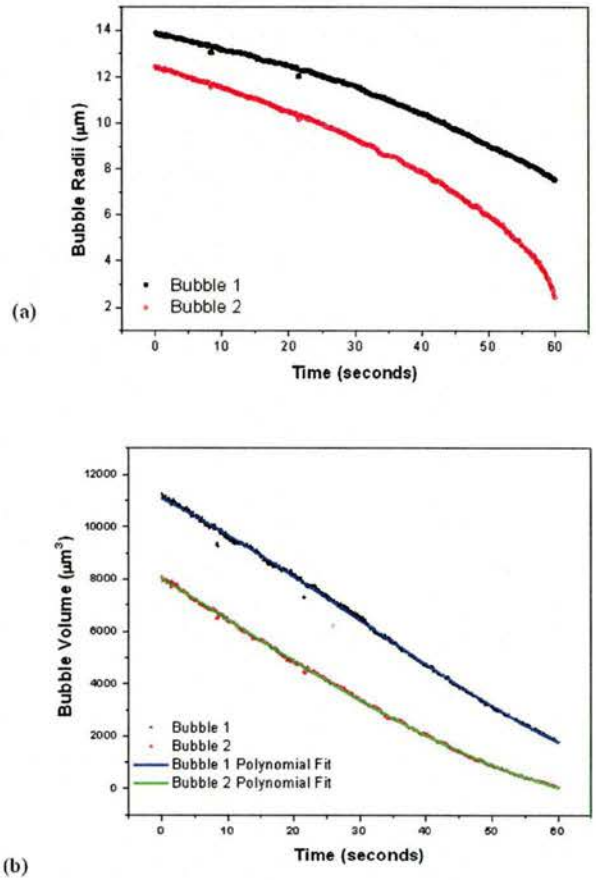

FIG. 8. The time dependence of the cross-sectional area of the bubbles in Fig. 7 (a) and the time dependence of the radius of the cross-sectional circle (b). These results suggest bubbles of similar sizes collapse at different speeds on the cover slip.

collapsing speed of bubble 1 is similar to that of bubble 2 within its detected radius range (8-14 μm), while bubble 2 collapses faster with the decrease of the bubble size.

This phenomenon has been consistently observed on many bubbles captured on the cover slip. We generally summarize our observations as follows: (1) All bubbles collapse on the cover slip given enough time. The smaller the bubble is, the faster it collapses. Bubbles with a radius of >12 μm take more than 60 s to collapse on the cover slip. (2) Bubbles with parting walls tend to coalesce and form bigger bubbles, which in turn collapse at their own pace. (3) Smaller bubbles may exist within larger bubbles given that they arrive at the cover slip first.

Furthermore, not all bubbles have the same wall thickness. Some larger bubbles with thick walls seem to have smaller bubbles embedded in or attached to their walls (shown as voids on the dark walls of bubbles in Fig. 10). These bright spots are not all in perfect circular shape, which mean that they could also be the results of the collapse of smaller bubbles on the wall of bigger bubbles.

V. DISCUSSION

A continuous sinusoidal ultrasonic wave was used in our system. In general, pre-existing gaseous impurities serve as

This article is copyrighted as indicated in the article. Reuse of AIP content is subject to the terms at: http://scitationnew.aip.org/termsconditions. Downloaded to IP: 128.82.40.63 On: Mon, 07 Dec 2015 14:59:20

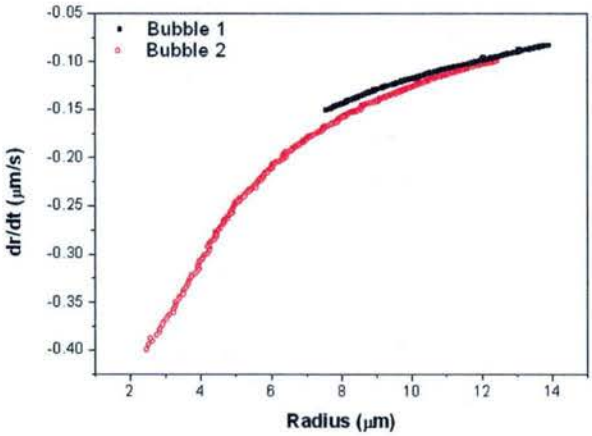

FIG. 9. Radial collapsing speed versus the radius of the cross-sectional circle. As the bubble becomes smaller, the faster it collapses.

the nuclei of bubble formation. During the negative portion of the pressure wave, water is pulled apart at the sites of impurity, forming acoustic microbubbles. During the positive portion of the pressure wave, these bubbles are compressed, albeit not completely. This process repeats in the following acoustic cycles, and the bubbles formed grow until reaching a critical size known as *resonance size*. Beyond this size, the bubbles either become unstable and collapse violently in a few cycles or oscillate near the resonance size for many more cycles. Bubbles may also become fragmented and reduce their sizes, which then serve as nuclei of new cavitation cycles. The relationship of the resonance radius of the bubble with the frequency f is given by Young[10] as

$$R_r = \sqrt{\frac{3\gamma p_\infty}{\rho\omega^2}}, \tag{1}$$

where γ is the specific heat ratio of the gas inside the bubble, which in our case is 1.33 for steam (water).[11] p_∞ is the ambient liquid pressure, which is approximately considered as 1 atm. ρ is the liquid density, which is 999.97 kg/m^3 for water and ω is the angular frequency of ultrasound, which in our case is $2\pi f = 1.32 \times 10^7$ Hz. The resonance radius is then evaluated to be about 1.52 μm. The resulting diameter of the bubbles is ~3 μm, which is beyond the detection range of our CCD camera.

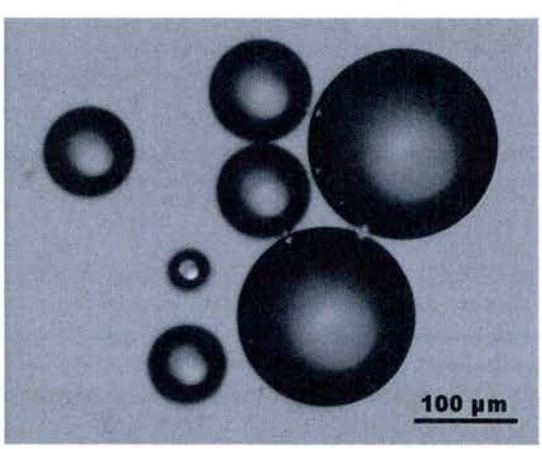

FIG. 10. A photogram of bubbles captured on the cover slip with different bubble wall thicknesses and voids inside the bubbles.

However, two pathways may lead to further growth of these small bubbles beyond the resonance radius R_r, namely, rectified diffusion and bubble coalescence. Rectified diffusion involves an unequal mass transfer across the bubble interface in the rarefaction and compression phases of the ultrasound wave. Eller and Flynn[12] suggested that gas diffusion into/out of a bubble depends on the surface area of the bubble. A bubble has a larger surface area during its expansion than its compression, therefore leading to more gas diffused into than out of the bubble. They also suggested that the wall of bubble thins during its expansion, making it easier for gas to diffuse in. Bubble coalescence involves multiple bubbles coming into contact with each other and forming wall partitions. The parting walls rupture when they become sufficiently thin, leading to the formation of bigger bubbles.[13]

Since our configuration has a glass wall directly facing the ultrasonic wave produced by the piezotransducer on the far end of the chamber, reflected wave interfere with incoming waves, leading to nodes and antinodes of standing waves. Microbubbles formed at the antinodes that grow to a radius $>R_r$ will be pushed toward the nodes by primary Bjerknes forces (acoustic radiation forces on gas bubbles)[14] and become "inactive bubbles" (bubbles that do not implode violently within the liquid near the site of creation). These bubbles eventually become large enough and rise to the surface of the cover slip due to buoyancy once the acoustic wave is interrupted. A more comprehensive discussion of bubbles in an acoustic field can be found in the overview by Ashokkumar and co-workers.[13]

The radius of the bubbles that arrive at the cover slip is distributed between 5 and 92 μm, and >50% of the bubbles have a radius between 10 and 30 μm. These bubbles gradually collapse on the cover slip or merge to form larger bubbles. The smaller the bubble is, the faster the collapse is. We believe these bubbles are of similar properties as those produced by the electrical discharges in water as reported in Refs. 5 and 7. The collapsing time of bubbles with initial radius of ~12 μm is about 60 s. This long collapse time may be favored for biological studies where the observation of time evolution is of essence.

We purposely designed the chamber in such a way that the direction of the mechanical wave is perpendicular to the cover slip, so as to separate the effect of the pressure wave and the collapsing of bubbles on the cover slip during future biological experiments. The all-transparent chamber allows easy access to imaging of the microbubbles in water through the side walls or observation of the event on the cover slip under the microscope. On a cover-slip that has only monolayer cells, the dynamics of microbubble may differ from the tissue which has different surface properties. Thus, the findings of the results may not be directly translatable to tissues, and therefore, our setup may not be applied to tissue. But one can use 3-D artificial matrices to produce physiologically relevant multicellular structures on the cover slip and allow studies to be conducted closer towards actual tissues.

This article is copyrighted as indicated in the article. Reuse of AIP content is subject to the terms at: http://scitationnew.aip.org/termsconditions. Downloaded to IP: 128.82.40.63 On: Mon, 07 Dec 2015 14:59:20

Finally, 2.1 MHz was chosen as the driving frequency of the piezotransducer in our experiments for three reasons: (1) ultrasound frequency at ~20 kHz is known to generate large bubbles for mechanical shearing applications such as emulsification;[15] (2) frequencies between 100 kHz and 1 MHz are used to generate smaller bubbles for sonochemical purposes;[16] and (3) ultrasound with a frequency above 1 MHz has weaker cavitation effects but is commonly used for medical and imaging purposes.[17] By choosing a frequency of 2.1 MHz, we safely stay away from "power ultrasound," yet still produce microbubbles for biological studies.

VI. CONCLUSIONS

An all-transparent chamber was designed to house a vertically arranged piezotransducer, which was driven by a RF voltage at 2.1 MHz directly in water to produce microbubbles for biological studies under a microscope. Bubbles of radius between 5 and 92 μm were observed on the cover slip with the highest percent frequency between 10 and 30 μm. These bubbles collapse with time: The smaller the bubble is, the faster it collapses. Bubbles of around 12 μm in radius take about 60 s to collapse. The fact that these bubbles take longer to collapse may be beneficial to biological studies as the mechanical waves are clearly separated in time from the impact of microbubbles, allowing easy analysis.

ACKNOWLEDGMENTS

This work was supported by a Grant No. N00014-13-1-0404 from the Office of Naval Research.

[1]D. K. Menon, K. Schwab, and D. W. Wright, "Position statement: Definition of traumatic brain injury," Arch. Phys. Med. Rehabil. **91**, 1637–1640 (2010).
[2]A. Nakagawa, G. T. Manley, A. D. Gean, K. Ohtani, R. Armonda, A. Tsukamoto, H. Yamamoto, K. Takayama, and T. Tominaga, "Mechanisms of primary blast induced traumatic brain injury: Insights from shock-wave research," J. Neurotrauma **28**, 1101–1119 (2011).
[3]G. N. Sankin, F. Yuan, and P. Zhong, "Pulsating tandem microbubble for localized and directional single-cell membrane poration," Phys. Rev. Lett. **105**, 078101 (2010).
[4]S. M. Nejad, S. H. R. Hosseini, H. Akiyama, and K. Tachibana, "Optical observation of cell sonoporation with low intensity ultrasound," Biochem. Biophys. Res. Commun. **413**, 218–223 (2011).
[5]S. Sun, J. Kanagaraj, D. Franz, D. Kang, S. Xiao, and M. Cho, "Characterization of subcellular responses induced by exposure of microbubbles to astrocytes," J. Neurotrauma **32**, 1441 (2015).
[6]T. Li, H. Chen, T. Khokhlova, Y.-N. Wang, W. Kreider, X. He, and J. H. Hwang, "Passive cavitation detection during pulsed HIFU exposures of *ex vivo* tissues and *in vivo* mouse pancreatic tumors," Ultrasound Med. Biol. **40**(7), 1523–1534 (2014).
[7]D. Kang, J. B. Nah, M. Cho, and S. Xiao, "Shock wave generation in water for biological studies," IEEE Trans. Plasma Sci. **42**(10), 3231–3238 (2014).
[8]A. R. Selfridge, IEEE Trans. Sonics Ultrason. **32**(3), 381–394 (1985).
[9]W. S. Rasband, ImageJ, U. S. National Institutes of Health, Bethesda, Maryland, USA, 1997–2014, http://imagej.nih.gov/ij/.
[10]F. R. Young, *Cavitation* (McGraw-Hill, London, 1989).
[11]J. G. Speight, *Lange's Handbook of Chemistry*, 16th ed. (McGraw-Hill Education, 2005).
[12]A. Eller and H. G. Flynn, "Rectified diffusion during nonlinear pulsations of cavitation bubbles," J. Acoust. Soc. Am. **37**(3), 493 (1965).
[13]M. Ashokkumar, J. Lee, S. Kentish, and F. Grieser, "Bubbles in an acoustic field: An overview," Ultrason. Sonochem. **14**(4), 470–475 (2007).
[14]T. G. Leighton, A. J. Walton, and M. J. W. Pickworth, Eur. J. Phys. **11**, 47–50 (1990).
[15]T. S. H. Leong, T. J. Wooster, S. E. Kentish, and M. Ashokkumar, "Minimising oil droplet size using ultrasonic emulsification," Ultrason. Sonochem. **16**(6), 721–727 (2009).
[16]K. S. Suslick and L. A. Crum, "Sonochemistry and sonoluminescence," in *Handbook of Acoustics*, edited by M. J. Crocker (Wiley Interscience, New York, 1998), pp. 243–253.
[17]T. S. H. Leong, M. Ashokkumar, and S. Kentish, "The fundamentals of power ultrasound—A review," Acoust. Aust. **39**(2), 54–63 (2011).

This article is copyrighted as indicated in the article. Reuse of AIP content is subject to the terms at: http://scitationnew.aip.org/termsconditions. Downloaded to IP: 128.82.40.63 On: Mon, 07 Dec 2015 14:59:20

Engineering a Light-Attenuating Artificial Iris

Farah Shareef,[1] Shan Sun,[1] Mrignayani Kotecha,[1] Iris Kassem,[2] Dimitri Azar,[1,2] and Michael Cho[1–3]

[1]Department of Bioengineering, University of Illinois at Chicago, Chicago, Illinois, United States
[2]Department of Ophthalmology and Visual Sciences, University of Illinois at Chicago, Chicago, Illinois, United States
[3]Department of Bioengineering, University of Texas at Arlington, Arlington, Texas, United States

Correspondence: Michael Cho, 500 UTA Boulevard, Suite 226, Arlington, TX 76019; michael.cho@uta.edu.

Submitted: May 20, 2015
Accepted: February 24, 2016

Citation: Shareef F, Sun S, Kotecha M, Kassem I, Azar D, Cho M. Engineering a light-attenuating artificial iris. *Invest Ophthalmol Vis Sci.* 2016;57:XXX–XXX. DOI:10.1167/iovs.15-17310

Purpose. Discomfort from light exposure leads to photophobia, glare, and poor vision in patients with congenital or trauma-induced iris damage. Commercial artificial iris lenses are static in nature to provide aesthetics without restoring the natural iris's dynamic response to light. A new photo-responsive artificial iris was therefore developed using a photochromic material with self-adaptive light transmission properties and encased in a transparent biocompatible polymer matrix. ?1

Methods. The implantable artificial iris was designed and engineered using Photopia, a class of photo-responsive materials (termed naphthopyrans) embedded in polyethylene. Photopia was reshaped into annular disks that were spin-coated with polydimethylsiloxane (PDMS) to form our artificial iris lens of controlled thickness. ?2

Results. Activated by UV and blue light in approximately 5 seconds with complete reversal in less than 1 minute, the artificial iris demonstrates graded attenuation of up to 40% of visible and 60% of UV light. There optical characteristics are suitable to reversibly regulate the incident light intensity. In vitro cell culture experiments showed up to 60% cell death within 10 days of exposure to Photopia, but no significant cell death observed when cultured with the artificial iris with protective encapsulation. Nuclear magnetic resonance spectroscopy confirmed these results as there was no apparent leakage of potentially toxic photochromic material from the ophthalmic device.

Conclusions. Our artificial iris lens mimics the functionality of the natural iris by attenuating light intensity entering the eye with its rapid reversible change in opacity and thus potentially providing an improved treatment option for patients with iris damage. ?3 ?4

Keywords: artificial iris, iris functionality, photo-response materials, UV activation, polymer NMR spectroscopy

The human iris provides eye color and facial symmetry while serving a central role in maintaining visual input to the retina. Using the sphincter and dilator muscles, the natural iris quickly and dynamically alters the size of the pupil, allowing for a 30-fold change in light transmission to the retina.[1,2] Excessive light exposure associated with diminished pupil constriction can lead to damage of retinal photoreceptor cells causing a decline in vision over time.[3] Congenital iris defects, such as aniridia or iris coloboma, as well as trauma-induced iris defects, are the two main contributors to reduced functionality of the iris.[4,5] Albinism, in which patients lack the melanin pigment that provides opacity to the natural iris, can also create a larger area through which excessive light can enter the eye.[6] The reduced adaptive response of the iris to light may result in photophobia, glare and haloes, double vision, and decreased visual acuity.[7]

Treatment options to alleviate the adverse effects of iris damage are limited to wearing sunglasses, colored contact lenses, or artificial iris intraocular implants. Although not approved by the Food and Drug Administration (FDA), Morcher GmbH (City, State, Country), Ophtec BV (City, State, Country), and HumanOptics AG (City, State, Country) fixed-diameter artificial iris implants have been used sparingly in the United States under the FDA's compassionate care clause.[8] Morcher's and Ophtec's implants for partial or complete aniridia use a fixed colored disc composed of polymethylmethacrylate (PMMA), a mechanically stiff polymer, which solely blocks peripheral light entering the eye.[9–11] In contrast to the hard polymers used by Morcher and Ophtec, HumanOptics' artificial iris lens is made of a flexible silicone polymer that allows for a smaller incision site.[12] Including an image of a natural iris allows the HumanOptics implant to be used as a cosmetic option to restore or change iris color. However, its fixed pupil size and thus invariable light transmittance fails to dynamically reduce bright light entering the eye.[13,14]

Morcher, Ophtec, and HumanOptics' artificial iris implants have been shown to decrease glare and photophobia as well as increase visual acuity, but postsurgical complications include decentralization due to migration of the implant, inflammation caused by repeated contact with peripheral tissues, and anterior uveitis.[15–17] Additional undesirable effects include secondary glaucoma, myopic shift, and a ghosting phenomenon causing double vision.[18,19] Furthermore, despite their success in reconstructing the shape and color of the natural iris, all three implants have a set pupil diameter and amount of light transmitted, thus lacking the ability to adapt to changes in incident light. One important criterion for improving the

?5 ?6 ?7

This work is licensed under a Creative Commons Attribution-NonCommercial-NoDerivatives 4.0 International License.

//titan/production/i/iovs/live_jobs/iovs-57/iovs-57-03/iovs-57-03-57/layouts/iovs-57-03-57.3d ■ 29 March 2016 ■ 8:06 am ■ Allen Press, Inc. ■ Customer #IOVS-15-17310 Page 1

current treatment options would be to provide the flexibility to attenuate the incident light dynamically.

The development of photo-responsive artificial iris implant should mimic the functionality of the natural iris while restoring iris color and shape. A well-designed artificial iris lens would continuously monitor and reversibly decrease the transmission of light based on the incident light intensity. For example, an increased intensity of ambient light would result in increased activation of the photosensitive component, which should absorb and block transmission of a higher percentage of the bright light, thereby protecting the sensitive photoreceptor cells of the retina. To overcome a major limitation of current iris defect treatment options, rapid activation and reversal times of less than 1 minute would be preferred as well as the synthetic and biocompatible lens materials.

Photochromic or photo-responsive materials are activated by light to undergo a change in molecular conformation. This change switches between a colorless more transparent state and colored opaque state associated with decreased light transmission.[20] Photochromic materials have traditionally been used for nonmedical applications, including memory storage systems, semiconductors, and light-based electric switches. In addition, these materials have been proven safe and effective as external ophthalmic devices such as Transition lenses. Incorporating a photo-responsive material encased within a biocompatible inert polymer without leakage provides an improved means of fulfilling the design criteria. In this study, we present a novel artificial iris that combines photochromic and polymer components to create an ophthalmic device that partially mimics the natural iris and can have long-term implant stability in the eye, which is a major advance over current commercial artificial irises.

Materials and Methods

Manufacturing the Artificial Iris

The artificial iris implant was fabricated using a photo-responsive material encased within a polymer matrix. Pellets of Photopia, which contain the photochromic material (5% wt/vol naphthopyran) in polyethylene (Matsui International, Tokyo, Japan) were melted and reshaped using a hot plate and glass press to create annular disks with the following dimensions: 11-mm outer diameter, 4-mm inner diameter, and 150-μm thickness (Fig. 1A). Encasement within a polymer matrix of biocompatible polydimethylsiloxane (PDMS; Sigma-Aldrich, St. Louis, MO, USA) involved spin-coating and curing a 100-μm layer on each side of the Photopia disk to form the artificial iris (Fig. 1B). Spin-coated thickness was reproducible within 5% error. Polydimethylsiloxane is proven to be biocompatible and has been widely used in tissue engineering. An image of the complete artificial iris construct in its photo-activated and inactive states shows the distribution of Photopia within PDMS (Fig. 2). Selection and use of Photopia, which has a distinctive color change from clear to magenta, induces activation and subsequent light attenuation.

Optical Characterization

The optical functionality of the artificial iris in attenuating incident light was determined with a UV/Vis Spectrophotometer (Beckman Coulter, City, State, Country). The percentage of light transmitted through the artificial iris with and without activation by UV light was measured over a range of wavelengths. Setting the wavelength scan to 300 to 750 nm provided attenuation properties for the two primary regions of interest: the UV (300–400 nm) and visible light spectrum (400–700 nm). To quantify the response of the artificial iris to changes in incident light intensity, neutral optical density filters (optical density = 0, 0.3, and 0.6) were placed between the light source and sample in the spectrophotometer. The wavelength of maximal light attenuation was also determined using these scans. Furthermore, kinetic scans at that wavelength (approximately 360 nm) led to quantification of the activation and reversal times for the artificial iris by measuring the time-dependent percent transmission changes. Image quality after incorporation of the artificial iris into the path of light entering the eye was then assessed. A glass slide etched

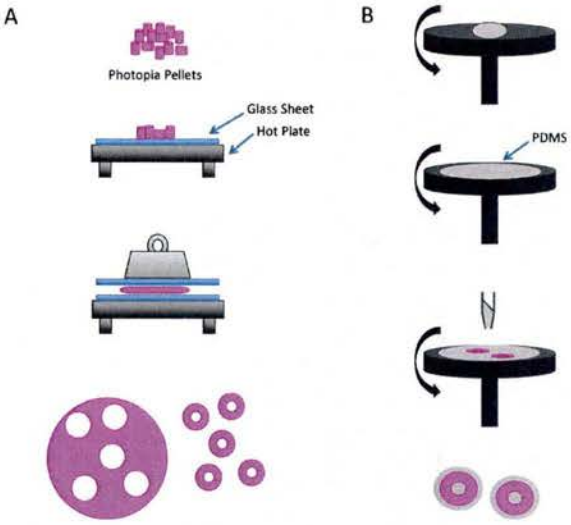

Figure 1. The light-responsive artificial iris was fabricated in two steps: **(A)** photochromic Photopia pellets were heated on a hot plate and reshaped into annular rings using a glass press and cutter, and **(B)** a 100-μm layer of PDMS was spin-coated on each side of the artificial iris to create a disk-shaped construct of 13-mm diameter and 350-μm thickness.

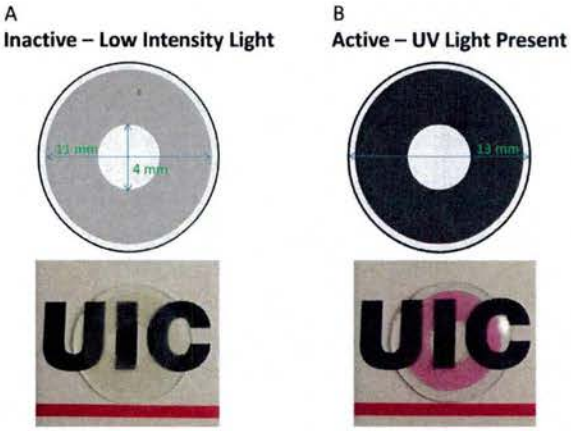

Figure 2. **(A)** Design schematic of artificial iris: the annular dispersion of the photochromic material, Photopia, is shown in *gray*. The *light* and *dark gray* represent the change in color and increased opacity of Photopia on light activation. **(B)** Images of the artificial iris placed on top of the UIC logo show that visual transparency is maintained with and without activation.

with uniformly spaced lines and a ×10 microscope objective were used to represent the object and lens in a classic image formation. Broadening for the thickness of the lines (e.g., blurring) after placement of the artificial iris between the glass slide and objective then served as a measure to quantify the light scattering expected after implantation.

?8

In Vitro Toxicity Testing

Primary human corneal fibroblasts (HCFs), passage 14 to 16, were cultured in Dulbecco's modified Eagle's medium (Sigma-Aldrich) supplemented with 10% fetal bovine serum (Atlanta Biologicals, City, State, Country) and 1% antibiotic-antimycotic solution (Sigma-Aldrich). Human corneal fibroblasts were seeded on 22 × 22-mm coverslips at a cell density of 20,000 cells per coverslip. Indirect cytotoxicity experiments in which HCFs were exposed to media containing the engineered devices were conducted. In these tests, a glass coverslip seeded with HCFs was placed on top of a Photopia disk without encasement or the artificial iris in a Petri dish filled with media. A live-dead cell viability assay (Invitrogen, City, State, Country) was used to stain cells at days 1, 5, and 10. Experiments consisted of two samples each of control, Photopia, and the artificial iris. Three fluorescent images were taken of each sample using a confocal microscope. Cell count was obtained using ImageJ software (http://imagej.nih.gov/ij/; provided in the public domain by the National Institutes of Health, Bethesda, MD, USA).

?9

?10

Structural and Chemical Characterization Using ^{13}C NMR

The ^{13}C nuclear magnetic resonance (NMR) experiments were performed to elucidate the chemical composition and stability of Photopia and the artificial iris in aqueous solution. Specifically, we aimed to identify the reactive, and potentially toxic, side chains of Photopia in solution. Photopia and artificial iris samples immersed in PBS for 3 days were evaluated using ^{13}C NMR along with samples of supernatant PBS exposed for 1 month to Photopia and the artificial iris to determine potential leaching of substances in solution. The NMR measurements were performed using ^{1}H decoupled ^{13}C NMR pulse program (Bruker - zgpg; City, State, Country) at room temperature on an 8.5-T (^{1}H frequency = 360.13 MHz and ^{13}C frequency = 90.55 MHz) Bruker Advance spectrometer equipped with a quadruple nucleus probe capable of multinuclear NMR measurements. A capillary filled with D_2O was placed in the NMR tube to achieve magnetic field homogeneity over the sample volume by locking the deuterium signal. The solid Photopia and artificial iris samples in PBS were placed on top of a doty aurum plug (14 mm) to keep the samples at the center of the radiofrequency coil. The 90° pulse width was 8.75 μs for the monomer solutions and was used as is for polymer samples. The relaxation delay was set to 2 seconds and the number of scans to 1024. The experimental parameters for supernatant samples were the following: 90° pulse width = 13.5 μs, relaxation delay = 2 seconds, and number of scans = 3072. The dimethyl sulfoxide (DMSO) carbon peak at 39.5 ppm was used for chemical shift reference.

?11

Results

Characterization of Artificial Iris

Activation of Photopia and attenuation of incident light were first established through observation of the distinct color change from clear to magenta in response to UV exposure (see Fig. 2B). Subsequent optical testing to quantify the functionality of the artificial iris demonstrated rapid but not instantaneous activation using UV and blue light with maximal activation achieved in less than 30 seconds (images not shown). Similarly, the artificial iris demonstrated gradual reversal that began immediately after removal of the light stimulus with a return to its original state within 1 minute. Wavelength scans of the artificial iris showed maximal attenuation at 390 nm with more than 60% of incident UV light (300–400 nm) and 50% to 65% of visible light (400–700 nm) blocked (Fig. 3A). It was also noted that the artificial iris attenuated a larger percentage of visible light in the green to orange (450–650 nm) range when preactivated by UV light exposure for 30 seconds (Fig. 3A, UV-activated artificial iris). The maximum attenuation (i.e., maximum absorbance) was found to occur at 390 nm. This coincides with the required energy to reversibly break a carbon-oxygen bond in Photopia and thus allowing optical modulation of transmitted light. Characterization of the artificial iris's response to changes in incident light intensity was achieved using neutral density filters of optical density 0, 0.3, and 0.6 to modulate the intensity of incident light by 0%, 50%, and 75%, respectively. It was designed to create varying ambient light intensity environments. The percentage of light blocked by the artificial iris at a given intensity was calculated by taking the difference between the incident light on the artificial iris after traversing the neutral density filter and the percent of that light transmitted through the artificial iris. As the optical density of the filters increases (i.e., the intensity of the light on the artificial iris decreases), the percentage of that incident light blocked by the artificial iris also decreases from 60% to 10% (Fig. 3B). In other words, as the incident light becomes dimmer, the artificial iris transmits more light, thereby attenuating high-intensity light while ensuring enough light enters the eye in the low light intensity environment.

Experiments to assess postimplant image quality were conducted using a glass slide etched with uniformly spaced lines 100 μm apart and a ×10 microscope objective to represent an object-lens-image visual system. The control image of the glass slide was acquired using differential interference contrast microscopy (Fig. 4A). Placement of the annular photochromic region of the artificial iris between the glass slide and the objective resulted in a darkened image (overall pixel intensity was reduced as seen by a gray background compared with the control image) with blurred lines (Fig. 4B). The degradation of image quality is perhaps best characterized by estimating the full width half maximum (FWHM) values. For example, the FWHM was calculated 5 μm in the control experiment without introducing the artificial iris in the optical pathway. This value can be used to represent the resolution and appears to be independent of the wavelength range in this study. Insertion of the artificial iris increased the FWHM by approximately 10-fold to 50 μm. An adjustment of the focal length by approximately 150 μm seemed to reverse the blurring effect (FWHM = 8 μm), resulting in an image of sharply refocused lines with decreased overall pixel intensity (Fig. 4C). The change in resolution of the lines in the three images and the corresponding pixel intensity modulation along a horizontal line are shown in Figure 4D.

In Vitro Response

Human corneal fibroblasts with indirect contact to the artificial iris or Photopia over a 10-day period were stained with green calcein AM (fluorescence green) to identify live cells and ethidium homodimer to highlight the dead cells (red fluoresces red). The resulting images indicate that the viability and proliferation of cells exposed to the artificial iris were

//titan/production/i/iovs/live_jobs/iovs-57/iovs-57-03/iovs-57-03-57/layouts/iovs-57-03-57.3d ■ 29 March 2016 ■ 8:07 am ■ Allen Press, Inc. ■ Customer #IOVS-15-17310

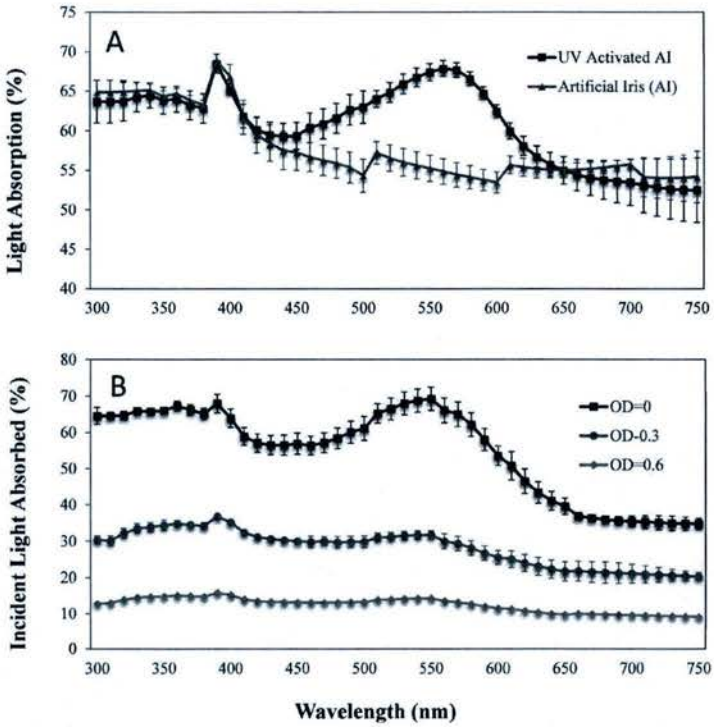

Figure 3. **(A)** Light transmittance of the artificial iris in the ultraviolet (300–400 nm) and visible (400–700 nm) spectrum. Preactivation by exposure to 365-nm light for 30 seconds (UV activated) results in reduced transmission in the green to orange (450–650 nm) range, thus highlighting the additional light blocked by the artificial iris when outdoors or in the presence of UV light. **(B)** The percentage of incident light absorbed by the artificial iris increases from 12% to 60% as the intensity of the incident light on the construct is increased. Thus, the artificial iris has higher light attenuation in bright light than it does in dim light settings.

comparable to those of the control sample (Fig. 5A). However, cells exposed to Photopia alone versus the control sample showed decreased live cells after 5 and 10 days. Quantification of live HCFs from these fluorescent images confirmed no significant difference in the number of live cells between the artificial iris and control samples at day 1 through 10 (Fig. 5B). In contrast, on days 5 and 10, the average live cell count was 40% less for HCFs exposed to Photopia compared with the control.

Structural and Chemical Characterization Using ^{13}C NMR

Following our in vitro experiments, NMR spectroscopy was used to determine Photopia's chemical structure and potentially reactive side groups and to validate the stability of the artificial iris in solution. The ^{13}C NMR spectra of Photopia and the artificial iris immersed in PBS for 3 days (Fig. 6A) identified the mobile molecular groups in the samples. The assignments are given in the Table. The common peaks seen in these scans belong to Photopia. It was noted that on coating with PDMS, an additional strong peak related to CH_3 of PDMS appears in the artificial iris spectra and the peaks related to Photopia are shifted upfield. A second set of NMR experiments (Fig. 6B) was conducted on PBS exposed to either the artificial iris or Photopia over 1 month to ascertain which molecules if any leached out of the samples over time. For these samples, NMR of the supernatant liquid alone was tested. In the case of no leaching, NMR peaks should not be seen, as there are no carbon-based substances in PBS. However, both the artificial iris and Photopia had CH-O residual monomer peaks, perhaps coming from the main polymer anchor (e.g., CH2 of polyethylene). However, the Photopia sample alone showed an additional peak at 124 ppm possibly coming from the aromatic carbon group in the naphthopyran (Fig. 6C), which might be responsible for the cell death in Photopia (see Fig. 5A). This potential leaching is effectively blocked in the artificial iris, likely due to PDMS coating and therefore improving the overall cell survival.

Discussion

The light-responsive artificial iris was designed as a biocompatible ophthalmic implant with self-adjusting light transmission properties to partially mimic the functionality of the natural iris. Dynamic light attenuation was achieved through incorporation of a photo-responsive material (Photopia, 5% naphthopyran) that undergoes a reversible molecular conformational change induced by UV or blue light.[21] Photochemical cleavage of the carbon-oxygen bond within the pyran ring by incident light converts a naphthopyran to its colored opaque ring-open state, while reversal to its original transparent ring-closed form occurs spontaneously with removal of the UV light stimulus.[22] This class of photochromic materials is particularly suited for ophthalmologic applications due to its efficient photo-response, large light absorbance when activated, rapid reversal, and fatigue resistance.[23]

Encasing an annular disk of Photopia within PDMS (Figs. 1, 2) to form the artificial iris implant met our design objectives by restoring iris shape and providing significant light attenu-

//titan/production/i/iovs/live_jobs/iovs-57/iovs-57-03/iovs-57-03-57/layouts/iovs-57-03-57.3d ■ 29 March 2016 ■ 8:07 am ■ Allen Press, Inc. ■ Customer #IOVS-15-17310

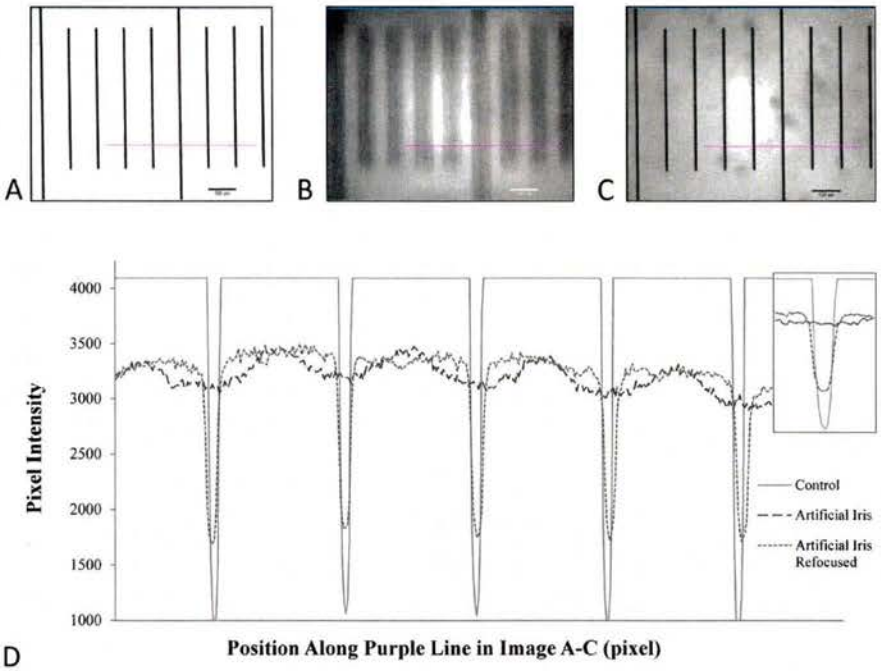

Figure 4. **(A)** Control. Image of glass slide with *black lines*. **(B)** Artificial iris. Image through peripheral photochromic region of artificial iris (AI): light scattering (increased thickness of *blurred black lines*) and decreased overall light transmission (*gray background*). **(C)** Artificial iris refocused. Image through peripheral artificial iris after focal length increased by approximately 150 μm: visual acuity restored. **(D)** Pixel intensity versus position along *purple lines* in **(A)** to **(C)**. Image resolution denoted by the full width half maximum of control **(A)** and artificial iris refocused **(C)** is greater than image formed through artificial iris alone **(B)**. Reduced light transmission (decreased baseline intensity) for images through AI **(B** and **C)** compared with control **(A)** was also noted.

ation while maintaining visual acuity through the clear center where light passes unimpeded for sight. Through selection of a photo-responsive material with activation and reversal times in less than 1 minute, we have overcome the primary limitation of other iris defect treatment options such as Transition lenses, which have prolonged reversal times in excess of 10 minutes when indoors. Similarly, the use of this particular self-adaptive light-sensitive material resulted in a less bulky alternative to the circuits found in electric artificial irises[24] and improved on current commercial artificial irises, such as HumanOptics AG through its light-attenuating profile.[25] Encasing Photopia in hydrophobic PDMS was central to preventing cell migration and surface attachment, which could affect light transmission through our artificial iris.

The human eye relies on the pupillary light reflex, the constriction and recovery of the iris in response to light stimulus, to modulate the light flux into the eye.[26] Along with controlling retinal illumination, a light-responsive pupil can change the depth of focus and, with a smaller pupil size, reduce optical aberrations, light diffraction, and visual effects such as glare.[27,28] Our goal in engineering a new artificial iris was to restore these natural iris properties to patients with congenital or trauma-induced iris defects. By blocking up to 60% of incident light across the UV and visible light spectra,

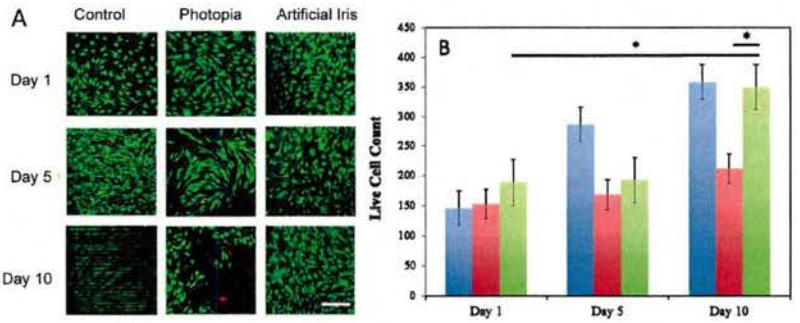

Figure 5. Human corneal fibroblasts were cultured with either the annular Photopia disks or the complete artificial iris for up to 10 days. **(A)** Cell viability staining (live cells = *green*, dead cells = *red*) show similar morphology and proliferation rate between control and artificial iris-exposed HCFs, whereas cell death and detachment (*black areas* represent cell-free regions) was noted for HCFs cultured with Photopia. For all images, *scale bar* = 200 μm as seen in *bottom right image*. **(B)** Quantification of live cells elucidated that Photopia counteracts cell proliferation as live cell count did not significantly change from day 1 to 10. Control, *blue*; Photopia, *red*; artificial iris, *green bars*.

//titan/production/i/iovs/live_jobs/iovs-57/iovs-57-03/iovs-57-03-57/layouts/iovs-57-03-57.3c ■ 29 March 2016 ■ 8:07 am ■ Allen Press, Inc. ■ Customer #IOVS-15-17310

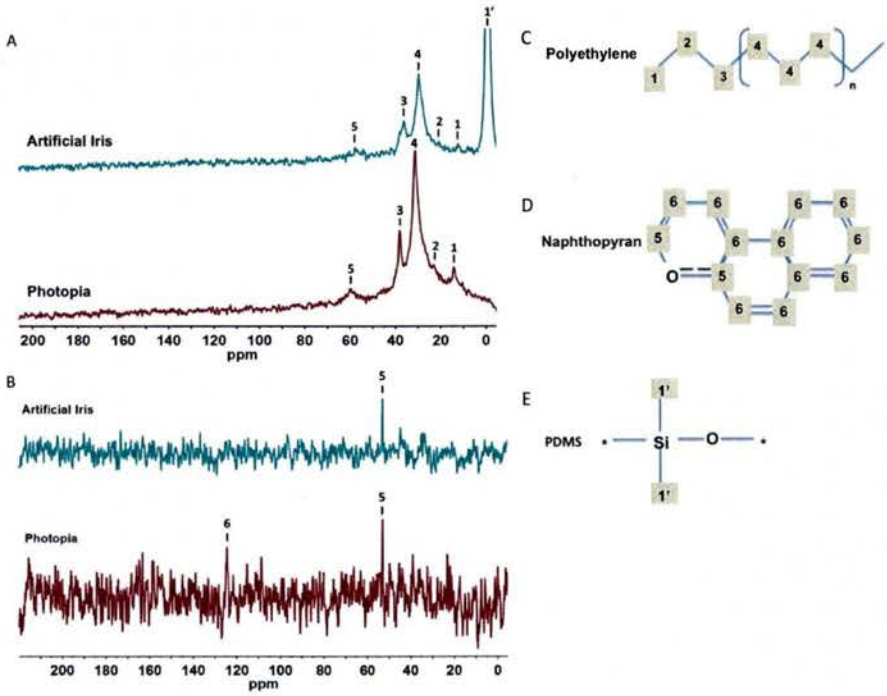

Figure 6. **(A)** ^{13}C NMR spectra of Photopia and artificial iris samples immersed in PBS. The visible peaks are from mobile fractions of polymers in aqueous solution. **(B)** ^{13}C NMR spectra of supernatant PBS exposed to Photopia and artificial iris for 1 month. The 124-ppm peak seen in Photopia supernatant is effectively blocked and not visible in the artificial iris supernatant sample. **(C)** Chemical structure of polyethylene, naphthopyran, and PDMS. The reversible and photoactive C-O bond in naphthopyran is indicated by a *dashed line*.

our artificial iris approaches such a design goal (Fig. 3A, artificial iris). Furthermore, when activated by UV light, the artificial iris blocks an additional 10% of green to orange light (450–650 nm), thereby enhancing its light sensitivity when outdoors or in the presence of harmful UV radiation (Fig. 3A, UV-activated artificial iris).

As the naphthopyran side groups largely determine its light-transmission properties, Photopia's unique chemical structure allows for the increased attenuation of visible light in the active state.[22] In addition to diminishing the amount of light entering the eye based on wavelength, our artificial iris has graded light transmission depending on the intensity of the incident light. Applying neutral-density filters with optical density of 0, 0.3, and 0.6 to alter intensity across the light spectrum showed that as the ambient light brightens, a larger percentage of that light is absorbed (Fig. 3B). Thus, similar to the natural iris, our implantable artificial iris has the sensitivity to inhibit high-intensity light while allowing enough light to enter the eye in dim settings to maintain vision.

Although the artificial iris retains visual acuity through its clear pupillary region, it was hypothesized that the image through the photochromic region may have decreased clarity due to the molecular structure of Photopia. The classic optics model of an object-(artificial iris)-lens-image system was used to characterize the change in visual acuity through the peripheral artificial iris. We found an approximately 25% decrease in the baseline intensity (Fig. 4), which corroborates the results of previous optical testing and confirmed the artificial iris's ability to attenuate incident bright light. We also noted a quantifiable degree of light scattering (Fig. 4D) as indicated by the increased FWHM estimates. However, further testing indicated that adjusting the focal length by 150 μm at which the image through the peripheral artificial iris was taken could counter and minimize this light scattering (Fig. 4C) while providing the expected light attenuation. The graph of pixel intensity verses position along a preselected line (Figs. 4A–C) more clearly demonstrates that changing the focal length can restore image resolution (Fig. 4D). For this graph, the image resolution is depicted by the change in pixel intensity between the white background and the black lines as seen in the control image. In comparison, the artificial iris curve has decreased baseline pixel intensity and a more gradual change in the slope representing the light diffraction of the lines imaged through the peripheral artificial iris. However, the similarity in steepness of the pixel intensity curves for the control and

Table. ^{13}C NMR Chemical Shift and Assignments

	Peak Number	Chemical Shift, ppm	Assignments
Artificial iris	1′	1.02	CH_3 (PDMS)
	1	12.13	CH_3 (PE)
	2	20.9	CH_2 (PE)
	3	29.5	CH_2 (PE)
	4	36	CH_2 (PE)
	5	57.3	CH-O (NTHP)
Photopia	1	14.29	CH_3 (PE)
	2	23.10	CH_2 (PE)
	3	31.28	CH_2 (PE)
	4	37.86	
	5	60.32	CH-O (NTHP)
Artificial iris	1	53.04	CH-O (NTHP)
Photopia	1′	53.04	CH-O (NTHP)
	2′	124	C (NTHP)

//titan/production/i/iovs/live_jobs/iovs-57/iovs-57-03/iovs-57-03-57/layouts/iovs-57-03-57.3d ■ 29 March 2016 ■ 8:09 am ■ Allen Press, Inc. ■ Customer #IOVS-15-17310

artificial iris refocused images signifies that the image degradation can be reversed and corrected with a change in focal length.

Collectively, the visual acuity data indicated that images taken through the periphery of the artificial iris would have reduced pixel intensity but diminished resolution compared with images through the clear PDMS center, unless the focal length was adjusted. Fortunately, simulating a change in focal length (i.e., optical power) to maintain focus on objects as their distance varies is an inherent process of the human lens, termed accommodation.[29] Given that the optical power of the human lens is measured in diopters, calculated as the inverse of focal length, the 150-μm change in focal length required for visual clarity is equal to a change in optical power by 0.55 diopters. As the optical power of the human lens can vary up to 10 diopters or more until age 40, it appears the natural lens could accommodate the light diffraction through the peripheral artificial iris postimplant. Thus, individuals with our artificial iris could maintain visual acuity when light passes through both the clear center and the light-responsive peripheral region of the implant.[30]

Once it was determined that our artificial iris met the optical design criteria, we pursued cell culture experiments to ascertain the biocompatibility of the artificial iris in vitro. Human corneal fibroblasts were indirectly exposed to samples of the artificial iris and Photopia alone for up to 10 days. Cell viability was established when normal morphology and proliferation rates were observed for HCFs exposed to the artificial iris compared with control samples (Fig. 5A). The biocompatibility of the artificial iris was then validated when subsequent analysis indicated no significant change in live cell count (Fig. 5B) for artificial iris and control samples at all study time points. In contrast, the decreased number of HCFs in the Photopia samples highlighted the potential adverse effects of exposure to Photopia alone. As the artificial iris consists of Photopia encased in PDMS, a polymer whose biocompatibility has been well established,[31,32] the in vitro data suggested that the design of the artificial iris inhibited cell death despite the possible toxicity of Photopia. We postulate that interaction of ionic media with reactive surface naphthopyran molecules in Photopia might have caused the cell death observed with the Photopia samples.

Based on the in vitro data, we endeavored to determine the molecular structure of Photopia and any potentially reactive side chains that could cause toxicity in solution. In addition, we aimed to ascertain the stability of the artificial iris implant over time. Commonly used to determine the structure and morphology of inorganic materials, NMR spectroscopy detects the chemical environment of atomic nuclei based on the differences in electromagnetic radiation they emit in the presence of a high magnetic field.[33] The mobile molecular groups in both samples were identified using ^{13}C NMR scans of Photopia and the artificial iris in PBS and are shown in the Table. Common peaks between the scans (Fig. 6A) were used to identify the molecular components of Photopia. The upfield shift of the Photopia-related peaks in the artificial iris spectra and the presence of the strong CH_3 peak associated with the PDMS coating indicated that PDMS served as an effective barrier in preventing the interaction of Photopia with the ions in aqueous solution. Another set of NMR experiments (Fig. 6B) on PBS exposed to the artificial iris or Photopia for 1 month was conducted to ascertain if molecular leaching would occur over time. Nuclear magnetic resonance testing of the supernatant liquid alone showed a peak at 124 ppm in the Photopia sample not seen in the artificial iris scan that could have arisen from the aromatic carbon group in the naphthopyran (Fig. 6C). This additional molecular species in solution may explain the cell death seen in images of Photopia at day 10 (see Fig. 5A). Furthermore, it confirms that the PDMS coating in the artificial iris effectively prevents leaching of aromatic carbon group while ensuring in vitro cell survival and stability of the implant over time.

Conclusions

Our light-activated artificial iris is a biocompatible implant that partially mimics the functionality of the natural iris while restoring iris aesthetics. Incorporation of a photo-responsive material encased in a PDMS matrix to engineer our device provides for a new artificial iris design. The dynamic light attenuation based on the ambient light intensity and wavelength (UV or visible light) characteristic of our artificial iris improves on the properties of commercial artificial iris implants. The ability to attenuate up to 60% of incident light provides our artificial iris with the means to alleviate or at least significantly reduce the symptoms of iris damage, such as photophobia, glare, and haloes. By maintaining visual acuity for light traversing both the central transparent PDMS as well as the light-responsive peripheral region, our implant proves comparable to commonly used intraocular lens implants. Unlike photochromic intraocular lenses that filter out UV and blue lights by absorbing them,[34,35] the artificial iris we developed filters and uses UV lights to activate the photoresponse materials to dynamically modulate the incident light intensity. In addition to providing enhanced optical properties, it demonstrated biocompatibility in vitro despite potential toxicity from Photopia alone. Follow-up testing using ^{13}C NMR served to identify structural characteristics of Photopia including ones that may lead to toxicity in solution as well as established that the PDMS coating in the artificial iris prevents leaching. Future work on artificial iris implantation in the rabbit eye would be necessary to confirm these findings in vivo. Although the final design of the artificial iris will be optimized based on preclinical animal model studies, we have successfully engineered a photo-responsive and biocompatible artificial iris implant with dynamic light-attenuation properties that may provide a new treatment option for patients with congenital or trauma-induced iris defects.

Acknowledgments

We thank Carlos Ng for his expertise and effort with artificial iris microfabrication.

Supported by the FMC Technologies, Inc., Fellowship (FS), Office of Naval Research Grant N00014-13-1-0404 (MC), National Institutes of Health Grant NEI K08 EY024645 (IK), and National Eye Institute Core Grant P30 EY001792 (IK).

Disclosure: **F. Shareef**, None; **S. Sun**, None; **M. Kotecha**, None; **I. Kassem**, **D. Azar**, None; **M. Cho**, None

References

1. Watson AB, Yellott JI. A unified formula for light-adapted pupil size. *J Vis*. 2012;12(10):1–16.
2. Campbell. *Biology*. 2nd ed. CA: Benjamin-Cummings Publishing Company; 1990. ?12
3. Glickman RD. Phototoxicity of the retina: mechanisms of damage. *Int J Toxicol*. 2002;21:473–490.
4. van Heyningen V, Hanson I, Hingorani M. Aniridia. *Eur J Hum Genet*. 2012;20:1011–1017.
5. Brooks BP, Meck JM, Haddad BR, Bendavid C, Blain D, Toretsky JA. Uveal coloboma: clinical and basic science update. *Curr Opin Ophthalmol*. 2006;17:447–470.
6. Brondum-Nielsen K, Grønskov K, Ek J. Oculocutaneous albinism. *Orphanet J Rare Dis*. 2007;2:43–50.

7. Liu C, Mavrikakis I, Mavrikakis E, et al. Surgical management of iris defects with prosthetic iris devices. *Nature Eye*. 2005;19: 205–209. ?13
8. Stephenson M. More appealing options for artificial iris patients. *Review of Ophthalmology*. 2010. ?14
9. Morcher Implants. Available at: http://www.morcher.com/en.html. ?15
10. Chung M, Miller KM, Weissman BA. Morcher iris reconstruction lens and rigid contact lens for traumatic aniridia. *Eye Contact Lens*. 2009;35:108–110.
11. Ophtec Iris Reconstruction System. Available at: http://www.ophtec.com/.
12. Doran M. Iris implant advance–but face continuing challenges. *EyeNet Magazine*. 2013. ?16
13. Human Optics Artificial Iris. Available at: http://www.artificial-iris.com/index-en.html. ?17
14. Krader CG. Posterior chamber implant reduces visual problems. *Ophthalmology Times*. 2011;. ?18
15. Osher RH, Karatza EC, Burk SE, Snyder ME. Outcomes of prosthetic iris implantation in patients with albinism. *J Cataract Refract Surg*. 2007;33:1763–1769.
16. Olson M, Masket S, Miller KM. Interim results of a compassionate-use clinical trial of Morcher iris diaphragm implantation: report 1. *J Cataract Refract Surg*. 2008;34: 1674–1680.
17. Liu C, Lee RM, Dubois VD, et al. Opaque intraocular lens implantation: a case series and lessons learnt. *Clin Ophthalmol*. 2012;6:545–549.
18. Manero F, Güell JL, Morral M, Gris O, Elies D. Transient myopic shift after phakic intraocular lens implantation. *J Cataract Refract Surg*. 2012;38:1283–1287.
19. Patel CK, Yusuf IH, Arun KS, Rosen P. Black-on-black secondary occlusive IOL implantation to alleviate enigmatic light perception through a black IOL. *J Cataract Refract Surg*. 2013;39:1439–1441.
20. Lehn J-M. *Photochromism: Molecules and Systems*. Elsevier Publishing; 2003. ?19
21. Crano JC, Guglielmetti RJ. *Organic Photochromic and Thermochromic Compounds: Volume 1: Main Photochromic Families*. New York: Kluwer Academic Publishers; 2002.
22. Song L, Yang Y, Zhang Q, Tian H, Zhu W. Synthesis and photochromism of naphthopyrans bearing naphthalimide chromophore: predominant thermal reversibility in color-fading and fluorescence switch. *J Phys Chem B*. 2011;115: 14648–14658.
23. Zhen W, Meng Q, Zhang Z, Fu D, Zhang W. Synthesis and photochromic properties of substituted naphthopyran compounds. *Tetrahedron*. 2011;67:2246–2250.
24. Lapointe J, Durette JF, Harhira A, Shaat A, Boulos PR, Kashyap R. A 'living' prosthetic iris. *Eye*. 2010;24:1716–1723.
25. Miller KM, Rosenthal KJ, Snyder ME, Tam DY, Oetting T. Cataract and lost iris tissue after trauma. *Cataract & Refractive Surgery Today*. January 2012;. ?20
26. Winn B, Whitaker D, Elliott DB, Phillips NJ. Factors affecting light-adapted pupil size in normal human subjects. *J Invest Ophthalmol Vis Sci*. 1994;35:1132–1137.
27. Markwell E, Feigl B, Zele AJ. Intrinsically photosensitive melanopsin retinal ganglion cell contributions to the pupillary light reflex and circadian rhythm. *Clin Exp Optom*. 2010;93: 137–149.
28. Mathôt S, van der Linden L, Grainger J, Vitu F. The pupillary light response reveals the focus of covert visual attenuation. *PLoS One*. 2013;8:e78168.
29. Chien C-H, Huang T, Schachar RA. Analysis of human crystalline lens accommodation. *J Biomech*. 2006;39:672–680.
30. Abolmaali A, Schachar RA, Le T. Sensitivity study of human crystalline lens accommodation. *Comput Methods Programs Biomed*. 2007;85:77–90.
31. Bélanger M-C, Marois Y. Hemocompatibility, biocompatibility, inflammatory and in vivo studies of primary reference materials low-density polyethylene and polydimethylsiloxane: a review. *J Biomed Mater Res*. 2001;58:467–477.
32. Worthington KS, Wiley LA, Bartlett AM, et al. Mechanical properties of murine and porcine ocular tissues in compression. *Exp Eye Res*. 2014;121:194–199.
33. Kimura H. Molecular dynamics and orientation of stretched rubber by solid-state 13C NMR. *Polymer Journal*. 2010;42:25–30.
34. Ao M, Chen X, Huang C, et al. Color discrimination by patients with different types of light-filtering intraocular lenses. *J Cataract Refract Surg*. 2010;36:389–395.
35. Zhu X-F, Zou HD, Yu YF, Sun Q, Zhao NQ. Comparison of blue light-filtering IOLs and UV light-filtering IOLs for cataract surgery: a meta-analysis. *PLoS One*. 2012. ?21

//titan/production/i/iovs/live_jobs/iovs-57/iovs-57-03/iovs-57-03-57/layouts/iovs-57-03-57.3d ■ 29 March 2016 ■ 8:09 am ■ Allen Press, Inc. ■ Customer #IOVS-15-17310